Doctoral Thesis

Effect of elevated temperature on water uptake behavior in cement-based materials

by

Ragathara GurrappaGari Rohith Kiran

supervised by

Prof. Ippei Maruyama

Nagoya University

Graduate school of Environmental Studies

Effect of elevated temperature on water uptake behavior in cement-based materials
(セメント系材料の吸水挙動に及ぼす昇温の影響)

Ragathara GurrappaGari Rohith Kiran

Ph.D. (Engineering)

Graduate school of Environmental Studies, Nagoya University

Abstract

In this thesis, non-destructive techniques of (^{1}H-NMR relaxometry and X-ray computed radiography) were used to understand the behavior of water.

During sorption, the microstructural evolutions of two different cement pastes (with water-to-cement ratios of 0.40 and 0.55) are studied via proton-nuclear-magnetic-resonance relaxometry. The water uptake test is performed for samples dried at 105 °C under three different temperatures of 20 °C, 40 °C, and 60 °C for the first twenty-six days of sorption. It is observed that the water went first to the larger pores before migrating to the finest ones. This behavior is accelerated with increasing temperature. The rate of water exchange between fine and large pores is estimated and found to increase with temperature for both studied mixtures. The activation energy corresponding to this water movement is calculated and found to be higher for the lowest water-to-cement ratio, owing its finer microstructure. Finally, the activation energy related to the local water transport in re-distribution from large pores to fine pores is calculated and found to be inferior to the experimental results, which can be explained by the dynamic microstructure not being considered in the classical theories.

X-ray computed radiography (X-ray CR) is used, which is a non-destructive technique for visualizing water movement and quantifies the depth of penetration and cumulative water absorbed in mortar specimen. This experimental and numerical study aims to evaluate the penetration depth of contaminated water in concrete structures involved in the Fukushima Daiichi power plant. The influence of mortar mixture on water absorption was investigated by varying the composition: mortar containing aggregates from river sand and crushed limestone sand was compared, and 15% of the cement in the mixture was substituted with fly ash. The effect of temperature in nuclear conditions is also significant; therefore, water uptake at temperatures of 20 °C and 60 °C was considered. Finally, pre-drying conditions were studied by drying the sample at two different conditions: at 105 °C and at 40% RH (relative humidity) and 20 °C. Water uptake was monitored using x-ray computed radiography in combination with mass measurements. In all cases, anomalous sorption, or a nonlinear relationship between penetration depth and the square root of exposure time was observed, with the sorption curves showing bimodal behavior. The aggregate type had no significant effect on the water uptake results. However, the samples containing fly ash clearly had lower water uptake rates, which can be explained by the differences in the calcium silicate hydrate (C-S-H) structures. With increasing

temperature, the penetration was slightly accelerated at the beginning of the experiment, with the rate of penetration then decreasing rapidly. The densification of C-S-H at higher temperatures could contribute to this phenomenon. Microstructural rearrangements can also explain why the highest uptake rates occurred for samples that were exposed to severe drying conditions (105°C). The experimental results were consistent when the microstructural rearrangement was considered, further confirming these conclusions.

Keywords: (a) Calcium silicate hydrate, (b) Temperature, (c) Water uptake, (d) ^{1}H-NMR relaxometry, (e) X-ray computed radiography

Thesis Advisor: Prof. Ippei Maruyama

Acknowledgment

Firstly, I thank almighty God who is the source of strength and motivation for all the tasks I take up and the ultimate reason for the successful completion of this work. I am grateful for the chance to convey my heartfelt appreciation and obligation of gratitude to all of the staff. I'd want to convey my sincere gratitude to Professor Ippei Maruyama at Nagoya University for his precious time, unwavering support, and tremendous advice. His suggestions and criticisms were very helpful in improving the research's fundamentals and technical aspects.

Dr. Samouh Hamza deserves special thanks for his contributions and technical advice. I'm also grateful for his time, support, and assistance in completing duties. He has been very helpful with my doctorate course recommendations, which I gratefully appreciate.

Special thanks to Professor Sanjay Pareek, who was always encouraging and encouraged us to go the additional mile. I appreciate his advice, encouragement, and suggestions, without which I would not have been able to cross the finish line.

Professor Araki Yoshikazu (GSES, Nagoya university), and Professor Yo Hibino (GSES, Nagoya University), are my reviewers, and I am grateful for their time, insightful comments, and suggestions that helped me improve my work.

I am also grateful to Nagoya University and its employees for making my time in Japan as simple as possible and providing all of the research facilities I needed.

My colleague researchers and other members of our laboratory have been very helpful. Special thanks to my wonderful friends Dr. Sasano Hiroshi, Dr. Jiří Rymeš, Dr. Ryo Kurihara, Dr. Suwanmaneechot Piyapong, Dr. Pranjal Satya, Dr. Abudushalamu Aili, and Dr. Samouh Hamza, Akira Matsuda, Tatsuto Haji, Fujimaki Tetsuya, Tsunekawa Koki, Umeki Shota, Kanbayashi Daisuke, and Goto sou for being so supportive, inspirational, and amusing. I owe my gratitude to the other students in our lab who were constantly encouraging and inspiring. I'm also grateful to our laboratory's secretaries, Keiko Nakamura and Chiaki Miura, for their support and assistance, since they were always accessible whenever I needed it.

It is always beneficial to have companions for entertainment and inspiration, since this keeps me from feeling depressed. I owe a particular thanks to Kumar Avadh, Nikhil, Saad, Shobhit, pranjal satya, Ajinkya, Rahul Deshmukh, Sunil, Arjit Bose, Nishtha Tiwari, Gaurav, Dr. Debaleen Biswas, Sachin and Priyanka for their support and friendship throughout the years.

Finally, but certainly not least, I owe my gratitude to my parents for their unwavering and tremendous support, which they extended to me in every manner possible.

They have my gratitude for carrying me and for their faith in me. My sisters and my brothers motivation has surpassed my expectations.

Contents

*In this thesis, many passages and figures are represented from the followimg papers published by the author in Journal of Advanced Concrete Technology

- Kiran, Rohith, Hamza Samouh, Go Igarashi, Tatsuto Haji, Takahiro Ohkubo, Sayuri Tomota and Ippei Maruyama., "Temperature-Dependent Water Redistribution from Large Pores to Fine Pores after Water Uptake in Hardened Cement Paste." *Journal of Advanced Concrete Technology*, vol. 18, no. 10, 2020, pp. 588–99, doi:10.3151/jact.18.588.

- Kiran, Rohith, Hamza Samouh, Akira Matsuda, Go Igarashi, Sayuri Tomota, Kazuo Yamada and Ippei Maruyama., "Water Uptake in OPC and FAC Mortars under Different Temperature Conditions." *Journal of Advanced Concrete Technology*, vol. 19, no. 3, 2021, pp. 168–80, doi:10.3151/jact.19.168.

List of Figures

List of Tables

List of Abbreviations

Cement chemistry nomenclature

C	CaO	Calcium oxide
S	SiO_2	Silicon dioxide
A	Al_2O_3	Aluminium oxide
F	Fe_2O_3	Iron oxide
S	SO_3	Sulphur trioxide
H	H_2O	Water
C_3S	$3CaO{\cdot}SiO_2$	Tricalcium silicate
C_2S	$2CaO{\cdot}SiO_2$	Dicalcium silicate
C_3A	$3CaO{\cdot}Al_2O_3$	Tricalcium aluminate
C_4AF	$4CaO{\cdot}Al_2O_3{\cdot}Fe_2O_3$	Tetra calcium ferrite-aluminate
CH	$Ca(OH)_2$	Calcium hydroxide
C-S-H	$CaO{\cdot}SiO_2{\cdot}H_2O$	Calcium silicate hydrate
C-S(A)- H	$CaO{\cdot}SiO_2{\cdot}(Al_2O_3){\cdot}H_2O$	Calcium aluminosilicate hydrate

^{1}H-NMR technique

^{1}H-NMR	(^{1}H) proton – nuclear – magnetic – resonance relaxometry
CPMG	Carr – Purcell – Meiboom – Gill
ILT	Inverse Laplace Transform
T_2	Transverse relaxation time
FID	Free Induction Decay
$T_{2,surface}$	Transverse relaxation time of monolayer surface adsorbed water
ε	Monolayer thickness of water molecules
S/V	Surface to volume ratio
d	Pore width
λ	Surface relaxivity ($\varepsilon/T_{2,surface}$)
W_L	Water in large pores
W_F	Water in fine pores
W	Evaporable water

X-ray Computed radiography technique

X - CR	X-ray computed radiography
SSD	Distance from the x-ray focus to the detector
SRD	Distance from the x-ray focus to the sample
G_{SV}	Grey value

W/C	Water to cement ratio
S/C	Sand to cement ratio
°C	Temperature
RH	Relative humidity
OPC	Ordinary Portland cement
FAC	Fly ash cement
LS	Lime stone
RS	River sand

1. Introduction

1.1. Research background

1.1.1. General buildings and Civil infrastructures

Cement is the binding agent of concrete, the world's most widely used man-made substance in the world, with one cubic meter generated per person each year. It is a low-cost and simple-to-use substance. Even though cement is a naturally low CO_2 substance when compared to all other frequently used building materials, the amount utilized contributes around 5% of world CO_2 emissions. [1]. Since the origins of construction materials science, one of its basic objectives has been the search for materials with given properties, to respond to the problems and needs that engineering has been raising. Obtaining materials with specific properties can be achieved through the discovery of new materials or through the modification of already known materials.

Portland cement is manufactured from a ground mixture of limestone and clay, or compounds containing calcium, silicon, aluminum and iron, in suitable proportions. This mixture is heated in a kiln at elevated temperatures (1500 °C) to produce a partial fusion of the materials, obtaining a product called clinker. The raw materials to produce clinker are containing these four oxides: CaO, SiO_2, Al_2O_3 and Fe_2O_3. From a mineralogical point of view, the main phases of clinker are: alite or tricalcium silicate (C_3S) at (50-70 %), belite or β-dicalcium silicate (β-C_2S) at (5-25 %), tricalcium aluminate (C_3A) at (0-15 %) and finally tetracalcium ferritoaluminate (C_4AF) and is found at (5-15 %). In addition, gypsum or calcium sulphate dihydrate is added at the end of the process in quantities of about (5 %) as a setting regulator, which, ground together with the clinker, constitutes the cement [2].

From a macroscopic point of view, the hydration of Portland cement at room temperature gives rise to a plastic and adherent product which sets both in air and under water in a few hours, but which hardens progressively until it acquires its fundamental properties: strength and durability. Similarly, if this process is observed from a microscopic point of view, the hydration of this material leads to the formation of a set of minority crystalline products (ettringite and portlandite) and a majority amorphous product, which is responsible for the aforementioned properties. This compound is a hydrated calcium silicate of variable composition, which according to the nomenclature of cement chemistry is called C-S-H [3].

1.1.1.1. Characteristics of hydrated cement paste

The cement hydration process can be defined as a set of chemical reactions between the different phases of clinker, calcium sulphate dihydrate and water, which lead to setting and hardening of the cement. The clinker phases have different hydration rates and can be ordered in the following order: C_3A, C_4AF, C_3S and C_2S. For this reason, it is appropriate to study the reactions between these phases and water. Starting with the most abundant phases, the hydration of the alite leads to the formation of calcium hydroxide (portlandite) and C-S-H (Calcium silicate hydrate), which is the product responsible for the bonding and strength properties of cement. C-S-H is an amorphous compound with a Ca/Si ratio varying over a wide range, so it lacks a general stoichiometric formula and is designated by C-S-H [2].

$$
\begin{aligned}
&C_3S + (3 - x + y)H \rightarrow C_xSH_y + (3 - x)CH \\
&C_2S + (2 - x + y)H \rightarrow C_xSH_y + (2 - x)CH \\
&C_3A + 3C\bar{S}H_2 + 26H \rightarrow 3C_6A\bar{S}_3H_{32} \\
&3C_6A\bar{S}_3H_{32} + 2C_3A + 4H \rightarrow 3C_4A\bar{S}H \\
&C_3A + CH + 12H \rightarrow C_4AH_{13} \\
&C_4AF + 2CH + 10H \rightarrow 2C_3(A,F)H_6
\end{aligned}
\qquad (1.1)
$$

Cement-based materials are basically composite materials, formed from the mixture of a hydraulic binder: cement , water and aggregates of different shapes and sizes . After a curing process, we have a solid and compact material, formed by a matrix of solid products that binds the aggregates. This solid matrix will be more or less porous, depending on the initial manufacturing conditions, the curing process to which it has been subjected, the environmental situation in which it is found, etc. In a very general way, the different phases that can be found within these materials are as follows[2][3][4]:

- Cement matrix: depending on the type of cement used, it will have different characteristics, but basically it is composed of a solid phase, pores and/or cracks and water. The solid phase generally contains hydrated calcium silicate (C- S- H gel), portlandite (CH), calcium sulphoaluminates (AFt , AFm) and unhydrated cement grains.
- Aggregates: these are the most homogeneous component of cement-based materials. They occupy most of the volume of these materials (between 60% and 80%) and largely provide the weight, modulus of elasticity and dimensional stability of these materials, as well as lowering the cost of the material. They exert a very positive

influence on the mechanical strength, shrinkage, creep, abrasion, and durability of these materials.

- Transition Interfacial Zone: This is the hydrated cement matrix found in the surface areas of the aggregates and which covers between 50 and 100 μm from the surface of the aggregate. It is a phase that conditions a large number of properties of these materials (durability, strength). Basically, it differs from the matrix, in its porosity and in the characteristics of the hydration products present, being, in general, this interfacial transition zone the weakest part of these materials.

Cement-based materials are extraordinarily complex and heterogeneous materials. They have a microstructure that evolves over time and is influenced by many variables, such as temperature, relative humidity, etc. The microstructure of these materials generally begins as an aqueous dispersion of a finely divided powder and aggregates of various sizes, and evolves into a solid mass, formed by a porous matrix of interconnected solid products and aggregate inclusions. As this microstructure is constantly changing and is extremely sensitive to treatment and storage conditions, it is extremely difficult to establish a precise characterization and therefore difficult to define relationships between the microstructure and the properties of these materials.

Beaudoin et al. [5], shows the different hydration rate of the basic cement components as well as the formation of the hydrated compounds(see Fig. 5.3 (A) in ref.[5]. Different reaction rates of each phase as well as the amount of each hydrated compound formed. It can be clearly seen that the major components are portandite (CH) and C-S-H gel. In addition to these major components, a number of other compounds can occur, such as ettringite (AFt phases), hydrated monosulphate (AFm phases) and other amorphous compounds (see Fig. 5.3 (B) in ref.[5]). Scrivener [6], shows the main components of a mortar in an electron microscopy image (see Fig.3 in ref.[6]).

Calcium silicate hydrate (C-S-H) is the major component of the hydrated cemnt paste, constituting (50 – 60 %) of the total hardened cemet paste and provides the hardened material with a matrix that connects and binds the aggregate together. The C-S-H nomenclature means that it does not have a defined stoichiometry and can have C/S ratio varying from 1.7 to 2.0 and very different structural water contents. C-S-H is an amorphous silicate that can undergoisomorphic substitutions, admitting considerable amount of other ions (mainly Fe and Al) into its structure. The term “C-S-H” is used to distinguish it from other phases. A large number of studies have been carried out on the mictrostructural characterization of C-S-H. There are different models and theories have been proposed to describe the structure of the C-S-H in Chapter 2.

1.1.2. Fukushima Daiichi accident

Nuclear power plant has six reactors each reactors successively commissioned during the 1970s. Unit1, unit 2 and unit 3 were operating at a full power the core at unit 4 was unloaded and unit 5 and unit 6 were in cold shutdown.

Following the accident at the Fukushima Daiichi nuclear power plant (FDNPP), a plan for decommissioning the plant must include an estimation of the level of contamination in the concrete due to the enormous quantity of material. As a part of the decommissioning, the Ministry of Education, Culture, Sports, Science and Technology of Japan (MEXT), conducted a project between January 2018 and March 2020 called "the analysis of radionuclide contamination mechanisms of concrete and the estimation of contamination distribution at the Fukushima Daiichi nuclear power station." To accurately assess the level of contamination in concrete structures, it is important to consider water transport and microstructural changes within the material. The concrete in the Fukushima NPP buildings has a relatively low moisture content after many years of service [7], [8] .

After the Fukushima Daiichi nuclear disaster in 2011, a project was undertaken to understand the fundamental mechanisms behind ion transport and the interaction between ions and concrete components, with the goal of aiding the decontamination, shielding, and disposal of concrete members affected by cesium and strontium at the nuclear power plant. For this, a reliable evaluation of the depth of cesium and strontium penetration in reactor building concrete was required [9][10].

The concrete in the nuclear infrastructure at Fukushima was dried over many years of service before the 2011 incident, then, portions of the surface were completely immersed in liquid water, going from a dried state to a saturated state via the water absorption process. For a typical case with no interaction between the fluid and and the material, the fluid transport should only depend on the liquid viscosity and the surface tension reflecting the intrinsic pore structure. This dependency is also observable for cement-based materials in capillary absorption tests when organic fluids are used, such as n-heptane, n-decane, n-dodecane, and ethanol however, when the fluid is water, the two-parameter dependency is no longer valid [11], [12]. A drop in the measured rate of water absorption compared to the theoretical prediction has been observed with a sorptivity that is lower by a factor between 1.5 and 2.

This special behavior of water transport in cement-based materials is generally qualified as "anomalous" [13][14], and should be distinguished from the saturation-dependent diffusivity, the sorption hysteresis, and the irreversibility of the first sorption cycle. This behavior was previously explained by a blockage in the porous network, which can have

different origins. The clearest is the delayed hydration of unreacted and dehydrated elements that creates new calcium silica hydrate (C-S-H) layers. For the origin of this behavior, the precipitation of the calcium hydroxide has also been suggested, as well as the swelling of the hydrate gel in contact with water. Additionally, microcracking caused by drying and shrinkage during the pretreatment phase are indicated to be susceptible areas to these microstructural modifications.

1.2. Objective

As a first step in the contamination estimation procedure, the water uptake behavior of materials similar to those used in the Fukushima Daiichi NPP buildings is studied. It should be mentioned that shrinkage-induced visible cracks as well as cracks around aggregate has a large influence on the moisture / liquid water transport in concrete, however, as a first step research program, several factors, which are originated from the characteristics of materials used in the Fukushima Daiichi NPP buildings, including temperature, drying conditions, and mortar composition are investigated. Regarding concrete in Fukushima daiichi accident, (1) Aging of concrete, (2) Heating due to accident and (3) Water supply for the accident are should be taken into account. In the present project, the molten core - concrete interactions is not the matter of concern. Due to the difficulty to obtain the precise history of temperature and humidity for the surface of each thick concrete wall in Fukushima daiichi plants, the project set the objective to obtain the scientific background data of interaction between dried cement paste and water as a first step. Consequently, the first drying at 105 °C is applied for the hardened cement paste and water suction measurement was conducted less than 60 °C to obtain the activation energy from there temperature conditions

In the context of nuclear power plants, capturing the temperature dependency of this dynamic microstructure (related data has been reported by [15]) is critical for a more accurate estimation of the moisture transport, such as in a recent trial by Li and Xu [16]. To the authors' knowledge, no similar data for mid-range periods have been reported thus far. The ^{1}H-NMR relaxometry technique is a noninvasive and nondestructive method in which the water is used as the probe and it is able to determine the dynamic porosity and water in different pores. Therefore, by using ^{1}H-NMR relaxometry, the temperature-dependent dynamic microstructure in hardened cement paste (hcp) is studied herein.

In this study, the porosity was initially extracted for four pores: capillary, interhydrate, gel, and interlayer. Then, to analyze the internal water exchange, the large pores are defined as the summation of the capillary and interhydrate pores, while the fine

pores are defined as the summation of the gel and interlayer pores. This bi-modal pore distribution has already been used and validated to analyze the microstructure of cement paste from ^{1}H-NMR measurements [17], [18]. The rate of water exchange between large and fine pores is calculated for three different temperatures. For many parameters with temperature dependency (such as permeability, diffusion, creep, and cracking), Arrhenius behavior can be observed. Thus, the activation energy of the rate of the internal water transport is estimated, allowing a better interpretation of the measurements. Furthermore, to understand the anomalous water transport behavior that was previously reported [12], [14], [19]–[25], a simplified numerical analysis is conducted. The behavior is investigated by considering dynamic microstructural changes in calcium silicate hydrate (C-S-H) [26]–[30], a major group of hydrates in cement-based materials that is influenced by variations in temperature.

1.3. Structure of the thesis

- The present thesis work is divided into five chapters including the present chapter which introduces to thesis problem that thesis work attempted to solve and a brief description of each chapter is provided below:
- Chapter 2 :- Literature review about the atomic scale of C-S-H structure, meso-csale modelling and Basics of ^{1}H-NMR relaxometry technique and the literature review of ^{1}H-NMR relaxometry in cement based materials. An existing theory, based on capillary tension as a driving force in the movement of liquids (Like organic, water) in cement based materials is discussed, followed by an overview of various techniques of measuring liquid movement by (Gravimetric, X-ray radiography and neutron radiography)
- Chapter 3:- Based on ^{1}H-NMR relaxometry technique, investigated the distribution of pore water (interlayer, gel, interhydrate and Capillary), pore size in cement paste under different temperatures (20 °C, 40 °C, and 60 °C) at different water to cement of (0.40,0.55). Pore water was divided into fine pore water (Sum of interlayer and gel) and large pore water (sum of interhydrate and capillary). The rate of water exchange was obtained showing an increasing temperature.
- Chapter 4 :- Based on X-ray computed radiography technique, investigated the ater uptake in OPC and FAC at different temperatures (20 °C and 60 °C). Sorpivity measurements showed that water transport displayed anomalus behaviour.
- Chapter 5:- Summary and future perspectives

2. Literature review on C-S-H

2.1. Atomic scale of C-S-H

The C-S-H originates in cement pastes through the hydration reactions of the calcium silicates in the clinker (alite and belite) [31]. These reactions can be observed in the chemical equations (as shown in **Eq.(1.1)**) described above. However, the kinetics of the hydration reactions of the calcium silicates in clinker are different, and so are the C-S-H that originate in each of them. The hydration of belite produces a different C-S-H gel to that from the hydration of alite in terms of Ca/Si ratio and chemically bound water [32]. The C-S-H originating from C_3S hydration has a higher Ca/Si ratio and consequently higher H_2O/Si ratio [33][34]. It should be noted that the Ca/Si ratio changes with hydration time, being initially higher, and lower as the hydration time increases[35][36][37].

The literature establishes that the Ca/Si ratio of C-S-H varies between 0.6- 2.3 depending on variables such as hydration time, the presence of additions, temperature, etc. It is also observed that the more mature paste, with longer hydration time, have lower calcium concentrations [38]. With regard to the presence of additions, if these are pozzolanic, they decrease the Ca/Si ratio [39]. When this type of addition is added, the Si-O and Al-O bonds of the pozzolan are broken by the attack of the OH^- ions coming from the portlandite. The silicate and aluminate ions present in the medium then react with each other and with the Ca^{2+} ions to finally form the C-S-H and C-S(A)-H.

Over the years, different classifications of calcium hydrated silicates (C-S-H) have been made based mainly on their Ca/Si ratio. The first classification was established by Taylor [40] and he called C-S-H (I) calcium silicate hydrates with a Ca/Si ratio ranging from 0.8-1.3, and C-S-H (II) those with a Ca/Si ratio ranging from 1.5-2.0. Kantro et al.[41] added to this classification the phase called hydrate (III), which was almost amorphous and had been observed in the hydration reaction of C_3S with water.

In 1998, Nonat made a different classification by subdividing the CSH (I) phase proposed by Taylor into two new ones: α-C-S-H when the Ca/Si ratio was less than 1.0, and β-C-S-H when the Ca/Si ratio was between 1.0-1.5. Thus, the CSH(II) phase proposed by Taylor was renamed as γ-C-S-H. Recently, through several solubility studies, Haas and Nonat [42] have described these three phases, α, β, and γ-C-S-H, as $Ca_4H_4Si_5O_{16}$, $Ca_2H_2Si_2O_7$ and $Ca_6(HSi_2O_7)_2(OH)_2$ respectively.

The existence of a great variety of commercial cements means that the C-S-H present in cement pastes have a great variability in terms of composition, structure, and microstructure. All this, together with the fact that the C-S-H has an amorphous nature,

means that its structure is not well known. Thus, it is not entirely well known to about the C-S-H , because this compound does not have a determined structure and composition, but rather presents a wide range of variation. Although, it is always referred as C-S-H.

Calcium silicate hydrate (C-S-H) can exhibit a wide range of Ca/Si ratios because its nature can be affected by many factors such as: initial cement composition, hydration time, water/solid ratio, degree of hydration, curing temperature and the presence of additives. All these factors influence the variation not only in composition, but also in structure and morphology [38]. For example, it is widely assumed that the Ca/Si ratio of the C-S-H gel from the hydration of the alite is 1.75 [43][44][45], although it can range from 1.2-2.1 within the same paste [37][46][47]. In addition, there are C-S-H samples with Ca/Si ratios ranging from 0.6-2.3; the first value of the range corresponds to cement containing additives such as fly ash, silica fume, metakaolin or granulated blast furnace slag, while the highest value of the range has been found in C-S-H from the hydration of Portland cement[38].

The chains that make up the C-S-H structure are not infinite. They have been empirically observed to have a given length of 2, 5, 8..., in general following the (3n-1) rule, where n is an integer [48][49]. Chain lengths from 2 for young pastes to 5 for mature pastes, and even longer than 20 for cements cured at high temperatures, have been measured experimentally.

Most structural models that attempt to explain the structure of the C-S-H are based on the structures of the 1.4 nm tobermorite [50] and jennite [51], because they have a layered structure that elongates in a certain direction producing a fibrous structure.

Richardson [52], the structure of 1.4nm tobermorite (as shown in Fig.2 in Ref[52]) is described as infinite chains of silicon tetrahedra [SiO_4] joined at the vertex in a dreierkette pattern, i.e. repeating in intervals of three tetrahedra. In each of these groups of three tetrahedra, two of them, called paired (P), share an oxygen with the central layer of calcium octahedra [CaO_6], while the third, called bridge (B), serves as a link between two adjacent tetrahedra, since it is not attached to the central layer. This structure of silicon tetrahedra together with the central layer of calcium octahedra is not directly joined to other structures of this type, but between one and the other, there is an interlayer or interlaminar space occupied by water molecules and Ca^{2+} ions. The structure of jennite can be explained in a similar way to that of 1.4 nm tobermorite. The fundamental difference is that in this case, half of the oxygen atoms in the core layer are shared with the silicon tetrahedron chains, while the other half is bound to OH^- groups.

Cement possesses other ions, such as Al^{3+} which are susceptible to incorporation into the C-S-H gel structure [53]. Thus, the proposed models have to be consistent when the

substitution of Si^{4+} for Al^{3+} occurs, which only occurs in the bridging tetrahedra or in the central tetrahedron [53][54][55][56][57].

2.1.1. Infinite chains

The first structural model based on infinite chains was proposed by Bernal et al.[58] in 1952. They carried out the synthesis of two compounds called calcium silicate hydrate (I) (CSH (I)) and calcium silicate hydrate (II) (CSH (II)), which had low and high Ca/Si ratios respectively[40]. Through X-ray diffraction, they determined that CSH (I) showed a layered structure, which elongated in a certain direction resulting in a fibrous structure very similar to that of the mineral 1.4 nm tobermorite and whose structure was described by Megaw and Kelsey[59].

Kurczyk and Schwiete [60], proposed a model another structural model based on infinite chains. The authors studied the hydration products of alite and belite using various techniques and proposed an identical structure for the products obtained in both systems. This structure was lamellar and based on that of the mineral 1.4 nm tobermorite, with the particularity that Ca^{2+} and OH^- ions, as well as water molecules, could be included between the mineral layers. The authors established the stoichiometric formula for calcium silicate hydrate, which is consistent with the solubility experiments carried out by Kantro et al.[61], in which they described that between the tobermorite layers there were included portlandite layers.

2.1.2. Monomers, dimers and polysilicate chains

Some authors have proposed models involving monomers,dimers or polysilicates to explain the structure of C-S-H.

After publishing the first model based on infinite chains of silicon tetrahedra. Bernal [62], developed another model based on the monomeric units of silicate anions. The author explained that in the hydration reaction of the alite has two phases called hydrated calcium silicate (I) and hydrated calcium silicate (II) originated, which included the monomer $[SiO_2(OH)_2]^{2-}$. Thus, he proposed the following structural formula for the C-S-H: $Ca[SiO_2(OH)_2][Ca(OH)_2]_x[H_2O]_y$, where x and y represent the number of portlandite and water units, respectively.

This model was based directly on the one proposed by Kurczyk and Schwiete [60] and proposed a structure analogous to that of the mineral 1.4 nm tobermorite, with the difference that the chains were not infinite. The authors proposed that the structure of the CS-H gel was built from CaO_x polyhedra between two silicate chains.In addition, the authors added that Ca^{2+} and OH^- ions, water molecules and other ions could be included in the

interlaminar spaces. Stade and Wieker [63]explained their model in two different ways, both of which were based on the same hypotheses. One described the C-S-H gel by purely dimeric units, while the other described it from dimeric units and polysilicate anions. Thus, the simplest structural formula for the C-S-H described by the dimer-only model is: $Ca_{4+y}(OH)_z[(H_{1+x/2}Si_2O_7)]_2 \cdot mH_2O$, where x, y, and z take values within certain limits.

Glasser et al.[64], proposed a structural model based on dimeric units, which was derived from the one previously developed by Stade and Wieker. Due to the thermodynamic treatment of the proposed model, it was only applicable to C-S-H gels with a Ca/Si ratio between 1.0-1.4, although the authors considered that it was equally applicable to young C-SH gels, i.e., of short hydration times. Glasser et al. [64] expressed the difficulty in writing the equations for the formation and dissolution equilibria of the C-S-H but proposed the following structural formula for it: $Ca_xH_{6-2x}Si_2O_7 \cdot zCa(OH)_2 \cdot mH_2O$, where x, z are variables that take on values within certain limits and are linked to the Ca/Si ratio, but do not have the same meaning as in the Stade and Wieker model.

Grutzeck [65], proposed a new structural model for the C-S-H based on two compounds. One, with a high Ca/Si ratio, was composed of sorosilicates or dimeric units. while the other, with a low Ca/Si ratio, was composed of longer chains of the 1.4 nm tobermorite type. The author proposed that the initially formed C-S-H gel presented a sorosilicate structure, as supported by 2D NMR experiments carried out by Rakiewicz et al.[66] which confirmed that in the newly formed C-S-H gel, there were only two types of bonds in which deuterium was involved: $Ca(OD)_2$ and D_2O. Grutzeck[65] also explained that some parts of the dimeric structure of the C-S-H eventually underwent a change to a longer chain structure of the 1.4 nm tobermorite type.

2.1.3. Rule of (3n-1)

Models based on the (3n-1) rule are the most accurate in describing the structure of the C-S-H .

Taylor and Howinson [67] proposed a model to describe the structure of the C-S-H gel, which was based on the phases previously described by Bernal in his two earlier models.52,79 The authors made some modifications to the structure of the 1.4 nm tobermorite. Taylor and Howinson [67] model was the one that best explained the structure of the C-S-H gel, since it established a dreierkette structure for this compound, which additionally obeyed the (3n-1) rule, that is, the chains of tetrahedra were not infinite, but formed dimers (n=1), pentamers (n=2), octamers (n=3), etc. It was also the basis on which Taylor later proposed his new structural model. The latter model is based on 1.4 nm tobermorite-type layers intermixed with jennite-type layers. Taylor [67] assumed that each

bridging tetrahedron is bonded to a single hydrogen atom, and that when such tetrahedra are omitted, only one of the broken ends of the chain remains bonded to a hydrogen atom. Thus, the charge remains unchanged and the removal of a bridging tetrahedron is not associated with the need to vary the amount of calcium located in the interlayer. However, the author stated that there was no direct evidence to justify this behavior, although the chemical structure and composition were reasonable and led to results that agreed with the experimental data. Taylor also found by X-ray diffraction experiments and thermogravimetric analysis that the structure of the C-S-H gel consisted of finite chains containing 2, 5, 8..., in general, (3n-1) silicon tetrahedra. This was consistent with the silicate anion structure that had been observed in the hydration products of alite and Portland cement pastes . In addition, the author calculated the different Ca/Si ratios for 1.4 nm tobermorite and jennite dimers, pentamers, octamers, etc., by fixing their degree of protonation [68]. Taylor proposed that the Ca/Si ratio of a C-S-H in young pastes is obtained by mixing 1.4 nm tobermorite and jennite dimers, while for mature pastes, the Ca/Si ratio of such a C-S-H gel is obtained by mixing larger polymers (pentamers and octamers) and to a lesser extent dimers [69].

Richardson and Groves (R-G)[70][71], explains the structure of the C-S-H on the basis of results obtained by ^{29}Si nuclear magnetic resonance and transmission electron microscopy. This model is based on an extremely disordered layered structure, consisting of finite chains of silicon tetrahedra of length (3n-1) interstratified with layers of a solid solution of portlandite. In this way, the authors succeeded not only in varying the number of hydroxyls attached to the silicon atoms, but also the amount of portlandite, and based on previous work [72]. They established the following structural formula for the C-S-H gel: $Ca_x H_{6n-2x} Si_{3n-1} O_{9n-2} \cdot zCa(OH)_2 \cdot mH_2O$, where n represents the length of the silicate chain, x the amount of calcium required for the charge balance of the silicate chain, z the amount of portlandite and m the amount of water molecules bound but not as hydroxyl groups. At this point, it can be seen that the Richardson and Groves model is related to some previously proposed models. Thus, the model of Glasser et al. [64] is a particular case for dimeric chain C-S-H gels (n=1) and the model proposed by Taylor [68] is a specific case of the Richardson and Groves model when x=2.5n since the amount of calcium does not vary with the omission of the bridging tetrahedra. The proposed model has maximum versatility in the degree of protonation of the silicate chains, since the formulae of the 1.4 nm tobermorite and jennite can be deduced from the initial formula considering that z=0 and z=2n respectively: $T_{3n-1}=Ca_{2.5n}H_nSi_{(3n-1)}O_{(9n-2)} \cdot mH_2O$ and $J_{3n-1}=Ca_{2.5n}H_nSi_{(3n-l)}O_{(9n-2)} \cdot 2nCa(OH)_2 \cdot mH_2O$. From these equations the general equation of this model can be rewritten, taking into account the degree of protonation of the silicate chains, as: $\{Ca_{2n}H_wSi_{3n-1}O_{9n-2}\}(OH)_{w+n(y-2)} \cdot Ca_{ny/2} \cdot mH_2O$,

where n represents the length of the silicate chain, w the number of silanol groups, w/n the degree of protonation and y the amount of calcium that offsets the charge of the silicate chain or is present as portlandite. The C-S-H can incorporate or have intermixed layers of AF_m phases and calcium and magnesium hydroxides among other elements, as has been verified by XRD. However, the main ion that can be incorporated into its structure is Al^{3+}, and the Richardson and Groves[71] model is able to explain the incorporation of ions into the C-S-H structure. Through ^{29}Si and ^{27}Al MAS-NMR experiments, the coordination of aluminium atoms in the C-S-H gel structure was studied and it was concluded that they could occupy tetrahedral and octahedral positions. However, it was established that aluminium atoms could only replace silicon atoms occupying the position of the bridging tetrahedra, so that there would be no deviation from the (3n-1) rule.

Cong and Kirkpatrick (C-K) [73][74][75], proposed a model for the C-S-H based on a 1.4 nm tobermorite-like layered structure, but much more disordered and containing a larger number of defects. The authors suggested that these layers could be of two different types: some were almost perfect but without some bridging tetrahedra, resulting in disorder and depolymerisation, while the others were very disordered, contained mostly dimers, and some tetrahedra could be tilted, rotated, and even displaced from the plane of calcium octahedra. The two types of layers could merge or occur together in the same layer. In addition, different types of layers could be stacked together, or be present in separate parts of the same sample. All this led to an increase in the diversity observed in different C-S-H structure (as shown in Fig. 6 in Ref . [74]) The authors based their model on several X-ray diffraction and nuclear magnetic resonance experiments of ^{29}Si and ^{17}O with magic angle spinning, and the equations they used to describe the relationship between the structure and composition of the C-S-H gel in their models. As shown in **Eq.(2.1)**, where r represents the initial Ca/Si ratio and m the number of bridging tetrahedra removed. The variable limits of the Richardson and Groves [70][71] model are equivalent to the defects proposed by Cong and Kirkpatrick[73][74][75]. Thus, Cong and Kirkpatrick state that Ca^{2+} ions are the ones that counterbalance the charge of the silanol groups that are missing a proton, forming -Si-O-Ca.

$$\frac{Ca}{Si} = \frac{r}{1-\frac{m}{3}} \qquad MCL = \frac{Q_1}{Q_1+Q_2} = \frac{2}{\frac{3}{m}-1} \tag{2.1}$$

Chen et al. [76], a new structural model was presented and was based on x-ray

diffraction experiments, ^{29}Si nuclear magnetic resonance with magic angle spinning and solubility studies. The model explained that the C-S-H structure could be described as a 1.4 nm tobermorite, jennite or a combination of both (y=2 and w/n=0), all with a large number of defects. The authors discussed two different ways in which the Ca/Si ratio of the C-S-H gel could be varied, one by the formation of -Ca-OH bonds, and the other by the loss of protons from the silanol groups. However, although the model was consistent with the experimental data, their arguments were not significantly different from those proposed by Richardson and Groves[70][71].

Recently, Grangeon et al. [77][78] based on ^{29}Si nuclear magnetic resonance and X-ray diffraction experiments, have proposed a structural model of the C-S-H gel that evolves as a function of the Ca/Si ratio. When the Ca/Si ratio is low, the C-S-H can be described as a 1.4 nm tobermorite nanocrystalline. As the Ca/Si ratio increases, depolymerisation of the structure occurs through the omission of some bridging tetrahedra. This leads to a weakening of the interlayer bonds, resulting in an increase of the interlayer distance. In addition, stacking defects are created, resulting in a change in the Si-O-Si angle. A further increase in the Ca/Si ratio leads to the progressive incorporation of Ca^{2+} into the interlayer, leading to a decrease in the interlayer distance until they are joined together. This connection is produced by the bonding of the Ca^{2+} ion coordination spheres, which form a layer that has many similarities with nanocrystalline portlandite. Although this model has many similarities with that of Richardson and Groves [70][71] these authors consider a certain structural order.

2.2. Meso-scale modeling

Calcium silicate hydrate (C-S-H) models attempts to explain the structure from another point of view. They aim to propose a model that with various properties of C-S-H such as density, porosity and specific surface area and that is related to the microstructure of the C-S-H. some of these models are listed below.

2.2.1. Powers and Brownyard model

One of the first known model is Powers and Brownyard [79]. It is a model that describes the hardened cement paste in a general way, as consisting of three components from a volumetric point of view: unreacted cement, hydration products and capillary pores. All solid products are not considered individually, but as “hydration products”. Furthermore, the volume available for the formation of hydration products is only that which is occupied by water. If the water to cement ratio is below 0.39, complete hydration of the cement is not

possible. Powers [80], proposed a structural model for cement gels (C-S-H gels) as shown in **Figure 2.1**. With the contributions of Brunauer[81], based on the measurements of water adsorption isotherms and bound swater content of cement paste. Author described the C-S-H gel as consisting of gel particles and gel voids between the particles. The C-S-H gel particles are composed of two or three layers of C-S-H gel particles bound together by surface energy. Powers has shown that osmotic pressure does not break the bonds of cement paste. Powers suggested that the osmotic pressure did not break the bonds in the cement paste, suggesting that there were chemical bonds within the small pieces. The hysteresis loops observed sin water vapour adsorption and nitrogen adsorption have the same shape as those of materials with slit-shaped voids. The hysteresis loops observed in water vapor adsorption and nitrogen adsorption have the same shape as those of materials with slit voids, suggesting a C-S-H layered structure. In addition, the specific surface area values obtained by water vapor adsorption The distance between the calcium silicate layers was estimated to be about 18 Å based on the specific surface area The distance between the calcium silicate layers was estimated to be about 18 Å. Water can enter all the spaces including the C-S-H interlayer, but nitrogen can enter only the coarse spaces. Water can enter all spaces including the C-S-H interlayer, but nitrogen can enter only coarse spaces, so the specific surface area by water vapor adsorption is the true value and that by nitrogen adsorption is the true value. The specific surface area due to water vapour adsorption is the true value and that due to nitrogen adsorption is smaller than the true value. The interlayer water is retained until it is strongly dried. Powers and Brownyad assumed that interlayer water is retained until subjected to severe drying, but is non-recoverable once lost. Powers and Brownyad classified water in cement pastes into three types.

- Structural water (crystalline water, chemically bound water and non-evaporative water)
- Gel water (adsorbed water, water bound by physical surface energy)
- Capillary water (free water in voids)

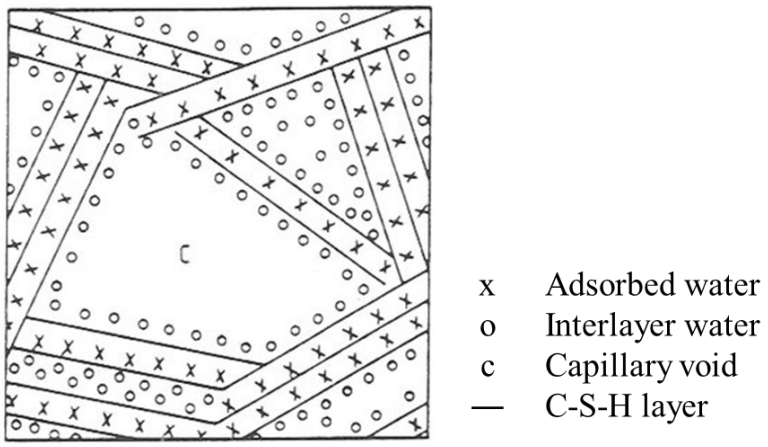

Figure 2.1 Powers schematic doiagram of C-S-H gels, interlayer water, adsorbed water amd capillary voids [80]

However, the authors could not determine the size of the particles. Because the optical microsopes did not have such a high resolution, which was the limitation for the model as the size of the particles could not be determined directly. Another limitation of this model is that it is unable to account for the irreversibility of water vapor adsorption isotherms. The fundamental consequence of these drawbacks was that it was unable to explain the nature of the bonds that are present in hydrated cement paste due to the extremely imprecise determination of pore size and surface area in the pastes.

2.2.2. Feldman and sereda model

Feldman and sereda [82] [83][84][85], proposed the C-S-H microstructure model as shown in **Figure 2.2** . Basee on various adsorption isotherm experiments with helium, methanol and nitrogen to perform porosimetry and density measurements of the C-S-H.
Their results demonstrated the dependence between mechanical properties of the hardened cement paste and transport characteristics of water in its different forms within the paste. The authors suggested that when the C-S-H gel collapses, water cannot re-enter the pores [86]. However, the aggressiveness of the drying conditions has been criticized by some authors because it causes partial loss of water from the C-SH structure [87]. The F-S model described that the water molecules in the interlayer of the C-SH gel were part of the structure of this composite and therefore, their possible removal would affect its mechanical properties. In addition, they attributed as valid for surface area measurements only the external surface of the material.

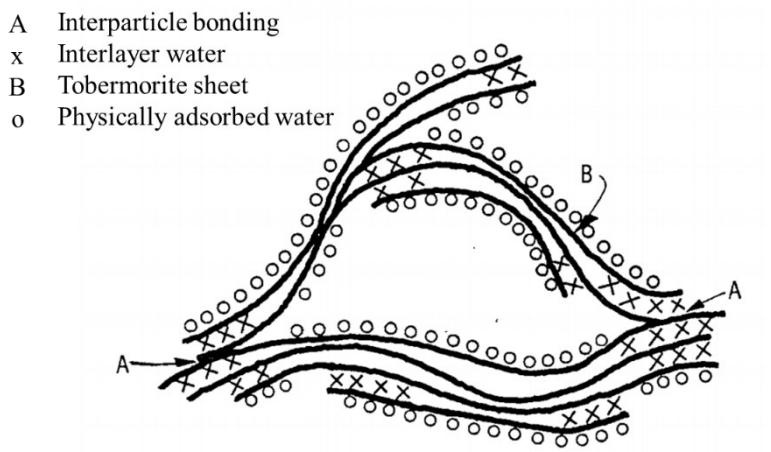

Figure 2.2 Feldman and Sereda schematic diagram of C-S-H sheets and interlayer water, Interparticle bonding and Physically adsorbed water [82]

Daimon et al.[88], investigated the nature of the pores of the C-S-H structure through nitrogen and water vapor adsorption isotherms. These authors established that the pore size was smaller than previously measured. Since the C-S-H gel formed could be encapsulated by the portlandite and make it more difficult for the adsorbate to reach all the pores of the material. They suggested that more accurate results could be obtained by resorting to extraction treatments of the portlandite. Thus, they measured the porosity between C-S-H gel particles and established two types of pores as shown in Fig.4 in Ref [88]):

- Intracrystalline pores: They are similar to the interlayer space established in the F-S model.
- Intercrystalline pores: They are similar to the micrometric pores described by Brunauer.

However, the lack of resolution of electron microscopy at the time did not allow confirming the characteristics of the pores, the type of water and solid matter that were part of the C-S - H structure.

2.2.3. Wittmann model

Wittmann [89], proposed a model, called the Munich model, in which he stated that the C-S-H gel had a three-dimensional structure of colloidal particles called xerogel. This model suggests that the gel particles are separated by thin sheets of strongly adsorbed water that adopt a repulsive behaviour to counteract the attraction due to the attractive

forces of the C-S-H gel particles. Through adsorption isotherm measurements, the author explained that the creep was due to the decrease in pressure, as the bonds between C-S-H gel particles were weakened but not between the layers. However, although this model explains the pressure decrease in the high humidity regions of the adsorption isotherms, it does not solve the problem concerning the nature of the pores and the creep under load or drying shrinkage induced by changes in the pores and the C-S-H gel structure.

Allen et al. [90], using a low-angle neutron diffraction (SANS) and specific surface area experiments, were able to observe changes in the microstructure of cement pastes. They concluded that the size of the C-S-H gel particles was 5 nm and that they formed clusters of about 40 nm in length. This study was not only the forerunner of modern colloidal models, but also marked the beginning of C-S-H classifications based on packing criteria rather than Ca/Si ratio.

2.2.4. Colloidal model (CM-I and CM-II)

Jennings, Tennis and Thomas developed the most important model called colloidal model (CM-I)[91][92][93][94] though a low angle X-ray diffraction (SAXS) and low angle neutron diffraction (SANS) techniques. Jennings determined that the basic units of the C-S-H gel were spherical, very dense and approximately 2.2 nm in diameter [90]. These spheres clustered to form globules of 5.6 nm in size, and these in turn could be grouped in two different ways, giving rise to two types of gels, one low-density (LD) and the other high-density (HD). These spheres clustered together to form globules 5.6 nm in size, and these, in turn, could cluster in two different ways to form two types of gels, one low density (LD) and one high density (HD) (as shown in Fig.3 in Ref.[91]). The distinction made between the two gels is based on the results obtained by nitrogen adsorption isotherms. Thus, density is associated with the surface area accessible to the gas; high density implies lower porosity and lower nitrogen accessibility. Through these tests, Tennis and Jennings estimated the relative ratio and variation with hydration time of (LD) and (HD) C-S-H [92]. C-S-H (HD) is considered to form at the anhydrous surface interface while (LD) C-S-H forms in the matrix and is present in greater quantity at earlier ages. As hydration time increases, the density of the gel increases and, therefore, the number of interparticle contacts increases[95].

The spaces between the smaller units are analogous to the interlamellar space of crystalline models; thus, the space between globules is assimilated to the intrinsic porosity of the C-S-H gel and the space between LD and HD particles corresponds to the capillary pores. Depending on the packing of these globules, two different situations can occur (as shown in Fig.3 in Ref.[91]).

- Interglobular arrangement: cement paste with low porosity and high density.

- Intraglobular arrangement: cement paste with high porosity and low density.

Subsequently, Jennings et al.[96] developed a colloidal and fractal model based on three different techniques: changes in length and weight during equilibrium drying, low-angle neutron diffraction and nanoindentation. The two variations in this model are the change in dimensions of the basic unit of CM-I from 2.2 nm to 4.4 nm, and the consideration that the space left when water is removed from the internal structure is not a pore. As in CM-I, the globules can be grouped in two different ways and generate the LD and HD structures of the C-S-H. However, in this case, the LD gel is described by a fractal model from a growing and connecting structure (as shown in Fig.5 in Ref [96]). As a continuation of the model, Allen et al.[97] through low-angle X-ray diffraction and low-angle neutron diffraction experiments determined the average particle formula of the C-S-H: $(CaO)_{1.7}(SiO_2)(H_2O)_{1.8}$.

Jennings [98], published a another colloidal model, which he described as an extension of the first one, calling it colloidal model II (CM-II). This model is a combination of the F-S model and CM-I, as it describes its structural unit as a brick-shaped grain or particle 4 nm long, but consisting of several 1.4 nm tobermorite-like layers. These layers are spaced by interlamellar water, and the whole unit is coated with a monolayer of water as shown in Fig. 5 in Ref. [98]). Moreover, these structures are linked together and generate three types of pores: intraglobular pores (IGP) less than 1 nm in size, small pores (SGP) with a dimension between 1-3 nm, and large pores (LGP) with a size between 3-12 nm. However, some authors have shown that both CM-I and CMII are unable to describe the C-S-H gel shrinkage phenomenon and explain the rearrangement process to form these structures. In this sense, further studies are needed regarding the role of water in the structure of this compound.

2.2.5. Other models suggested by ^{1}H-NMR relaxometry

C-S-H is now thought to be made up of nano -crystalline layers of material comparable to tobermorite and jennite. Calcium and oxygen atom sheets, as well as silicate tetrahedra, make up these minerals. Water may be found in three locations. Between the silica and calcium layers in C-S-H is intra-C-S-H or sheet water. Water between the locally aggregated C-S-H sheets and water between the nano-crystalline areas is known as inter C-S-H or gel water. It's still uncertain if these regions are individual granules (Colloidal models,[91][98]). Mcdonald et al.[99] propose a Feldman-Sereda-like model. C-S-H is made up of tetrahedral silica layers sandwiched between calcium and water ions. Intra-C-S-H water is the name given to this kind of water. Inter-C-S-H gel water is created by stacking C-

S-H sheets with water between them. Planar pores include both intra (sheet) pore and inner (gel) pore (as shown in Fig.2 see in [99]).

There should be a common nomenclature for future reference. When C-S-H is described as an layers, it is referring to its atomic structure. The word sheet, gel, interhydrate and capillary pores will be used to describe water in the same way that as described by [99] [100][101].

2.3. Dynamic microstructure based on ^{1}H-NMR

Earlier in Japan, Kawachi et al. [102], investigated the cement paste based on the ^{1}H-NMR relaxometry. To study the ratio between the chemically bounded water and free water as a function of hydration. Later on, Blinc et al. [103], published the early NMR measurements of evaporable water in cement pastes. From 10 minutes to after mixing to 28 days of hydration, these researchers calculated the so-called ^{1}H T_1 and T_2 relaxation time of water in cement pates. The various phases of hydration have been described. On the other hand, the author did not divide the signals into components corresponding to various microstructural conditions. The subsequent significant study was conducted by Schrenier et al. [104] was the first author to quantify the the different magnetization fractions for the first time. They included water in micropores at T_1 = 5 ms, which slightly decreased in an amount beyond 10 hours of hydration. Secondly, a substantial gel component at around T_1 = 1 ms, which at 10 hours already represented more than 50% of the ^{1}H protons and is described as C–S–H gel structural water. Finally, a substantial magnetization component with a growing spin-spin relaxation time representing protons of substantial OH^- groups such in $Ca(OH)_2$. The latter population increased in amount with the time of hydration. Lasic et al. [105], monitored the evolution of T_1 relaxation times of a synthetic white cement of (w/c = 0.42). Initially, two populations had been observed with the T_1 of approximately 100ms and between 18-25ms. These corresponded to water between the cement grains and the early crystalline products. This study demonstrated the first pieces of evidence of growing the C-S-H water by the NMR. Moreover , Miljkovic et al. [106] separated the signals from the tightly bound ^{1}H protons using the FID pulse sequence. The T_2 decreased beyond 8 hours of hydration, as was already observed by [103]. This study revealed that signal arising from the solid-like protons grows at the expense of signals from the liquid-like protons in the whole hydration process. Furthermore, the study pointed out the correlation between the liquid-like T_2 and the amount of water used in the mix proportions. Halperin et al. [107] presented the inversion of the CPMG decay into a pore volume distribution function using the fast exchange model for the first time. The first to relate calculated

relaxation time to pore size and surface area in the cement using quick exchange principle and the concept of relaxation at surfaces. Most writers opted to calculate T_2 rather than T_1 over time since it is a simpler experiment and the chemically mixed water in crystalline solids is easier to distinguish from water in large pores. Greener et al.[108] and Holly et al.[109], monitored the T_2 relaxation time in cement paste was studied using the "cross-standarized" mixture of two NMR approaches of FID pulse sequence and CPMG – to improve the quantification of the crystalline solids, and discovered five T_2components. They are crystalline solid, inter-layer pore water , gel pore water, capillary water, and water correlated with ettringite to monosulphate conversion in ascending order of T_2 in the maturing paste, but only the first four components occur in the mature paste.

In recent years, many researchers are used Nuclear magnetic resonance (^{1}H-NMR) relaxometry to measure the water distribution in cement paste and mortar specimens under different drying conditions.

Muller et al.[110], investigated based on the relaxation rates, pore sizes can be calculated and porosity ranging from 1nm to 10 μm can be probed by the ^{1}H NMR. The main advantage of the method lies in unneccesity of drying, which may alter the microstructure of C-S-H gel, prior application of this measurement technique. On the other hand, since this technique is based on measuring of hydrogen atoms, empty pores filled with air (void pores) cannot be detected by this method. Author composed his results with other techniques and concluded that only desorption isotherm technique can measure gel pores properly. Muller et al. [111], compared the NMR results to the results of other studies such as X-ray diffraction and thermogravimetric analysis to show how the density of hydrates could be calculated alongside the pore size distribution. The same authors later published findings from pastes containing silica fume [112] and demonstrated the calculation of a pore size resolved desorption isotherm in cement paste [113] [114]. Maruyama et al.[29], investigated under different drying conditions of (RH -80%, RH -40 % and RH – 11%). Based on their data, initially the water in interlayer pore water was increased, gel pore water, interhydrate pore water and capillary pore water was decreased. After reaching the interlayer peak up to 9 hours, then the water in interlayer was decreased significantly at RH – 40% and RH – 11% but at RH -80%, the interlayer pore water has increased up to 56 days.

Moreover, Fischer et al.[115], Schulte Holthausen et al. [116] recently demonstrated the advanced characterizations allowing a better understanding of the impact of parametes on the water exchange process. For instance the effect of pre-drying at 40 °C, 60 °C, 105 °C, and rewetting, evolving on a time period of 1 to 2 days, that the gel pores collapsed during drying and swell back to anything close to the original size. Gajewicz et al.[100] investigated that the water is redistributed from large pore water to fine pore water

at different drying conditions. Based on their data, gave a 2-cycle water redistribution for various cement paste measured by the salt-saturated solutions of relative humidity (RH-23%, RH-15%) and an oven drying of cement paste at a temperature of (60 ℃, 40 ℃) (see Fig.4 and Fig. 5). The results showed that the water is redistributed if the drying procedure is sufficiently gentle, and an irreversible change of microstructure occurs.

Other notable work includes McDonald, Korb, and co-workers T_1-T_2 correlation and T_2 -T_2 exchange studies[117][118] which measured the rate of water exchange between pores in fully saturated cement pastes. This suggested the exchange of water or hydrogen between different pore-size reservoirs. When the T_1-T_2 spectra of white cement and white cement with 10% silica fume showed that the silica-induced sample has less discrete diagonal peaks compared to the white cement. For paste with silica the off diagonal peak shifts towards a longer T_1 early on and this means hydration is faster in this paste.

2.4. Anomalous behaviour of water uptake

Based on Hall et al.[119] investigations, ASTM C1585 was developed and became a standard code in 2004. In unsaturated conditions, this test measures the rate at which water is absorbed by concrete samples due to the capillary forces. This rate is known as sorpitivity. The ASTM C1585 Standard specifies that the test be performed on disc concrete specimens with a diameter of 100 ± 6 mm and a length of 50 ± 3 mm. These samples may be taken from molded cylinders or concrete part drilled cores. For three days, samples should be conditioned in an atmosphere with a temperature of 50 ± 2 °C and a relative humidity of 80 ± 3 %. This preconditioning provides samples with an internal relative humidity of 50 % to 70 %, which is found to be the standard RH in the covercrete zone of certain in-field structures. ASTM C1585 are standard methods for concrete water absorption. Concrete samples should be acclimatized in specific environmental conditions to achieve a specified internal relative humidity prior to the test process, and the test should be conducted at Normal laboratory temperature, according to these Requirements. ASTM C1585, a laboratory test tool, is the most widely used method. The relationship between the sum of absorbed water plotted against the square root of time is explored in this method to assess the sorptivity value of concrete. The slope of the resulting line that suits the points is the sorptivity. Parrot [120], The rate at which water is absorbed into concrete by capillary suction will reveal important details about the pore structure, permeation characteristics, and toughness of the penetrated concrete surface zone. The most significant drawback of this approach is that it is destructive when applied to existing concrete structures. Although the preconditioning technique produces an internal RH of 50 to 70% for concrete samples, this is not the RH of field concrete elements under all environmental conditions. According

to Parrot [121] three days of drying at 50 °C followed by four days in a sealed container would result in fair moisture uniformity. The one-month period used in this study is longer than the ASTM C1585-recommended 15-day period. After the sorptivity testing was finished, the specimens were oven dried for three days at 110 °C to obtain dried mass in order to obtain saturation degree. Furthermore, another collection of specimens was dried to a particular moisture content (for 7 days) before being checked at three different temperatures of 5, 23, and 40 °C. To maintain the same temperature state, samples, water, and instrument parts were stored in the proposed testing temperature for at least 24 hours prior to testing. The dependency of the WSC on the moisture content of the samples [120] was a major obstacle to the standardization of the examination. The drying at 105°C is normally considered a reproducible precondition, however the change in pores structure contributes to unrealistically high WSC values due to hydration products degradation. Hall et al.[122], investigated that the capillary absorption of organic liquids such as (n-decane, n-heptane, n-dodecane and ethanol) and water by gravimetric method. Samples are dried at 40 °C and 105 °C for 24 h. Cement-based materials depends only on liquid viscosity and surface tension reflecting the intrinsic pore structure. In case of organic fluids, a linear relationship is obtained between the sorptivity and $t^{1/2}$. But in the case of water, the relationship between the sorptivity and $t^{1/2}$ deviates from the linear relationship. Based on theoretical and measured rate of water absorption is inferior, which is explained by the strong and fast interaction between hardened cement paste and water. This difference can be explained by the hydration of unreacted and dehydrated elements in cement matrix, the swelling of cement gel in comparison almost no swelling is observed in organic fluids and the corresponding microstructure alteration. It should be noted that the dependency of sorpivity test on pretreatment conditions. In case of water, depending on the liquid viscosity and surface tension it is not observed, and which is called as anomalous behavior. According to Marty's and Ferraris [19], the rise in sorptivity within a day tends to be linear, accompanied by a sudden decrease in sorptivity within a day. An experiment is performed for more than 200 days with negligible gain in mass. seem to indicate an initial linear plot of sorptivity accompanied by a sudden slope decrease within a day. The test continues for more than 200 days, with a moderate rise in mass. The evaporation at the exposed end will continue the transport of water, but with little change in mass. The findings after the front approach to the physical end of the sample are of little significance. Peter et al. [123], investigated the measurement of the effective porosity of the concrete is a measure of the degree of durability that these guarantee to the concrete and reinforced concrete structures against aggressive agents. The sorptivity is related mathematically to the diffusivity hydraulic, which is used to model the moisture transport in porous medium may be in

porous medium can be determined by the unsaturated flow theory describes the capillary flow process in porous cementitious materials. Applying Darcy's equation, modified for capillary flow in unsaturated materials, the diffusivity is related to the water content. The experimental study which was carried out on concretes of various qualities contributes to a better understanding of the link between sorptivity and capillarity. It has been observed that the sorptivity measured on dry concretes increases with their porosity while the capillarity coefficient reveals a bell effect. Tests were also carried out on damaged concrete. It has been observed that in the case of a globally diffuse damage, the links between sorptivity and capillarity are not necessarily upset insofar as the damage tends to increase both the sorptivity but also the capillarity. A high degree of saturation, of the order of 90%, was also investigated. However, the results of this test are not detailed here since the presence of a significant water gradient at the edges of the test body was suspected; then making the absolute values of sorptivity and capillarity difficult to interpret. Later Taylor et al.[12], investigated that the anomalous behavior by a partially substituting of Portland cement by less reactive cementitious materials as granulated blast furnace slag. Since only the low density CSH is involved in the macroscopic shrinkage and swelling, the observed reduction can be explained in this case by the corresponding lower ratio of low to high density CSH. Andrade et al.[124] Drying at low temperatures is more difficult to reproduce, but it is a sufficient technique to obtain a practical WSC. That the concrete be pre-conditioned to achieve a degree of saturation equal to that which occurs when it is in balance with the atmosphere at RH = 75%. For this purpose, the first criterion is to determine the water loss of saturated concrete when it is dry in the atmosphere at RH = 75%, and this relative water loss is repeated in the samples by means of an accelerated process utilizing an oven at 50 °C. Pre-conditioning is finalized by a redistribution process of moisture. Wong et al.[125] Drying at 105 °C leads to the intertwined microcracking, averaging 0.5–10 μm cracking width. There is also a much less frequent record of microcracking with a drying time of 50 °C. As a result, when drying temperature is raised from 50 °C to 105 °C, the WSC may be increased 100 percent. Wu et al.[126] conducted a one-dimensional vertical upward water absorption test on concrete specimens and measured the water absorption over time using an electronic balance to obtain the relationship between the cumulative water absorption per unit area of the absorbing surface and the square root of time. As in the case of water immersion distance, the relationship is generally linear, but as the water absorption progresses, the water absorption rate decreases and deviates from the linear relationship. Yury et al. [127], challenges the normal method of water uptake in cementitious materials according to the square root of time. Therefore ,there is need to abandon the $t^{1/2}$ method of calculating

the capillary absorption for cement materials. A better way of defining the capillary absorption is that it is the ration between water uptake in cementitious materials and the fourth root of time. Cementitious materials are hygroscopic and upon interacting with water, they swell. Compared to other building materials, C-S-H contents in cement materials generate a divergence/variance from the $t^{1/2}$ relationship. This is a better explanation compared to bi-dimensional transport or gravity's effect. Tests show that the $t^{0.25}$ method is effective for samples of up to ten days and it has a linear evolution of water uptake. Moreover, the $t^{1/4}$ can be used for cracked and uncracked cementitious materials and improves fitting compared to the $t^{1/2}$ relation. This phenomenon is probably linked to the fact that ordinary concretes, by virtue of their pore structure (morphology, connectivity), particularly favor flow by capillarity.

2.5. Experimental techniques

2.5.1. ^{1}H-NMR relaxometry

2.5.1.1. Introduction

Many atomic nuclei have non-zero spin angular momentum in their lowest energy state and non-zero magnetic momentum,see **Eq.**(**2.2**). This equation represents the phenomenon that gives rise to nuclear magnetism [128] [129].

$$\mu = \gamma \bar{h} I \tag{2.2}$$

where μ is the magnetic moment, γ is the nuclear gyromagnetic ratio, I is the spin angular momentum operator (the quantum number m of I can only take values in intervals of one from -I to I) and $\bar{h}$ is the Planck constant over 2π.

For a (non-ferromagnetic) sample in equilibrium and in the absence of magnetic field, the distribution of magnetic moments is isotropic and consequently, the net magnetisation is zero. However, in the presence of an external field, a splitting of the energy levels occurs due to the Zeeman effect, generating a net magnetisation different from zero. The interaction between the nucleus and a constant magnetic field B_0, (in the z-direction) can be represented by the Zeeman effect . These eigenvalues represent the possible energy values (2I + 1) for the nucleus in the presence of the field. These levels are equally and the difference between two consecutive levels. The photon energy at this frequency is $E = {h\omega}/{2\pi}$, then resonance occurs. The difference in populations between the two levels (for a two-level core, see **Figure 2.3**) is given by the energy difference and the temperature, as

postulated by the Bolztmann distribution [130]:

$$\frac{n_1}{n_2} = exp\left(\frac{\Delta E}{k_B T}\right) \tag{2.3}$$

Where n_1 is the population at the lower energy level, n_2 is the population at the higher energy level, k_B is the Boltzman constant and T is the temperature. Considering a spin of (1/2), in thermal equilibrium there is a population-difference which generates a non-zero total magnetisation. This magnetisation (M_0) is aligned with the external field and has the following magnitude. Where $n = n_1 + n_2$ is the total number of nuclei. From **Eq.(2.4)** it can be seen that the magnetization is directly proportional to the external field and the number of nuclei, and inversely proportional to the temperature.

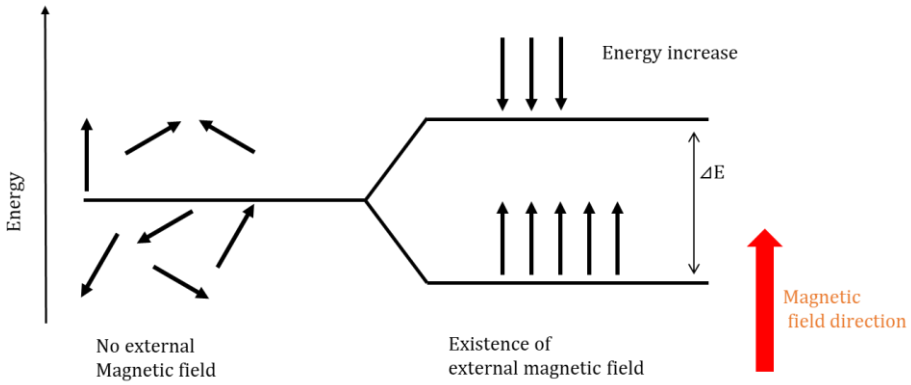

Figure 2.3 Schematic diagram of zeeman energy of a nucleus

2.5.1.2. Classical theory

According classical theory of electromagnetism, a magnetic moment (M) in the presence of an external field (B_0), experiences a torque equal to the rate of change of angular momentum. Then since $\mu = \gamma \bar{h} I$, the motion of the magnetic momentum can be described by the following quation.

$$\frac{d\mu}{dt} = \gamma\mu \times B_0 \tag{2.4}$$

In order to solve the **Eq.(2.4),** it is useful to switch to a rotating co-ordinate system, and it is possible to write the motion of the magnetic moment in the rotating system . As shown in **Eq.(2.4),** only that the field (B_0) is replaced by an effective magnetic field (B_{ef}). From this expression, if a rotating system is chosen with $\omega = \gamma B_0$, the effective field (B_{ef})

is zero. In the co-ordiante system $d\mu/_{dt} = 0$ and therefore, the magnetic moment is a fixed vector. Therefore, with respect to the laboratory the magnetization is precessing with anguar velocity ω_0, where $\omega_0 = \gamma B_0$. This frequency is called the larmor frequency and for a magnetic field value (for example, Hydrogen nucleus 42.6 MHz at 1 Telsa).

Using this principle, it is possible to manipulate spin systems by applying oscillating fields. For example, if a (B_1) magnetic field is applied on the x'-axis of the rotating system at ω_0, the effective field in the system will be $(B_{ef} = B_1\hat{\imath})$, so the magnetization will strat to precess around the x'-axis with a frequency $\omega_1 = \gamma B_1$. The magnetization will continue to precess with frequency ω_0 around z–axis, but will also precess with frequency (ω_1) around the x-axis, where the angle of rotation of the magnetization is $(\gamma B_1 t)$, and it is possible to vary the magnetic field strength, as well as the time on the magnetic field is applied, to achieve the desired angle. In NMR, a pulse that rotates the magnetization by 90° (typically from the z-axis to the xy plane) and a π pulse that reverses the magnetisation by means of a 180° rotation [130][131].

2.5.1.3. Relaxation time

For the moment, the interaction between the sample spins and between the sample and the lattice has not been considered. These interactions are of great importance as they produce variations in the magnetization, giving rise to the so-called relaxation processes. The time evolution if rhe magnetization under such interactions was sfirst studied by Bloch [132]. He proposed a set of phenomenological equations describing the behaviour of the system.

$$\begin{aligned} M_x &= M_0 e^{-t/T_2} \cos\omega_0 t \\ M_y &= M_0 e^{-t/T_2} \sin\omega_0 t \\ M_Z &= M_0 \left(1 - e^{-t/T_1}\right) \end{aligned} \tag{2.5}$$

Where T_1 represents the longitudinal relaxation time and T_2 represents the transverse relaxation time.

As shown in **Eq.(2.5)**, it can be concluded that the decay of the magnetization in the xy-plane is associated with T_2 (transverse relaxation), while the magnetization in the z-axis depends on the T_1 (longitudinal relaxation). The longitudinal relaxation occurs as a result of the energtic exchange between the spin system and the lattice. The lattice is defined as the arrangement of nucleus that the spin system uses as a reservoir of the thermal energy

and is therefore also often referred to as spin-lattice relaxation. The transverse magnetization is not related to the total spin energy unchanged. It is important to clarify theta the external magnetic field inhomogenetities (B_0) accelerate the transverse relaxation since they generate a phase shift between spins proportional to the $\gamma \Delta B_0$, where ΔB_0 represents the field inhomogenity. Thus, the in plane magnetization decays with $T_2{}^*$, where $\frac{1}{T_2{}^*} = \frac{1}{T_2} + \frac{1}{\gamma \Delta B_0}$ for the case of inhomogenous fields generally $T_2{}^* \leq T_2$.

As mentioned above, the magnetization (M_0) is very small but detectable, because it is very well defined frequency. For this reason, the way to make measurements is by means of a coil specifically tuned to the Larmor frequency, in which current will be induced due to the variation of magnetic flux caused by the precession of the magnetisation, thus obtaining an NMR signal [131].

2.5.1.4. Free induction decay

The simplest NMR experiment consists mainly of a constant magnetic field (B_0) in the z-direction and an RF coil in the xy plane to generate the oscillating field (B_1) to rotate the magnetization to the x'-y' plane (90° pulse) and then detect the signal induced by the magnetization rotating in the same or another coil. The signal obtained is called FID (free induction decay), since the magnetization us allowed to evolve freely once it is in the x'-y' plane.

The strength of the signal induced by the precessing magnetization is directly proportional to the amount of water in the sample following the P_{90} pulse, and it decays exponenetially with time, with signal lifetime T_2 . The free induction decay signal is the signal after the P_{90} excitation pulse (FID). The most fundamental NMR experiment is to apply single pulse excitation and observe a FID signal. As can be seen in the FID signal, The rotating magnetisation's precessing nuclei all rotate at the same time at first. However, due to magnetic interactions between nuclei, each nucleus has a slightly different magnetic field than its neighbors. As a result, each nucleus rotates at a slightly different frequency. They lose coherence and de-phase as a result. The signal amplitude decreases as the net magnetisation, which is the vector number of the individual nuclear moments in the sample, decreases. This is where the T_2 relief comes from [133].

2.5.1.5. CPMG

The Carr-purcell-Meiboom (CPMG) method is used in ^{1}H-NMR relaxometry to determine the pore structure [134]. The CPMG method was proposed by Carr et al.[134] and modified by Meiboom et al.[135]. CPMG is an abbreviation for Carr Purcell Meiboom

and Gill. It is mainly used to measure the pore sizes in cement and concrete. The method involves separating two successive radio frequencies by an interval time τ applied as an ensemble to produce a spin-echo at 2τ. The goal is to apply the frequency long enough to tip the protons in a 90-degree manner and then change their phase before applying another pulse to produce an "echo". This phase is applied after τ time. It is done now by another frequency 180-degree in the opposite direction. Successive pulse of 180-degree in opposite directions are done after intervals of 2τ. A common way of doing the CPMG is through a series of alternating 180-degree pulses on the y-axis. These pulses will saturate the magnetization in the longitudinal direction. After each alternating pulse, a time delay is left upon 2τ. The method faces the disadvantage of the 'coherence pathways' created may not be eliminated using log spacing, while linear spacing that eliminates it may average out echoes at long echo times rendering insufficient in such scenarios [130][136].

2.5.1.6. Spin echo method

Another widely used experiments is the spin echo or Hahn echo, named after the man who was the first to implement it. It consists of applying a $\pi/2$ pulse, generating an FID, and a later time applying a π pulse, inverting the magnetisation in such a way as to refocus the previously dephased spins, forming an echo at a later instant. It should be noted that the π pulse manages to refocus the dephasing produced due to the field inhomogeneities, which provides this sequence with an important robustness against inhomogeneity effects. However, the spin echo does not reach the same maximum value as the FID, but decreases exponentially due to decay by T_2. Therefore, performing Hahn echo measurements for different τ is a way to determine the spin-spin relaxation time or T_2. Thus, by measuring the fast and more slowly T_2 in cement, a ratio can be quantitatively worked upon [29][118][137] [138].

2.5.2. Water uptake for cement based materials

2.5.2.1. Introduction

Cementitious materials such as concrete and mortar are porous materials with pores of various sizes ranging from several nm to mm. we present a one-dimensional water absorption model using capillary tension as a driving force and various measurement methods.

Capillary tension is an example of a driving force that contributes to the infiltration of liquid water into a hardened cement body that is a porous body having fine voids. Washburn [139] expresses the capillary tension in a simple tube with the cross section by

Eq.(**2.6**)**.**

$$P = \frac{2\,\gamma\cos\theta}{r} \tag{2.6}$$

Where, P: Capillary tension (N/m^2), γ: Surface tension of liquid (N/m), θ: Contact angle (°) and r: Capillary radius (m)

When a viscous liquid flow through a circular pipe with a constant pipe diameter at a stable and constant speed, the average flow velocity in the pipe is expressed by using **Eq.(2.7)** called the Hagen-Poiseuille formula.

$$Q = \frac{\pi\,P\,r^4}{8\,\eta\,L} \tag{2.7}$$

Where, Q is the average flow velocity in the pipe (m^3 / s), η is the viscosity coefficient of the liquid (Pa. s), and L is the liquid water infiltration distance (m).

Based **Eq.(2.6)** and **Eq.**(**2.7**)**,** the liquid water infiltration distance L driven by the capillary tension in the circular tube is expressed by **Eq. (2.8)**

$$L = \sqrt{\frac{\gamma\,r\,\cos\theta}{2\eta}\,t} \tag{2.8}$$

Where, t represents time (s).

From the above, the liquid water infiltration distance L is proportional to the square root of time t (hereinafter referred to as the √t rule). **Eq.** (**2.8**) is called the Lucas-Washburn equation, and has been applied for the water absorption into concrete. The void structure in the hardened cement body is different from that of the circular tube, but if the void structure is regarded as some simple shape, the circular tube is suitable. In addition, it has been reported that the behavior of liquid water movement deviates from the Lucas-Washburn equation when the water absorption time exceeds several hundred hours.

The influence of gravity on the driving force of liquid water intrusion is also considered. The upper threshold of the effective flow path diameter in which the capillary tension is dominant is called the capillary length κ (mm) and is expressed by the **Eq.** (**2.9**).

$$\kappa = \sqrt{\frac{\gamma}{\rho\,g}} \tag{2.9}$$

2.5.3. Water uptake tehniquess

2.5.3.1. Gravimetric method

The experimental procedure requires a sample preconditioning which includes frying and insulation of lateral faces. Then the samples smooth bottom (just a few millimeters) is brought in touch with water to prevent immersion. The weight of the sample increases due to the water absorption, expressed by unit area which contrasts with the period from beginning of the interaction.

$$i = St^{1/2} + C \tag{2.10}$$

where *i* is the accumulated volume of water absorbed per unit area, *t* is the time and C is the constant.

2.5.3.2. X-ray tomography

The modern micro-tomographic X-ray computed (X-μCT) application, as implemented in this work, reflects the high-resolution advancement in the methodology of computed X-ray (XCT) tomography originally established in the latter 1960s and early 1970s for medical purposes (CT scan or CAT, computed axial tomography), to remove traditional 2D X-ray limitations. Godfrey N. Hounsfield (1919-2004) was usually responsible for the discovery of medicinal CT Hounsfield [140]. He took a novel concept of obtaining a wide range of radiographs from various angular locations along the rotation axis of an item (a body or a portion of it), accompanied by applying a mathematical reconstruction algorithm in order to measure the X-ray attenuation coefficient (μ) map for any volume in the body. This allows for better visualization of density and structure differences of bones and internal organs relative to the conventional x-ray radiography. applying a mathematical reconstruction algorithm in order to measure the X-ray attenuation coefficient (μ) map for any volume in the body. This allows for better visualization of density and structure differences of bones and internal organs relative to the conventional x-ray radiography. In 1917, Austrian mathematician Johann Radon had already solved the problem of extracting a part of an object from an endless number of rays traveling through it . The study showed that there is an inverse radon transform, which can be used to map (μ) differences within a piece of the object until there are a number of radiographic projections. However, for the advancement of medical CT, the work of Allan M. Cormack who proposed certain mathematical concepts for tomographic reconstruction several years later in 1963 was equally fundamental. Their invention was given the Nobel Prize in 1979 in Physiology or Medicine by Hounsfield and Cormack. Soon after its first introduction in the medical sector, computed tomography was used to examine non-living systems in manufacturing, where all the problems associated with the limitations of the radiation exposure became almost irrelevant in operation.

X-rays are short-wave electromagnetic radiation. It penetrates matter to a limited

extent. Just like conventional radiography, X-ray tomography is based on the irradiation of the measurement object and the measurement of the radiation weakened by the measurement object. In conventional radiography (X-ray irradiation), a projection of the measurement object is generated. The three-dimensional measurement object is mapped two-dimensionally. Objects that lie one behind the other in the beam path are superimposed in the measured projection.

The working principle of an X-ray tomography is similar to that of the medical method, however, regarding its use in cement and concrete materials, the spot size of the source of the X-ray is much smaller (approximately 10 μm) that allow placement of the object close to the source of the X-ray [141]. The tomography X-ray absorption is a non-destructive technique that allows the image reconstruction "sectional" an object in three dimensions. Its principle is based on the multidirectional analysis of the interaction of the matter with an X-ray beam, by recording with detectors. radiation transmitted after passing through an object.

The basic elements that make up an X-ray tomography equipment are a source and a detector. The geometry of the X-rays and the detector varies depending on the equipment. For the study of cement and concrete, collimated rays that cover the entire width of the object and a series of in-line detectors are typically used. The object to be scanned is located between the source and the detector and an X-ray discharge is sent from the source towards the object, measuring the intensity of the radiation reaching the detector. The density of the object determines the intensity of the X-rays reaching the detector [142]. The higher the density of the object, the lower the intensity of radiation detected since the X-rays are absorbed by the object or reflected back to the source.

2.5.3.3. Radiography

Neutron and X-ray radiography is a non-destructive visualization technology that utilizes the attenuation characteristics caused by the interaction (capture, scattering, and nuclear reaction) between nuclei and neutrons when neutrons pass through a substance [143]. An example of using the same principle is X-ray, and this method can be said to be a neutron version of X-ray. Neutrons are attenuated by factors such as the sample's density and thickness and the mass absorption coefficient. However, since neutrons have a strong absorption/scattering effect, especially on hydrogen, neutrons correspond to the presence of water [144]. In the actual measurement, the test piece is first irradiated with thermal neutrons generated by the nuclear reactor's nuclear reaction. The neutrons that pass through the test piece are converted into light by the fluorescence converter and reflected by the two mirrors to create a transmitted image.

The neutron beam is attenuated when the sample is irradiated. Still, its attenuation characteristics differ depending on the sample elements and are not related to the molecular weight [145]. Hydrogen, lithium, boron, cadmium, and samarium have low permeability. Conversely, silicon transmittances, calcium, oxygen, aluminum, and iron are the main components of cement-based materials. It is about two orders of magnitude smaller than the element [146]. Therefore, when irradiating concrete, it is possible to easily transmit heavy metals such as iron, lead, and zirconium, which are difficult for X-rays and γ-rays to pass through, and a transmission image according to the presence of hydrogen atoms can be obtained. Furthermore, it is possible to capture high molecular materials containing a large amount of hydrogen.

2.5.3.4. Linear attenuation coefficient of water

Radiography is one of the visualization methods that acquires a contrasted image when the radiation passes through an object due to the difference in the amount of transmission. The attenuation behavior of the X-rays can be described based on Beer-Lambert law and the transmitted X-ray energy of the dry and wet sample can be written as shown in

$$I = I_0 \, e^{-\mu \, d} \tag{2.11}$$

The main radiation used in radiography are neutrons and X-rays, but the nature of interactions with elements is different. Therefore, μ changes depending on the radiation quality of the irradiation and the elements that make up the irradiation object Roles and Carmeliet [147].

Where : μ is the attenuation coefficient (cm^{-1}), d is the thickness of the materials (cm), I_o is the incident intensity, and I is the x-ray attenuated results in the transmitted intensity.

Roles and Carmeliet [147] and Lukovic et al., [148], investigated and explained as (see in Fig.3 and Fig.2 from ref [147][148]) with a known thickness can be determined form the change intensity level as shown in **Eq.(2.12)** (or) the detector visualize the intensity levels as Grey scale values (G_{sv}) and it can be determined from the change in (G_{sv_0}) by logarithmically subtracting from the wet sample to dry sample .

$$G_{sv} = G_{sv_0} \, e^{-\mu \, d} \tag{2.12}$$

$$G_{sv_{dry}} = G_{sv_{air}} e^{-\mu_{mor} d_{mor}} \quad (2.13)$$

Where:- $G_{sv_{dry}}$ = Grey value of dry sample after passing the mortar , $G_{sv_{air}}$ = Grey value of air after passing through air, μ_{mor} = Attenuation coefficient of mortar (cm^{-1}) and d_{mor} = Thickness of mortar (cm) .

$$G_{sv_{wet}} = G_{sv_{air}} e^{-\mu_{wet} d_{wet}} \quad (2.14)$$

Once the attenuation coefficient of water is determined, G_{SV} of the wet porous material can be correlated to G_{SV} of the dry porous material according to the following **Eq.** Error! Reference source not found..

$$G_{sv_{wet}} = (G_{sv_{dry}} e^{-\mu_{mor} d_{mor}}) e^{-\mu_w d_w} \quad (2.15)$$

It can be determined from the change in G_{SV} by logarithmically subtracting from the wet sample to dry sample.

Where: - μ_w = Attenuation coefficient of water (cm^{-1}), d_w = thickness of water (cm), Water thickness can be expressed as shown in the below **Eq.**Error! Reference source not f ound.**.**

$$d_w = \Delta C_w \frac{d}{\rho_w} \quad (2.16)$$

From **Eq.**Error! Reference source not found.**, Eq.** (**2.14**) , and **Eq.** (**2.16**)**,** the he amount water absorbed can be calculated by the following equations.

$$\Delta C_w = -\frac{\rho_w}{\mu_w d} ln \frac{G_{sv_{wet}}}{G_{sv_{dry}}} \quad (2.17)$$

$$\Delta C_w * \mu_w = -\frac{\rho_w}{d} \ln \frac{G_{sv_{wet}}}{G_{sv_{dry}}} \quad (2.18)$$

Where: - ρ_w= Density of water (g/cm^3), d = thickness of water (cm) and μ_w = Attenuation coefficient of water (cm^{-1})

In the calculation of water absorption by X-ray CR, in **Eq.** (**2.18**), was set to ρ_w 1.00 g/cm3, and μ_w was used by fitting values so that the change in mass and the change in luminance value were close. Two of them gave approximately linear results, and μ_w was . As can be seen in this study, it is possible to calculate the moisture distribution from the relationship between the mass value and the luminance value at two points in the range where the linearity of the luminance value and the mass change due to moisture can be confirmed. On the other hand, in X-ray CR, we obtained the result that the luminance value and the mass change of the image roughly corresponded by using a constant μ_w. This shows that the water absorption can be calculated from the X-ray CR image.

3. ^{1}H-NMR relaxometry

3.1. Experimental methods

3.1.1. Materials

White Portland cement provided by Taiheiyo Cement Corporation was used to prepare the hcp. As ^{1}H-NMR relaxometry is affected by paramagnetic ions such as iron and magnesium, white Portland cement containing only trace amounts of iron or magnesium was used in this study. The chemical composition was determined by the X-ray fluorescence (XRF) method and the mineral composition of the white Portland cement were performed by X-ray diffraction (XRD) on a powder sample. D8 advance equipment was used for the X-ray powder diffraction (XRD) and the TOPAS software was used for the Rietveld analysis, as shown in **Table 3.1** and **Table 3.2**,respectively. It should be noted that there is a small proportion or a non-detectable quantity of magnetic oxides (Fe_2O_3 and Mn_2O_3) contributing to the transverse NMR relaxation [106].

Table 3.1 Chemical composition as determined by XRF analysis (mass %)

SiO_2	Al_2O_3	Fe_2O_3	CaO	MgO	SO_3	Na_2O	K_2O	LOI	Sum
22.68	4.50	0.19	65.07	1.19	2.75	0.06	0.07	3.18	99.69

Table 3.2 Mineral composition as determined by XRD/Rietveld analysis (mass %).

Alite	Belite	Aluminate phase	Periclase	Basanite	Gypsum	Calcite	Sum
48.96±2.33	33.98±0.38	4.46±0.24	0.51±0.41	1.01±0.43	3.30±0.80	5.26±0.38	97.48

All the materials were stored in a thermostatic room and the temperature was controlled at 20 ± 1 °C for one day prior to mixing. The mixing was performed at room temperature. The water-to-cement ratios of the specimens were set as 0.40 and 0.55 (hereinafter denoted as W40 and W55). The paste was mixed using a planetary centrifugal mixer at 1000 rpm for 1.5 min after the water was added to the cement. Next, the paste was scraped to detach residual powder from the internal surface of the mixer, and finally an additional 1.5 min of mixing was performed. After the mixing, the paste was immediately moved to the thermostatic room at 20 ± 1 °C and remixed every 30 min for 8 h to minimize segregation. All samples were sealed and cured after being poured into the cylindrical

plastic container (φ30 mm × 125 mm). After ninety-one days, the plastic container was demolded, and specimens cored to a size of φ4.5 mm × 5 mm and kept at room tempertures.

3.1.2. Method for water absorption

The ^{1}H-NMR relaxometry was performed for the obtained samples in the sealed condition, after vacuum drying, and in the water absorption process. During each measurement, the mass of the sample was measured using a precision balance. Vacuum drying with a degasser (FLOVAC, Quantachrome) was used for the drying treatment. In the vacuum drying, the specimen was kept at 105 °C for one day and then ^{1}H-NMR relaxometry was performed. During the water absorption process, the tap water was used, and its temperature was maintained at 20 °C, 40 °C, and 60 °C. The temperature inside the device was controlled so that the temperature at the time of the ^{1}H-NMR relaxometry measurement was equal to the temperature of the absorbed water. Curing water was used for the water absorption process and vacuum absorption was performed for 30 min after the drying treatment. For the subsequent water absorption, curing water was stored at each temperature and, after that, the samples were stored as shown in **Figure 3.1** and removed from the submerged water immediately before the ^{1}H-NMR measurement. Immediately before the measurement, the water on the sample was wiped off and the Carr–Purcell–Meiboom–Gill (CPMG) measurement was performed. The CPMG echo signal was measured after 30 min, 1 day, 2 days, 5 days, 12 days, and 26 days at different temperatures. Three samples were used for each temperature.

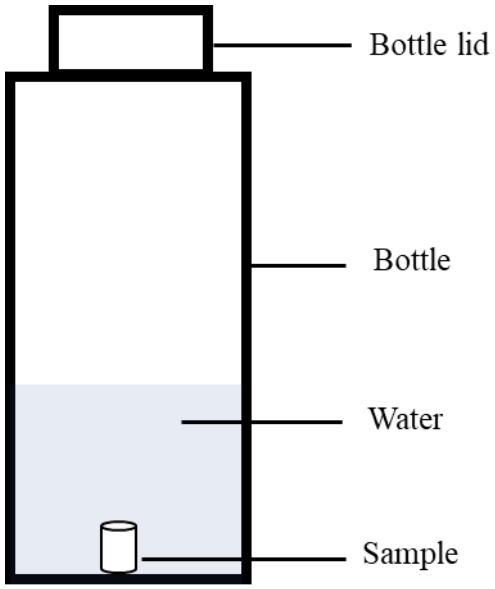

Figure 3.1 Experimental setup for the water absorption at different temperatures

3.1.3. ^{1}H-NMR relaxometry method

The ^{1}H-NMR relaxometry was carried out at Nagoya University in Japan and was conducted using a Bruker minispec equipped as shown in **Figure 3.2**, with a digital filter and a φ10 mm probe. After coring, the cement paste specimen size of φ 4.5 mm × 5 mm was kept in a glass rod has a diameter of φ7 mm and enclosed with a plastic rod with a diameter of φ6 mm, sealed with parafilm and closed with a plastic cap as shown in **Figure 3.3**. The magnet provided a resonance frequency of 20 MHz (0.47 T) for the protons. The $\pi/2$ pulse wavelength was 2.4 μs, which was calibrated on a solid cement sample. The relaxation delay was 1 s [29].

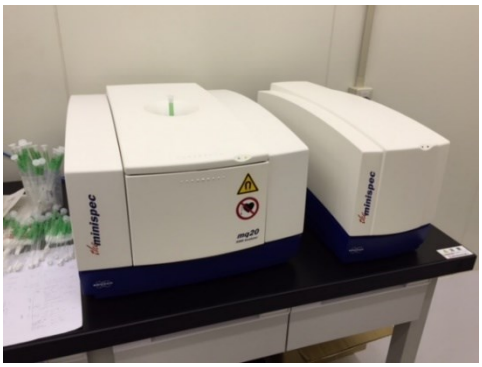

Figure 3.2 ^{1}H- NMR relaxometry device setup

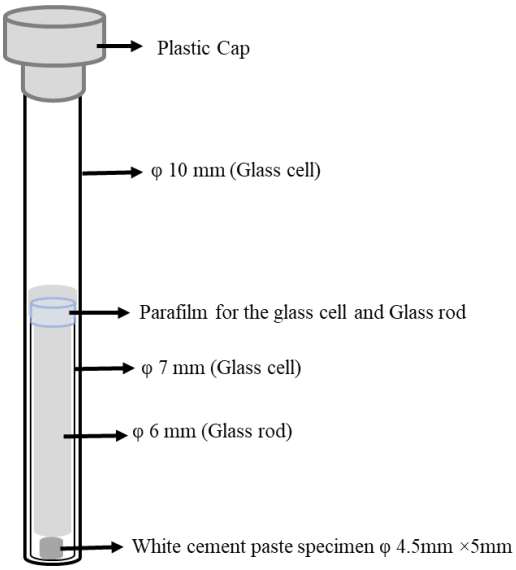

Figure 3.3 Schematic representation for the measurement of white cement paste specimen inside the ^{1}H-NMR relaxometry equipment

The CPMG pulse sequence method proposed by [134] and modified by [149] was used for all the measurements to obtain the distribution of T_2 relaxation time based on the CPMG echo sequence decay. The device was connected to the water bath where the temperature was maintained throughout the experiment. Blank cell correction at each temperature was performed. Two-hundred log-spaced echoes were recorded from 0.1 to 2180 ms and more than 256 averages were recorded to obtain a sufficient signal-to-noise ratio. To record the CPMG pulse sequence and solid echo signal took approximately 1 h and 45 min. The decay curve was obtained by measuring the time required to return to the thermal equilibrium state when the external magnetic field was removed from the excited state (transverse relaxation time: T_2). This relaxation time becomes shorter as the constraint becomes stronger. In other words, for water present in the voids, the longer the relaxation time, the larger the void diameter. The measured CPMG data were analyzed with an in-house inverse Laplace transform (ILT) algorithm, using the Butler–Reeds–Dawson (BRD) method [150], to obtain the quasi-continuous T_2 distributions. As shown in **Figure 3.4**, the four confirmed T_2 peaks from the ILT algorithm were used to analyze the CPMG data. The four peaks and the ratio of each peak to the total intensity were used to evaluate the quantities of interlayer water, gel pore water, interhydrate pore water, and capillary pore water [100], [151]. A lower T_2 indicates smaller pores.

NMR signals are expected to change with temperature, owing to the temperature dependence of the Boltzmann factor that contributes to the equilibrium nuclear magnetization. Based on the theory [152], [153], the 60 °C/20 °C and 40 °C/20 °C signal ratios were 0.880 and 0.936, respectively, while the obtained CPMG data was normalized by the data at the 20 °C condition. It is also assumed that the T_2 values at different temperatures are not affected by the temperature of the sample [153].

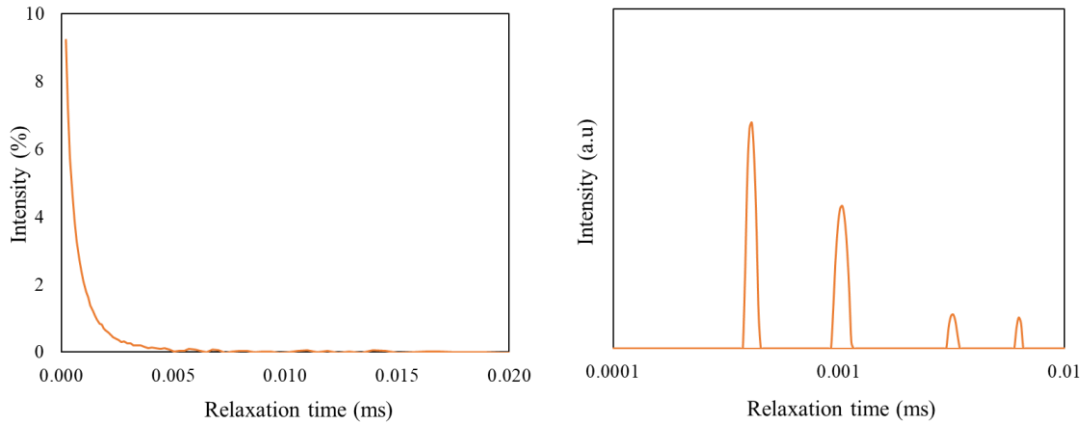

Figure 3.4 ^{1}H-NMR relaxometry CPMG decay curve of W55 cement paste at the sealed

condition and T_2 relaxation time obtained by calculating the decay curve from an inverse Laplace transformation

3.2. Theory

3.2.1. Rate of water exchange between large and fine pores

The water in the cement paste can be separated into two categories, the water in either fine or large pores, according to the equation:

$$W_L + W_F = W \tag{3.1}$$

where W_L is the water in large pores (capillary pores + interhydrate pores) (g/g-ignited cem), W_F is the water in fine pores (gel pores and interlayer spaces) (g/g-ignited cem), and W is the evaporable water (g/g-ignited cem).

The water redistribution from the large pores to the fines pores during the sorption test can be expressed as:

$$\frac{\partial W_F}{\partial t} = \alpha W_L \tag{3.2}$$

where t is the time (days) and α is a coefficient indicating the rate of water redistribution from large pores to fine pores per unit time (1/day).

3.2.2. Activation energy of the rate of exchange between large and fine pores

In 1889, Arrhenius introduced the concept of activation energy as the minimum energy necessary for a specific chemical reaction to occur. Since then, it has been adapted to many phenomena that are time and temperature dependent. Thus, many phenomena related to the field of cementitious materials were found to be well described by the activation/rate theory. For instance, hydration [154], permeability [155], moisture diffusion [156], [157], diffusion of ions [158]–[160], creep [161]–[163], and even aging of cracked concrete [164] have already been analyzed through this approach. In this study, the activation energy related to the rate of exchange between large and fine pores during the water uptake process will be calculated. An Arrhenius plot in which the logarithm of the rate is plotted against the reciprocal of the absolute temperature will provide this activation

energy (E_a) divided by the ideal gas constant (R = 8.314 J.K^{-1}.mol^{-1}) as the slope of the curve.

3.3. Results and discussion

3.3.1. ^{1}H-NMR results

The obtained T_2 relaxation times for both compositions are presented in **Figure 3.5**. The peaks corresponding to the capillary pore water are difficult to observe in some cases. For a very thin section, the exposure to the atmospheric conditions just before the beginning of the test (on the order of several minutes) can be enough to dry out the capillary pores instantly. Therefore, the capillary pores detected by this approach are expected to be very low [23]. The fast diffusion relaxation model links the relaxation time T_2 to the pore surface area S and pore volume V as:

$$\frac{1}{T_2} \sim \frac{\varepsilon S}{V} \cdot \frac{1}{T_{2,surf}} \tag{3.3}$$

where ε is the diameter of a water molecule, taken as equal to 0.28 nm, and $T_{2,\,surf}$ corresponds to the fast-relaxing molecules on the pore surface. Following the method proposed by Gajewicz [131], this surface relaxation time is 106 μs. By considering planar pores with area A, the pore surface can be expressed as $S = 2A$ and the pore volume can be expressed as $V = Ad$, where d represents the pore width [151]. Thus, **Eq. (3.3)** becomes:

$$\frac{1}{T_2} \sim \frac{2\varepsilon}{d} \cdot \frac{1}{T_{2,surf}} \tag{3.4}$$

The pore width is clearly proportional to the relaxation time T_2 and can provide initial details on the C-S-H microstructure. In the sealed condition, the size of the interlayer space is approximately 1.73±0.08 nm for W40 and approximately 2.07±0.11 nm for W55. Under 105 °C drying, most of the water is removed and the remaining fraction in the interlayer space shows a stacked C-S-H structure with an interlayer width equal to 1.24±0.20 nm and 1.20±0.20 nm for W40 and W55, respectively. After wetting, the interlayer spaces of W40 and W55 broaden again, returning after 26 days to their initial sizes of 1.72±0.11 nm and 2.02±0.11 nm, respectively, at 20 °C, and to a greater sizes of 1.87±0.05 nm and 2.34±0.33 nm, respectively, at 40 °C and to 2.00±0.19 nm and 2.30±0.00 nm, respectively, at 60 °C. The absorption under high temperatures clearly widens the interlayer pores. The same observations can be made for the gel pores with average initial widths of 4.42±0.72 nm and 5.16±0.30 nm for respectively W40 and W55 in the sealed

condition. The gel pores become larger after wetting, especially for higher temperatures. After 26 days of water absorption for W40 and W55, the calculated widths are equal to 5.21±0.47 nm and 5.71±0.17 nm, respectively, at 20 °C; to 5.54±0.19 nm and 6.71±0.10 nm, respectively, at 40 °C; and to 5.49±0.39 nm (7.31±0.00 nm) at 60 °C. For interhydrate and capillary pores, more fluctuation is observed with temperature, which can be explained by the high signal-to-noise ratio and the lower number of detected pores as compared to the finest ones (statistically, a lower representative population).

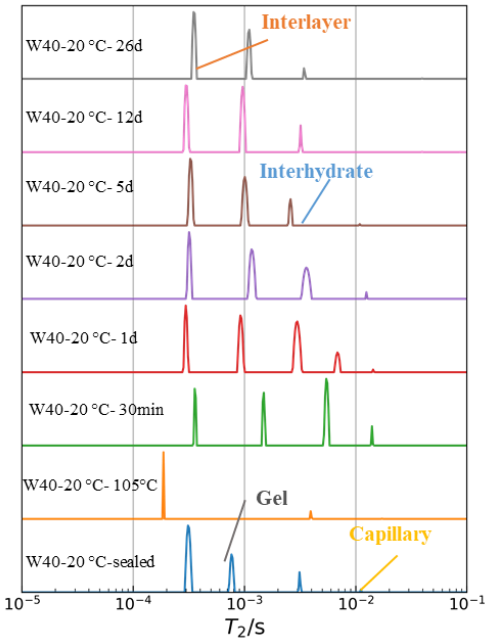

(a) W40 - 20 °C

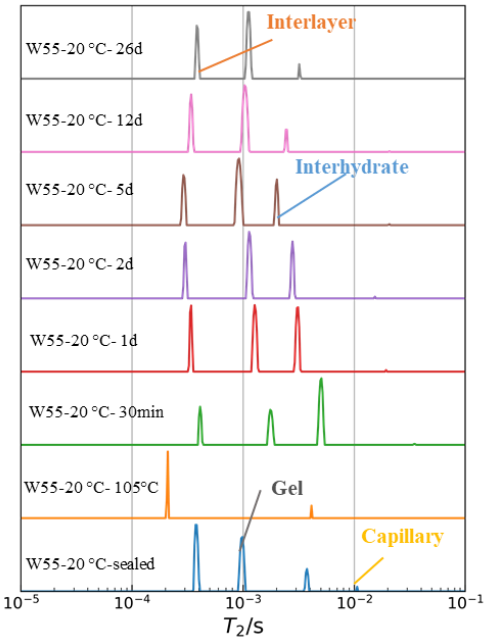

(b) W55 – 20 °C

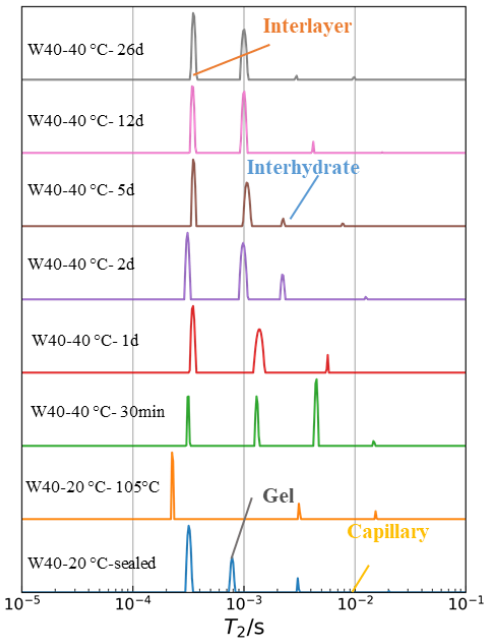

(c) W40 – 40 °C

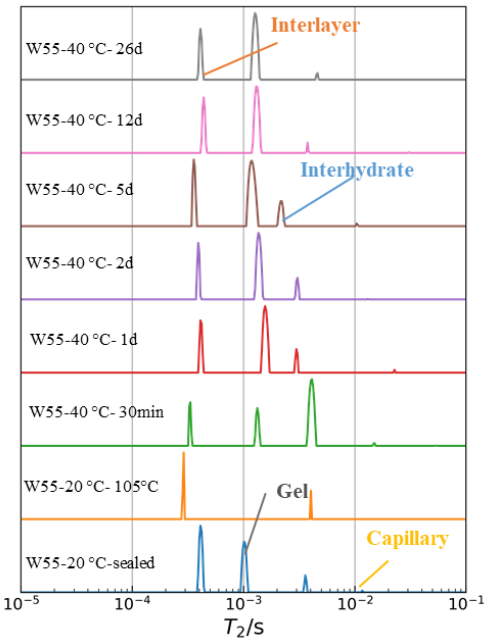

(d) W55 – 40 °C

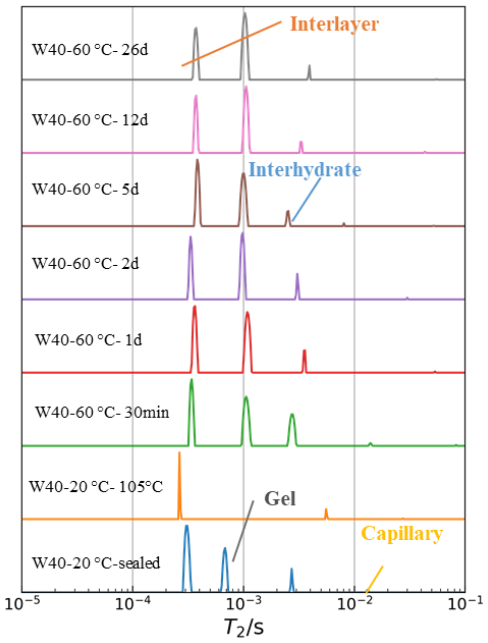

(e) W40 – 60 °C

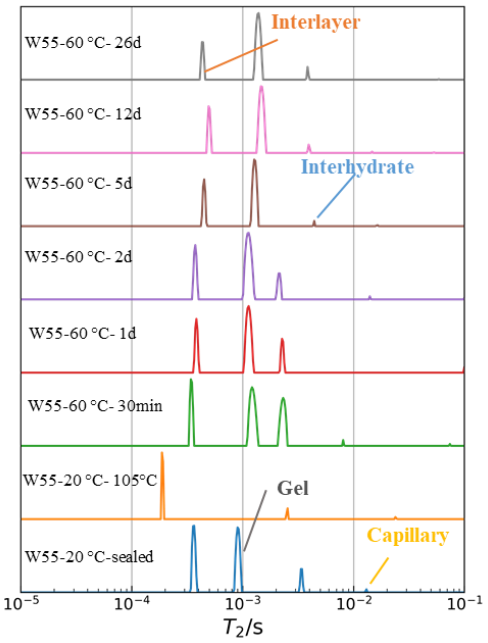

(f) W55 – 60 °C

Figure 3.5 T_2 distributions calculated by an inverse Laplace transformation of the CPMG signal of W40 and W55 under temperatures of 20 °C, 40 °C, and 60 °C

The evaporable water for different samples was measured with a balance in different conditions. The mass evolutions are presented in **Figure 3.6**Error! Reference source not found.. The mass given by the balance and that obtained by the NMR being generally in the same range confirms that all the water is captured by the ^{1}H-NMR. A high

evaporable water content was observable for W55 as compared to W40, which is consistent with the initial high-water content and consequently the high porosity. For the sealed condition, the water content was slightly higher as compared to the wetted samples for the different periods of sorption. After drying at 105 °C, the evaporable water was almost removed and only a very small quantity remained in the interlayer pores according to the ^{1}H-NMR results. The sample was assumed to be completely dried and its mass used as a reference to estimate the absorbed water from the balance measurements. The influence of temperature on the sorption is not detectable here since a high percentage of the water was already absorbed after the first 30 min.

The water distribution according to the size of pores given by ^{1}H-NMR is also presented in **Figure 3.6.** In the sealed condition, a large amount of the evaporable water is present in the interlayer pores. After drying and rewetting, this initial amount of interlayer water was never again recovered for the various cases. For the temperatures of 20 °C and 40 °C, the water starts to move to the cement paste via the interhydrate pores before migrating towards the finest pores (interlayer and gel). Under these environmental conditions, the interlayer pores seem to increase slightly with time, which is not the case under 60 °C. Additionally, for this temperature, the interhydrate water seems already lower as compared to the gel water after 30 min of water uptake. One explanation for this difference is the increase of the rate of water exchange with temperature, which prevents the initial water state of the sample being attained. At the end of the test (26 days), the interhydrate water becomes negligible and almost all the evaporable water is in the interlayer and gel pores. At this moment, the predominant pores are gel pores except for W40 under 20 °C and 40 °C for which the water is equally distributed between interlayer and gel pores. The influence of the mixture also appears to be important for the microstructure rearrangement. Indeed, W55 with the highest initial water content and then the highest porosity is better able to contain water in the gel pores not only under the sealed condition but also after rewetting. This result suggests that the porosity of W55 is larger than that of W40 and this order is not affected by the microstructural dynamics. This result can also be obtained via the bulk density of C-S-H, which incorporates the gel pore water. Thus, the bulk density of C-S-H decreases with wetting time. It is also a decreasing function of the water-to-cement ratio, which is consistent with previous data [151]. The bulk density appears to decrease with temperature, as the water incorporated in gel pores increases with temperature as compared to interlayer water for both mixtures, but this variation is more pronounced for W55 than W40. Muller et al., (2013b), studied the sealed curing hardened cement samples after 10 days of hydration with different water to cement ratio (W/C= 0.32, 0.40 and 0.48) and they do not show the capillary pore water. Only at very early age, the

capillary pore water can be seen. Based on these backgrounds, sample measurement results of the starting and after 26-day of water suction were consistent to the previous data.

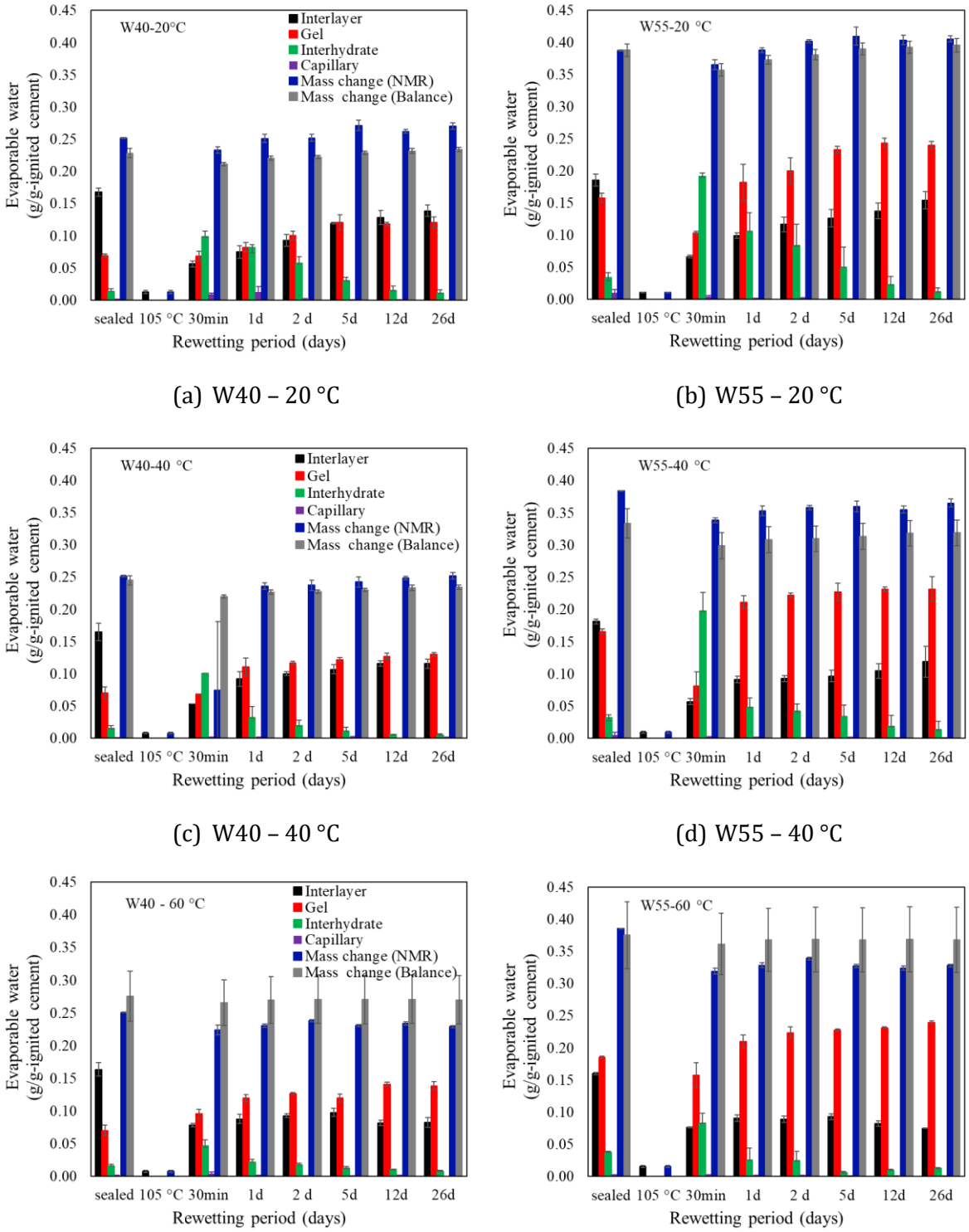

(a) W40 – 20 °C (b) W55 – 20 °C

(c) W40 – 40 °C (d) W55 – 40 °C

(e) W40 – 60 °C (f) W55 – 60 °C

Figure 3.6 The evolution of water components calculated based on the CPMG echo signal of W40

and W55 under 20 °C, 40 °C, and 60 °C, and the evaporable water content of W40 and W55 calculated based on the mass change under 20 °C, 40 °C, and 60 °C.

The reasoning can be simplified by classifying the pores into two different categories: fine and large (free water) pores. The fine pores are defined as the summation of the interlayer and gel pores while the large pores are the summation of the interhydrate and capillary pores. The evolution of the water inside the cement paste can now be plotted according to this classification, as shown in **Figure 3.7.** In the sealed condition, the predominant pores were the fine pores and negligible quantities of water were found in the large pores for both mixtures. After drying at 105 °C, the large pores were completely emptied while a small quantity of water remained in the fine pores. At the beginning of the wetting phase, the large pores had a maximum evaporable water content, with the quantity decreasing with time until reaching the smallest value at 26 days. This water is completely transferred to the fine pores, explaining the increasing function of fine pores with wetting time. The water transfer from the large pores to the fine pores seems to be faster with an increase in temperature. However, this increase does not allow the capture of the initial water in the large pores, especially for W40. At 60 °C, after one day of measurements, the transfer seems almost complete, while this necessary period is longer for lower temperatures.

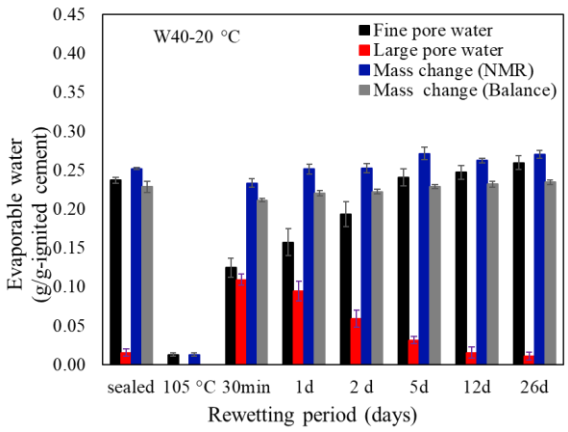

(a) W40 – 20 °C

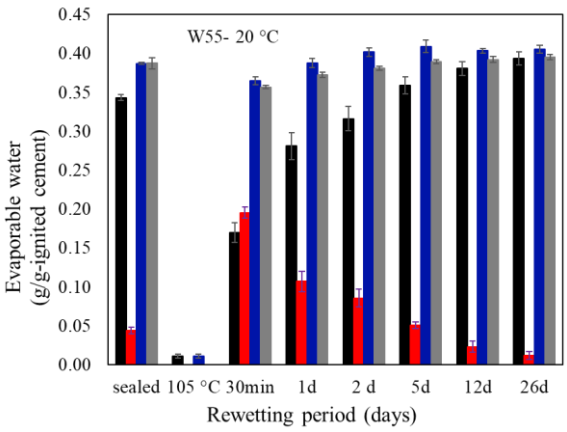

(b) W55 – 20 °C

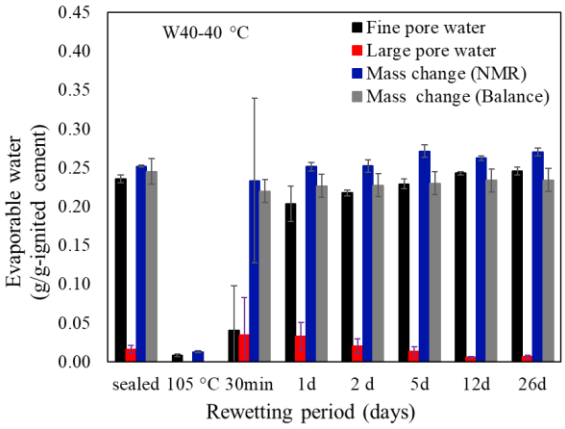

(c) W40 – 40 °C

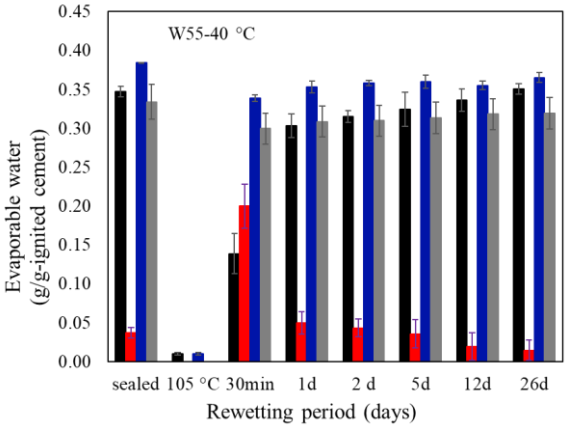

(d) W55 – 40 °C

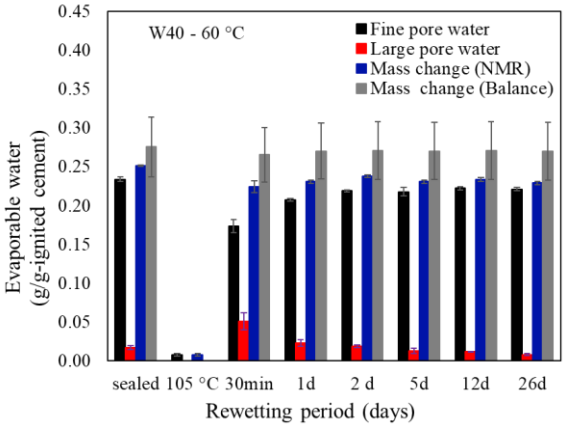

(e) W40 – 60 °C

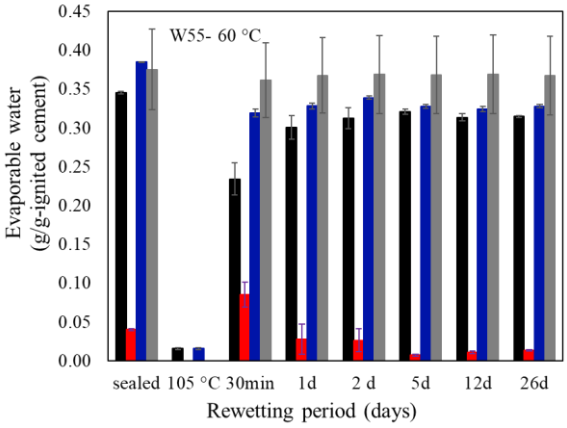

(f) W55 – 60 °C

Figure 3.7 The combined water components calculated based on the CPMG echo signal of W40 and W55 under 20 °C, 40 °C, and 60 °C and the evaporable water content of W40 and W55 calculated based on the mass change under 20 °C, 40 °C, and 60 °C

The coefficient of water transfer from large to fine pores can be calculated using **Eq.(3.5)**. This rate is dependent on the water distribution in the pores as shown in Error! Reference source not found.This dependency on the ratio W_l/W_F can be approximated by a linear function as presented by **Figure 3.8**. The phenomenological concept of this equation is that the pores or surfaces where the water redistribution occurs, and the large pores and the fine pores are connected, and it would be a function of the ratio of volume of the large and fine pores. Therefore, as a first order approximation **Eq.(3.5)**, is applied. A constant coefficient (the gradient) independent from the water distribution in pores of cement paste can be extracted from the linear fitting. this coefficient was named as β.

$$\alpha = \beta\ (W_L/W_F) \tag{3.5}$$

The coefficient β obtained for different temperatures and for both mixtures is presented as the slopes of lines in **Figure 3.8**. For 20 °C, β of W40 – 20 °C is smaller than that of W55 – 20 °C. This is likely due to the difference of the ratio of gel pores to fine pores, as shown in **Figure 3.6**. However, at 60 °C, the trend reverses. Furthermore, the values show a clear temperature dependency similar to water transport coefficients in concrete such as the diffusion coefficient and the permeability coefficient.

The change in diffusion with temperature can be expressed as Error! Reference source not found., where the temperature dependency is explicitly shown [166]. The permeability can be expressed theoretically as function of water density ρ, the gravitational constant g, the specific surface area of the particles σ, the coefficient of viscosity η, and the porosity ε, as shown in **Eq.** (**3.7**) [155].

$$D = cste \left(\frac{T}{T_0}\right)^{\frac{3}{2}} \tag{3.6}$$

$$k = \frac{2\rho g}{\sigma^2 \eta} \frac{\varepsilon}{1-\varepsilon} \tag{3.7}$$

This equation allows us to express the ratio of the permeability for two different temperatures as:

$$\frac{k_T}{k_{T_0}} = \frac{\rho_T}{\rho_{T_0}} \frac{\eta_{T_0}}{\eta_T} \left(\frac{\sigma_{T_0}}{\sigma_T}\right)^2 \frac{\varepsilon_T (1-\varepsilon_{T_0})}{\varepsilon_{T_0}(1-\varepsilon_T)} \tag{3.8}$$

According to **Eq.** (**3.8**), the influence of temperature on permeability can be separated into two parts. The first part concerns the density and viscosity of water. The second part is related to the nature of the material through the specific surface and porosity, which can vary with different mechanisms, such as the dilatation of the porous structure with temperature [167] or the dynamic microstructure observed here. If the impact of the variation of the water properties according to temperature is considered, then permeability should at least double between 20 °C and 60 °C, as shown in **Table 3.3.** If it is assumed that the rate of water transfer is also influenced by the same parameters, then its value at 60 °C should also be greater than twice its value at 20 °C, which is the case for both compositions as presented in **Table 3.3.** The further increase beyond this estimated factor of two can then be related to the microstructural modification of the cement paste due to the temperature

increase. This difference is higher in the case of W40 for which the microstructure is finer and should be more impacted by the water movement, especially when this motion accelerates with temperature. In addition, for the very narrow pores of cementitious materials, the Knudsen effect can take place with more frequent collisions of water molecules with the solid matrix as compared with their collisions with each other (Gawin *et al.*, 1999).

Table 3.3 Water properties calculated from 20 °C to 40 °C and then to 60 °C.

T	ρ (kg/m³)	η (mPa.s)	$\rho_T/\rho_{20\,°C}$	$\eta_{20\,°C}/\eta_T$	$(\rho_T/\rho_{20\,°C})(\eta_{20\,°C}/\eta_T)$
20 °C	998.2	1.002	1	1	1
40 °C	992.2	0.6531	0.994	1.534	1.53
60 °C	983.2	0.4658	0.985	2.151	2.12

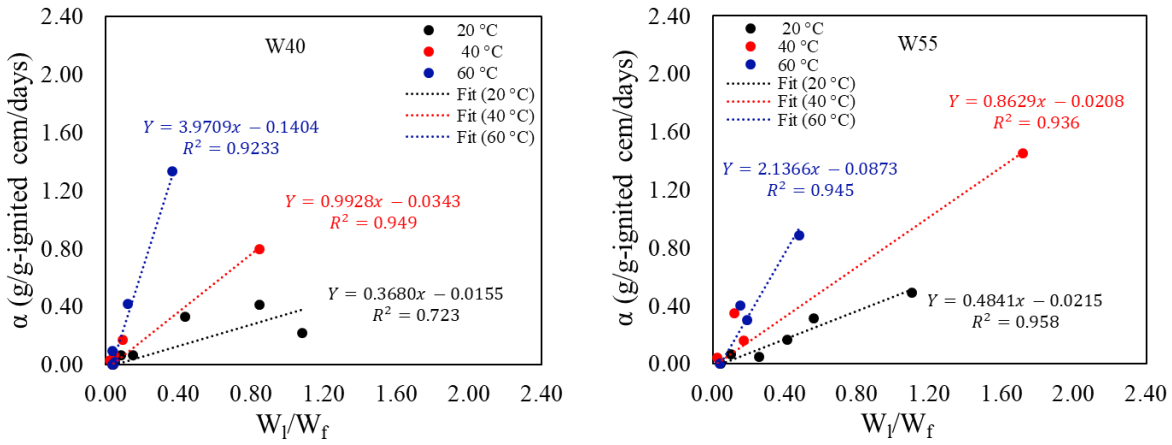

(a) W40 (b) W55

Figure 3.8 Relationships between coefficient α and W_l/W_f for water moving from large pores to fine pores

3.3.2. Activation energy of the rate of exchange between large and fine pores

The Arrhenius plot for the rate of exchange between large and fine pores versus the reciprocal of the absolute temperature is presented in **Figure 3.8,** for W40 and W55. The activation energy divided by the gas constant (R = 8.314 J.K^{-1}.mol^{-1}) is the gradient of these curves. Thus, the activation energies for W40 and W55 are 36 kJ/mol and 35 kJ/mol, respectively, which are very similar values. For comparison, the activation energy of

diffusion can be calculated by **Eq.** (**3.6**), with its Arrhenius plot presented in **Figure 3.10.** Based on this plot, the activation energy of the diffusion process in the studied temperature range is equal to 29 kJ/mol. The same approach can be adopted for the permeability process via **Eq.** (**3.8**)**.** The Arrhenius plot of permeability linked to the water properties is also presented in Figure 3.10**.** If no microstructural change is assumed (by assuming a constant specific surface and porosity), then the activation energy related to the permeability is equal to 14 kJ/mol. However, an additional activation energy should be added to this value, owing to the microstructural modification by considering the porosity and specific surface variations, especially since the difference in evaporable water at 26 days under different temperatures is still negligible, as shown in **Figure 3.7.** By considering the porosity of the material corresponding to this amount of water, the porosity can be assumed to be almost constant for this temperature range. Thus, the activation energy of permeability due to porosity variation will be null and the only remaining source of this activation energy will be the variation of the specific surface.

The temperature dependency of the specific surface seems to be more important than that of the porosity as the term representing this dependency is squared in **Eq.** (**3.8**)**.** However, for a similar material (white Portland cement, with water-to-cement ratio 0.55 and similar mineral composition, and from the same factory) studied in a previous publication [168], the measured specific surface variation according to the temperature was very small. Its corresponding activation energy calculated from the permeability from **Eq.** (**3.8**) will also be negligible (around 2 kJ/mol). Thus, the total activation energy of permeability in the materials used in this study should be slightly higher than 16 kJ/mol if the porosity variation due to temperature is also considered. Both water transport processes give lower values than those experimentally observed, which can be explained by additional microstructure evolution that is not considered in this theory. The microstructural reorganization may be the source of this observed difference, which requires energy to transform the interlayer pores back to gel pores under saturation.

For both mixtures, the curves are not perfectly linear and a double-slope shape can be observed in **Figure 3.9 .** This double-slope shape was also observed previously for the same temperature range under diffusion for ordinary Portland cement (cured for 28 and 90 days) and aluminous cement [169]. In addition, Drout et al. [170] described the temperature dependency of permeability as a non-Arrhenius behavior. Instead, to fit the behavior linearly, they suggested a double exponential function. However, in this case, a double-slope fitting can also be adopted for the four studied cements. In these two published studies, the temperature for which the curves have an inflection point is approximately 40 °C, which is similar to the results of the present study. This difference occurs in parallel with the

substantial increase of gel pore water at 60 °C for both mixtures, as compared to the two other temperatures. For W40, this represents a significant change in microstructure from an equivalent quantity of water between interlayer and gel water to dominant gel pores. For the W55, due to the larger amount of initial gel pores, the classification between gel and interlayer pores was not affected while the gel pore proportion increases with temperature. Thus, this non-perfect linearity can be associated with the variation in the required energy to move water from large to fine pores and to reorganize the microstructure.

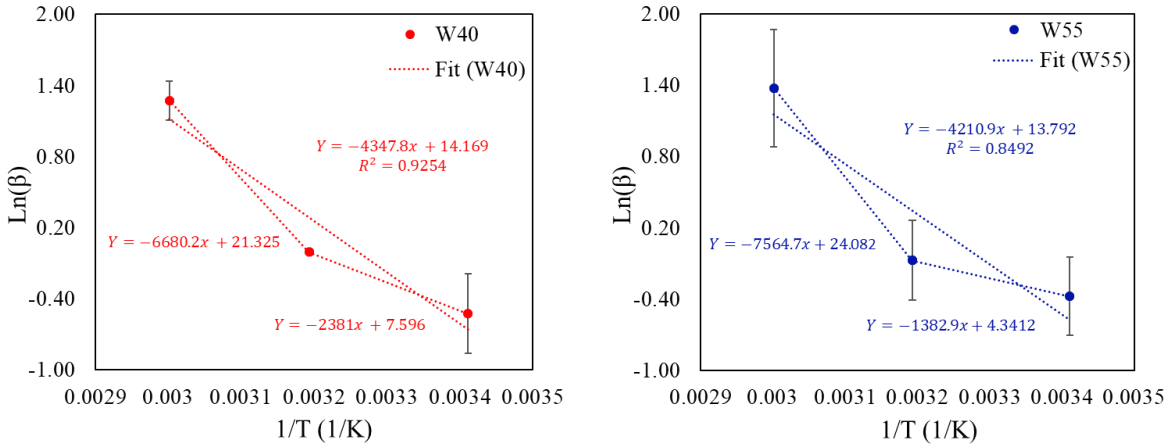

(a) W40 (b) W55

Figure 3.9 Temperature dependence coefficient of β

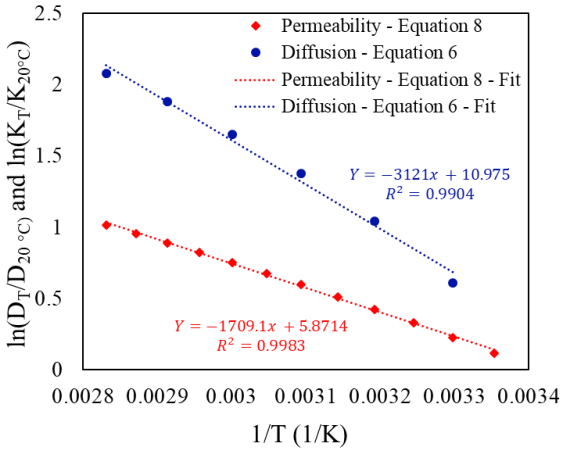

Figure 3.10 Arrhenius plot of diffusion and permeability according to **Eq. (3.6)** and **Eq. (3.8)**

3.4. Conclusions

The water distributions in two different mixtures of white Portland cement paste were investigated through proton-nuclear-magnetic-resonance relaxometry. The water uptake test was performed at three different temperatures: 20 °C, 40 °C, and 60 °C. The water present in four porosities (interlayer, gel, interhydrate, and capillary pores) was measured for the sealed condition and dried condition, and during the first twenty-six days of sorption. Based on the obtained results, the following conclusions can be drawn:

- The interhydrate pores are quickly filled with water at the beginning of the sorption test before emptying into the finest porosities over time.
- The movement of water from different pores to the gel pores increases with time and temperature.
- The rate of water exchange between large pores (capillary pores and interhydrate pores) and fine pores (gel pores and interlayer spaces) was obtained, showing an increasing tendency with temperature
- The activation energy of 35 kJ/mol corresponding to water exchange between large and fine pores was similar for both studied compositions.
- The activation energy obtained from the diffusion or permeability processes based on previous studies was inferior to the measured result. This difference can be linked to the microstructural rearrangement observed experimentally, which is not considered in classical water transport theories.
- A double-slope curve was observed in the Arrhenius plots. The finest microstructure showed an important variation in the proportion of the gel and interlayer pores between the lowest two temperatures (20 °C and 40 °C) and the highest temperature (60 °C), which can be linked to the variation in the necessary energy to move water between pores and to reorganize the microstructure.

4. Water uptake

4.1. Experimental methods

4.1.1. Materials

The materials for this experiment were fabricated according to the construction records from the NPP at the Fukushima Daiichi site [171]. One mixture proportion, shown in **Table 4.1**, was selected from the records. Class II fly ash powder was used according to the Japan. The material properties and mixture proportions for the samples used in this study are shown in **Table 4.2** and **Table 4.3** respectively. The chemical composition of the ordinary Portland cement and fly ash powder as determined by x-ray fluorescence (XRF) is shown in **Table 4.4**. The phase composition of the powdered samples of raw ordinary Portland cement and natural fly ash was determined using x-ray diffraction (XRD) (D8 Advance, Bruker AXS) and Rietveld analysis software (TOPAS ver. 4.2 developed by Bruker AXS), as shown in **Table 4.5** and **Table 4.6**, respectively. **Table 4.7** shows the chemical composition of the fine aggregates. The minerals, which were identified in the samples using polarized micrography and XRD measurements, are listed in **Table 4.8**.

Table 4.1 Example mixture proportions for concrete used in the Fukushima Daiichi Nuclear Power Plant buildings.

	W/C	S/C	Unit amount (kg/m^3)				AE agent amount
			W	C	S	G	
Concrete	0.55	2.39	182	330	790	1000	99 mL

W: unit water content, C: unit cement content, S: unit sand (fine aggregate) content, G: unit gravel (coarse aggregate) content, mL: Millilitres

Table 4.2 Material properties of the mixture components

Material	Notation	Information
Cement	OPC	Ordinary Portland cement (density: 3.16 g/cm^3, specific surface area: 3140 cm^2/g)
Fly Ash	FA	JIS Class II (density: 2.37 g/cm^3, specific surface area: 4210 cm^2/g) (Class C by ASTM C 618)
*Fine aggregate	LS	Crushed limestone sand (excluding fine particles less than 0.15 mm in diameter)
	RS	On-site aggregate (including river sand and fine particles)

Admixture agent	AE	From diluted pulverized Vinsol resin (Yamaso chemical Co. Ltd.)

Table 4.3 Mixture composition of the mortar specimens

Mixture ID	Water to binder ratio	FA (%)	Unit amount (kg/m^3-Conc.)					AE agent (mL)
			Water	Binder		LS	RS	
				OPC	FA			
OPC-LS	0.55	0	182	330	-	790	-	86
FAC-LS		15		280.5	49.5	790	-	255
FAC-RS						-	790	123

mL: Millilitre

Notes: (1) Added gypsum and adjusted the total SO_3 content in the powder to 2.5%. (2) The AE agent was used by diluting Vinsol (Yamuna Chemical Co., Ltd.) one-hundred times. The AE agent amount represents the target air amount and was added to make 7.0 ± 1.0%.

Table 4.4 Chemical composition as determined by XRF analysis (mass %).

Cement	LOI	SiO_2	Al_2O_3	Fe_2O_3	CaO	MgO	SO_3	Na_2O	K_2O	TiO_2	P_2O_5	MnO	SrO	Total
OPC	2.26	20.54	5.18	2.92	64.30	0.90	2.04	0.35	0.32	0.31	0.57	0.08	0.05	99.82
FA	2.41	56.23	30.89	3.05	1.66	0.92	0.23	0.36	1.24	1.67	0.49	0.02	—	99.17

Table 4.5 Mineral composition of the OPC cement as determined by XRD/Rietveld analysis (mass %).

C_3S	C_2S	C_3A	C_4AF	Periclase	Basanite	Gypsum	Calcite	Total
50.35 ± 1.22	23.27 ± 2.07	8.79 ± 0.30	10.10 ± 0.37	0.38 ± 0.12	1.90 ± 0.155	0.16 ± 0.04	5.01 ± 0.39	99.96

Table 4.6 Mineral composition of the fly ash as determined by XRD/Rietveld analysis (mass %).

Quartz	Mullite	Magnetite	Hematite	Calcite	Rutile	Glass	Total
8.71 ±	26.42 ±	0.11 ±	0.27 ±	0.64 ±	0.33 ±	63.49 ±	99.97

0.32	0.54	0.05	0.06	0.14	0.26	1.03	

Table 4.7 Chemical composition of the fine aggregates as determined by XRF (mass %).

Fine aggregates	LOI	SiO_2	Al_2O_3	Fe_2O_3	CaO	MgO	SO_3	Na_2O	K_2O	TiO_2	P_2O_5	MnO	Total
RS	1.03	79.51	8.75	3.30	1.85	1.45	0.01	1.86	1.69	0.35	0.05	0.10	99.95
LS	41.66	5.35	0.72	0.26	47.03	4.57	0.02	0.04	0.15	0.03	0.03	0.00	99.86

Table 4.8 Minerals observed in the fine aggregates from the micrograph and XRD/Rietveld analysis.

Fine aggregates	Quartz	Plagioclase	Orthoclase	Chlorite	Mica	Amphibole	Calcite	Dolomite
RS	x	x	x	x	x	x		
LS							x	x

x: target phase was confirmed by XRD/Rietveld analysis.

4.1.2. Mixing and curing condition

The mortar was mixed with a Hobert mixer. Each batch had a total mixture volume of 4 L. The mortar was placed in a mold with a cross-sectional area of 50 × 50 mm^2. The specimens were cured at 40 °C in moist condition (100% RH) for three months. Then, they were cut into 20 × 20 × 50 mm^3 blocks using a diamond precision saw as shown in **Figure 4.1**. This accelerated curing at 40 °C was applied in order to obtain the sufficient degree of hydration (Reaction degree of glass phase in FA was about 50% (selective dissolution method) and degree of hydration of OPC was about 91% (XRD/Rietveld analysis)) in order to obtain the similar reacted condition to that in aged structure.



(a) Hobert mixer (b) 50 × 50 mm^2 (c) Curing condition at 40 °C

Figure 4.1 Preparation of mortar samples

4.1.3. Water absorption test method

After the sample was homogenously dried at 105 °C or at 20 °C and approximately 40% RH, all surfaces except for one, with dimensions of 20 × 20 mm, were covered with aluminum adhesive tape. For the drying condition at 105 ± 2 °C, a heating chamber was used . Each specimen was inserted in a glass bottle, and a silicon tube connected the glass bottle to a gas washing bottle placed outside of the heating chamber. The gas washing bottle contained calcium hydroxide aggregates, which prevented the carbonation of the specimens as shown in **Figure 4.2**. The drying process took approximately one days. For the condition at approximately 40% RH and 20 °C, a saturated salt solution (solutions containing pure NaI can be used to maintain an RH of approximately 39.65% at 25 °C [172] was used to maintain a constant relative humidity as shown in **Figure 4.3**. The drying period took 93 days, ensuring a quasi-equilibrium condition (0.01%/day according to [24]) for all samples. This 105 °C was selected as the reference which is the most commonly used and 20 °C and 40% RH was selected since this drying state was similar to the drying condition on the surface of thick concrete wall in nulcear power plant (an estimation was made based on references [7], [8]).

Figure 4.2 Oven drying at 105 ^{0}C

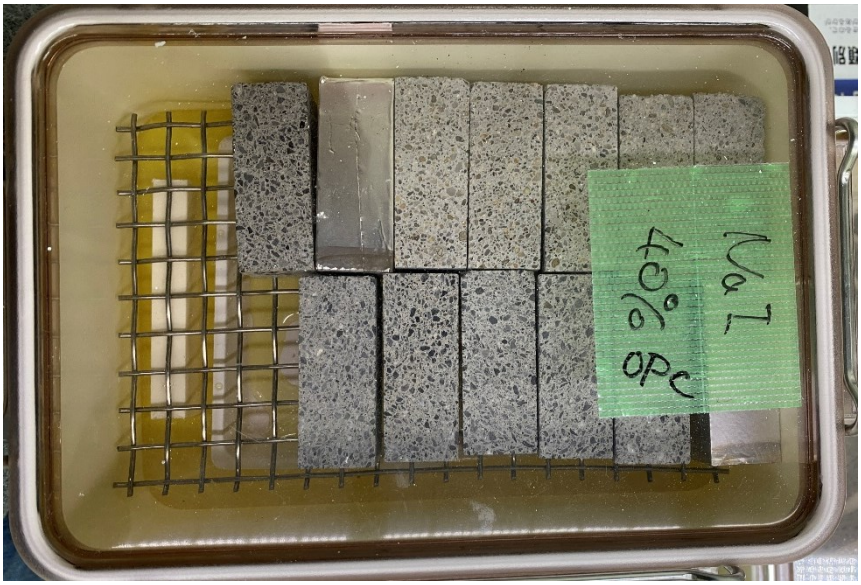

Figure 4.3 Drying at RH-40% at 20 °C with salt saturated solution (NaI)

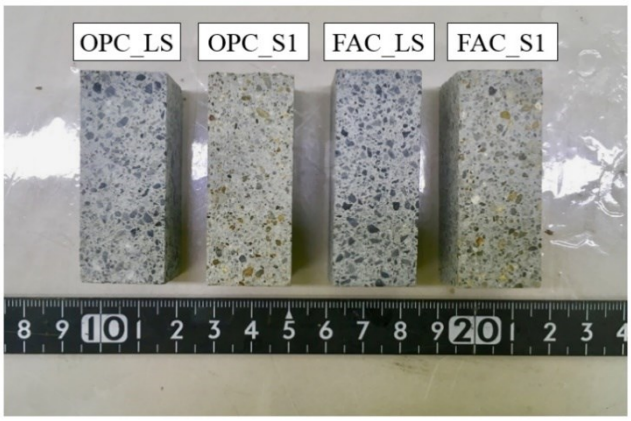

Figure 4.4 Overview of the mortar specimens used for X-ray CR experiment

As shown in **Figure 4.5** and **Figure 4.6**, a tap water absorption test was conducted from the bottom of the specimen. The temperature of the water and the ambient environment was controlled at the target temperatures, 20 ± 2 or 60 ± 5 °C. The specimen and a water reservoir were placed inside the x-ray CT scanner. During the twenty-four-hour water absorption experiment, transmission images of the sample were taken intermittently. Immediately after transmission imaging, the specimen was removed, and the mass was measured using an electronic balance.

For measurements at 60 °C, the water absorption test was performed in a 60 °C

heating chamber. The specimen was removed from the furnace for transmission imaging, and then the water absorption test was restarted in the furnace. It was expected that the specimen's temperature would decrease during the transparent imaging. However, it took approximately 150 seconds to remove the sample from the furnace, image it using x-ray radiography, and return it to the furnace. As the interval between imaging was several hours, it was determined that the sample temperature dropped by approximately 5 °C during this 150 second interval.

The samples were labeled according to their mixture identity, drying condition, and experimental temperature. For example, an OPC-LS specimen dried at 105 °C and measured at 20 °C was labeled “OPC-LS-105C -20”.

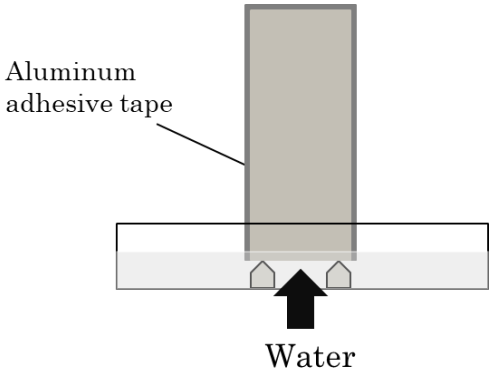

Figure 4.5 Schematic representation of the water absorption process in a controlled chamber

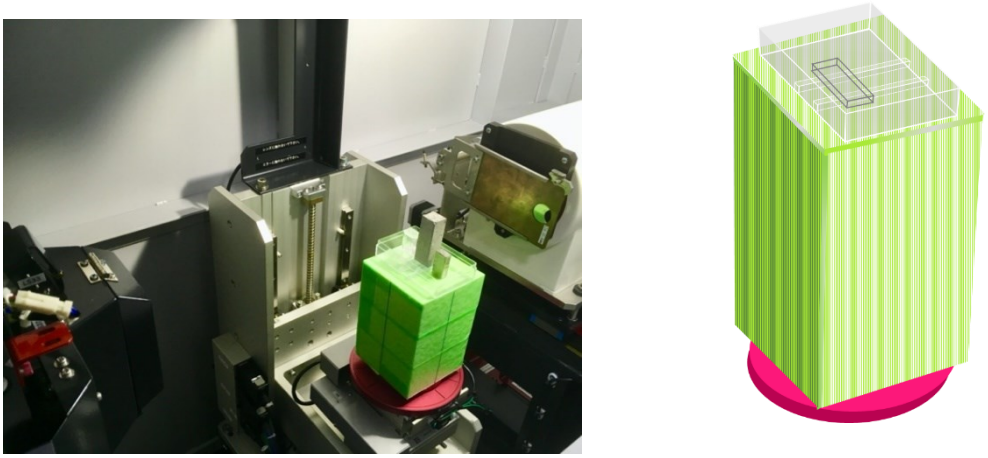

Figure 4.6 Schematic representation of the water absorption process and experimentalsetup for x-ray radiography measurement

4.1.4. X-ray imaging process

X-ray imaging techniques have several advantages for capturing the water absorption behavior of cementitious materials. When the specimen is exposed to air during the water absorption test, the water penetration depth shows a concave (∧-shape) distribution inside, and the results observed at the surface are not sufficient to evaluate the penetration depth. Secondly, from the X-ray attenuation, the mass difference can be estimated using a calibration curve from the obtained image. It should be noted that there is a limit to the thickness (or size) of the sample depending on the X-ray source and detector.

For X-ray computed radiography (CR) observations, the inspeXio SMX-100 CT (Shimadzu Corporation) was used. The maximum tube voltage and current in this instrument are 100 kV and 120 μA, respectively. The Feldkamp, Daci, Kress (FDK) method, a cone-beam reconstruction method, was used as the algorithm for image reconstruction [173]. In this study, the tube voltage was 100 kV, the tube current was 110 μA, the SDD (distance from the x-ray focus to the detector) was 500 mm, the SRD (distance from the x-ray focus to the sample) was 350 mm, and the number of feed lines was four. Ten measurements were conducted for each sample, and radiography was performed using a Cu filter with a thickness of 0.4 mm. To convert the brightness of the transmitted image to useable measurement values, iron (3 mm thick) and quartz (16 mm thick) were used as references. The grayscale range of the resultant image was normalized, and the spatial resolution of the picture was 0.0176 mm/pixel.

As shown in **Figure 4.7**, the moisture content was visualized by subtracting the initial image (before water absorption) from the x-ray transmission image taken six hours into the water absorption experiment. It is important to subtract the background from the transmission image for each water absorption process to determine the penetration depth. Using this method and the differences in gray scale values in the images, the infiltration depth of the liquid water and the total volume of absorbed water in each sample was calculated. The open-source image analysis software ImageJ [174] was used for processing and grayscale digitization. X-ray computed radiography (X-CR) was used to image the water absorption for 24 hr at 20 °C and 60 °C respectively. One sample per once condition was measured in this experiment.

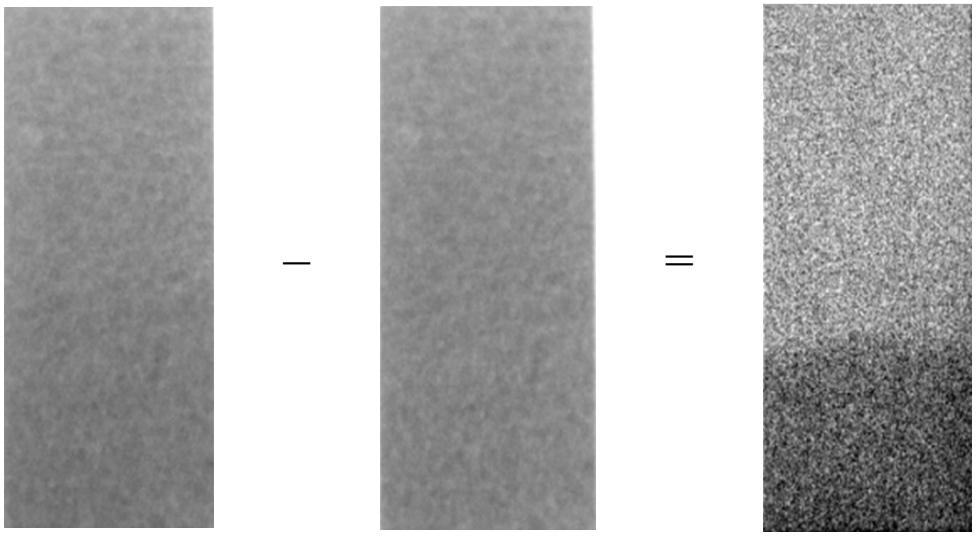

Six hours into the water absorption process | Before the water absorption | Difference in water absorption.

Figure 4.7 X-ray transmission images before and after six hours of water absorption. The width of the image is about 2 cm.

4.1.5. Quantification of water

The attenuation behavior of the x-rays could be described using the Beer-Lambert law. The water absorption levels were quantified from the x-ray radiography images using process evaluated by Roels and Carmeliet (2006). The amount of water absorbed for each pixel (ΔC_w) can be calculated as:

$$\Delta C_w * \mu_w = -\frac{\rho_w}{d} \ln \frac{I_{wet}}{I_{dry}}, \tag{4.1}$$

where I_{wet} is the attenuated x-ray intensity through a wet mortar specimen, I_{dry} is the attenuated x-ray intensity through a dried mortar specimen, ρ_w is the density of water (g/cm^3), d is the thickness of water (cm), and μ_w is the nominal attenuation coefficient of water in the mortar (cm^{-1}).

To calculate the water absorption from the discretized gray scale values from the x-ray CR images, Equation (1) was used with ρ_w = 1.00 g/cm^3. The total mass change due to the water evaporation should be correlated to the integration of ΔC_w for all pixels. Based on the experiment, μ_w was evaluated by fitting the experimental data to correlate the change in mass. As shown in **Figure 4.8**, μ_w was determined to be 0.0185 cm^{-1} in our measurement system.

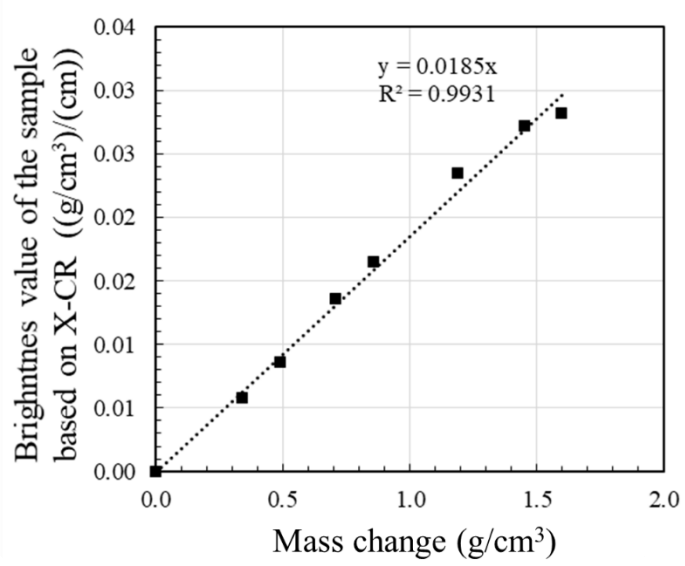

Figure 4.8 Relationship between the change in mass and the change in brightness value in the x-ray transmission images

4.2. Results

4.2.1. Visualization of water movement of mortar specimen drying at 105 °C at 20°C

The representative results for OPC-LS-105C-20, FAC-LS-105C-20, and FAC-RS-105C-20 are shown in **Figure 4.9**. The dark area represents the region in which the water is absorbed in the mortar specimen. The figure can be used to evaluate the relationship between average brightness and distance from water absorption surface. The results for OPC-LS-105C-20, FAC-LS-105C-20, and FAC-RS-105C-20 are summarized in **Figure 4.10**. The change in the moisture distribution was quantitatively analyzed using these figures. Additionally, this data was used to calculate the penetration depth and the volume of water absorbed in the sample. The results for OPC-LS-105C-20 are shown in **Figure 4.11**.The absorbed water values were normalized per unit of projected area. As each specimen had dimensions of 20 × 20 × 50 mm^3, the total absorbed water can be calculated by a factor of 1000 based on the sum of difference of normalized gray values. As shown in **Figure 4.11** shows the anomalous behavior of water adsorbed in cement-based materials, a phenomenon characterized by water absorption behavior that deviates from the linear relationship between water

penetration depth or volume of water absorbed and the square root of time. According to these results, the penetration depth began to deviate from the linear curve (denoted as point A) at approximately 20 $min^{0.5}$ (400 min after the first contact with water), while the water absorption amount began its deviation (denoted as point B) at approximately 25 $min^{0.5}$. After approximately 30 $min^{0.5}$, more significant reduction of water absorption was confirmed. As the experiment proceeded, maximum water amount is slightly increased as the depth is increased, consequently, between the timings of point A and point B, the discrepancy between penetration depth and the water absorption amount was confirmed. After the point B where the corresponding depth is from 15 mm to 22 mm, the maximum water absorption is start to decrease and distribution of water (as a function of the distance from the water contact surface) near the penetration depth became broad, and then the significant reduction of rate of absorption was observed in **Figure 4.11**. Currently mechanism of the slight increase of the maximum water adsorption at the depth ranging from 0 to 15-22 mm was not clear, and one possible explanation is an artifact due to x-ray scattering from the water at the bottom. On the contrary, after the point B, the trend of decrease in the maximum absorption as the increase of penetration depth and broadening of the water distribution near the penetration depth can be explained by the connectivity of pores. If there is a large pore in which the liquid water can not transport and fill in, the maximum of water will be decreased at the same depth of the large pore. As a result, the rate of water absorption is decreased against the square root of time, while the penetration depth can keep the linear relationship against the square root of time. In summary, in **Figure 4.10**, there are two anomalies of moisture transport. One is the inflection point of the penetration depth as a function of the square root of time (point A), and the deviation between the penetration depth and the water absorption against the square root of time. Hereafter, point A is mainly discussed.

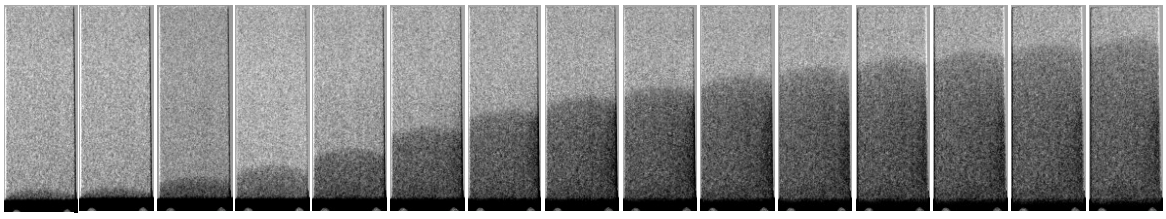

(a) Visualization of water penetration into OPC-LS at 20 °C mortar specimen

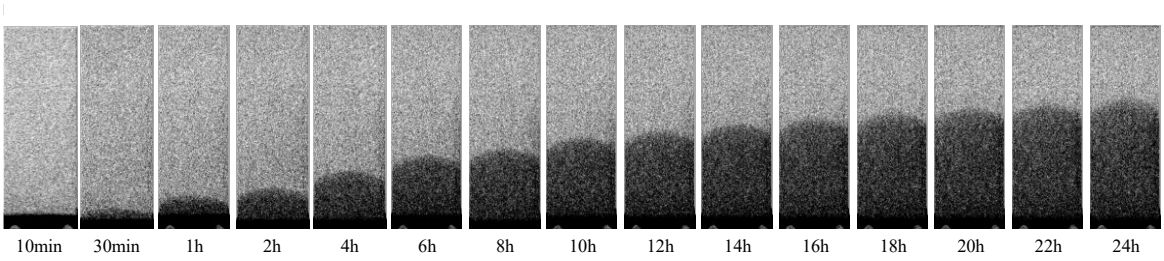

(b) Visualization of water penetration into FAC-LS at 20 °C mortar specimen

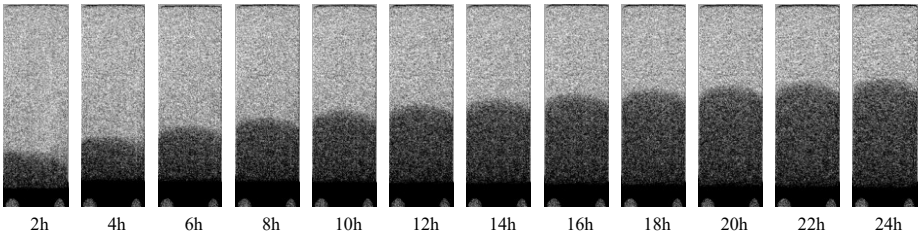

(c) Visualization of water penetration into FAC-RS at 20 °C mortar specimen

Figure 4.9 Visualization of water penetration into mortar specimens drying at 105 °C during the first 24 hours by X-ray computed radiography (X-CR)

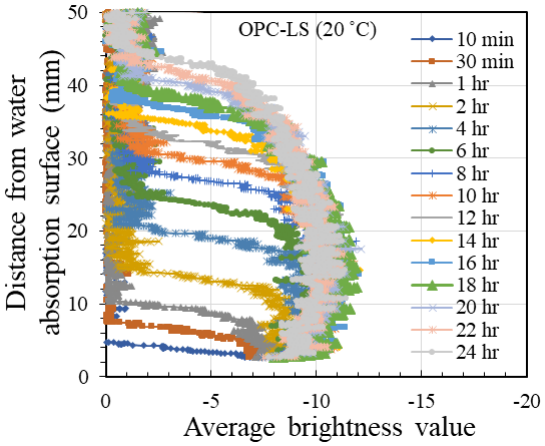

(a) OPC-LS-105C-20

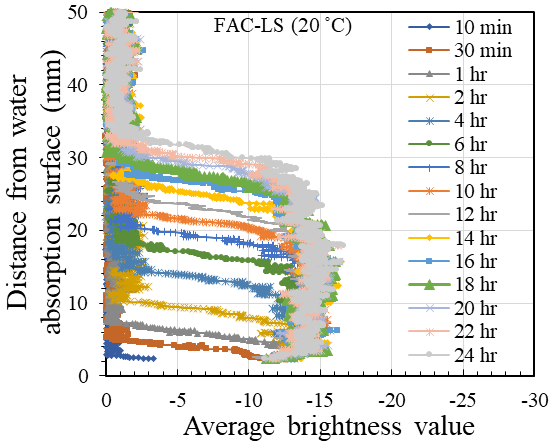

(b) FAC-LS-105C-20

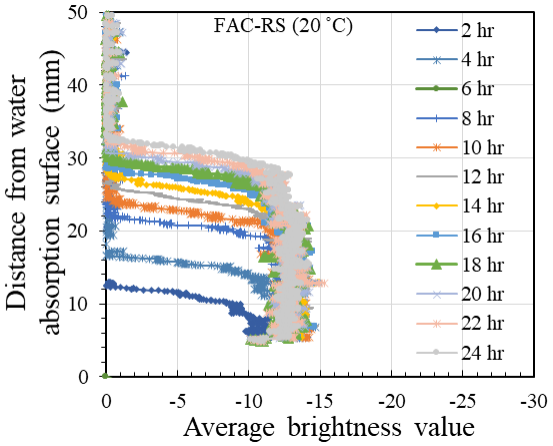

(c) FAC-RS-105C-20

Figure 4.10 Results of the x-ray computed radiography (average brightness value) for the water absorption, in which water at 20 °C was absorbed from the bottom surface of the mortar specimens dried at 105 °C

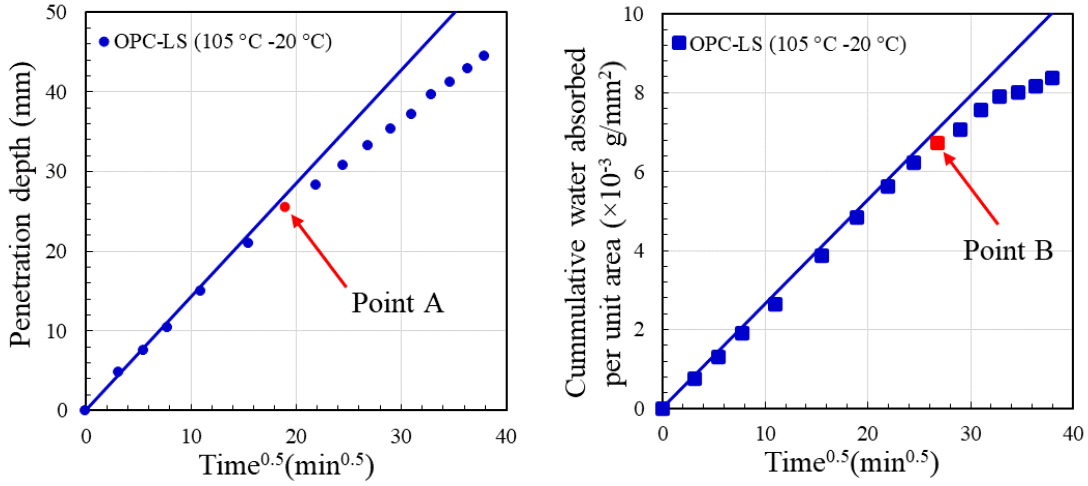

(a) Penetraiton depth (b) Cummulative water absorbed

Figure 4.11 Penetration depth and cumulative water content per unit area of OPC-LS-105C-20. The points represent experimental data, while the solid lines represent the sorptivity of specimens at the beginning of experiment, determined by the first several experimental data points.

The experimental results are summarized in **Figure 4.12** . **Figure 4.12 (a)** shows the effect of cement type on the rate of water absorption. At the beginning of the water absorption experiments, the water absorption coefficient rate (sorptivity with a unit of mm/min$^{0.5}$) of the FAC mortar was approximately 70% that of OPC mortar. Interestingly,

the anomalous trend was much stronger for OPC mortar than for FAC mortar (see **Figure 4.13 (a)**); FAC showed a more linear trend as a function of the square root of exposure time. These trends are consistent with those reported in previous studies [175]–[179]. The morphology of calcium silicate hydrate (C-S-H), a major hydrate in cement-based materials and a source of strength in concrete, can be changed by changing the calcium silicate (Ca/Si) atomic ratios [180]–[182]. C-S-H with a lower Ca/Si ratio has a foil-like structure, which may be a major reason for its lower diffusion coefficient and lower sorptivity, being formed by the pozzolanic reaction**. Figure 4.12 (b)** shows a little effect of rock type on the sorptivity. Two possible factors that could affect the sorptivity rate. One is the interfacial transition zone, which can be changed by the reaction of cement hydrates and rock-forming minerals, as calcium aluminate hydrates can be formed on the surface of calcite , while the portlandite can be the major phase on the quartz [183]. It should be noted that the interfacial transition zone does have significant impact on mass transfer in concrete rather than the microcracks caused by pre-drying condition [184]. The other is the presence of clay minerals (but only few percent) in sand which can absorb the water. From **Figure 4.12 (b)**, it is concluded that these two factors were not significant for the aggregate used in the Fukushima Daiichi plant.

Temperature has a significant effect on the sorptivity, as confirmed in **Figure 4.12 (c)**. At the beginning of the water sorption process, the sorptivity of OPC-LS-105C-60 was approximately 35% higher than that of OPC-LS-105C-20. However, the anomalous behavior of OPC-LS-105C-60 is much greater than that of OPC-LS-105C-20, and after 24 hr, the penetration depth in OPC-LS-105C-60 was 28% smaller than in OPC-LS-105C-20.

All the measured sorptivity was summarized in **Table 4.9**. Based on the Washburn equation [139], the penetration depth can be evaluated as

$$L = \sqrt{(\gamma r \cos\theta / 2\mu) \cdot t}, \tag{4.2}$$

where L is the penetration depth, γ is the surface tension (N/m), μ is viscosity (Pa○s), r is the radius of the pore (m), and t is the exposure time (s). When the temperature is changed, the viscosity and the surface tension of the pore solution changes due to the thermodynamic behavior of water molecules. Additionally, the radius of pore changes due to thermal deformation in the solid components of the mortar structure. the structural deformation in the mortar contributed to a change on the order of 10^{-4}. The surface tension of water is 72.75 and 66.17 N/m at 20 °C and 60 °C, respectively, and the viscosity of water is 1.002 and 0.467 (mPa○s) at 20 °C and 60 °C, respectively. The ratio of $\sqrt{\gamma/\mu}$ at 60 °C to that at 20 °C was 1.40; this value is a bit larger than the experimental value of 1.16 – 1.25, but it is reasonably concluded that this is the major factor of the change in the initial sorptivity (the first slope of the sorptivity after water contact, less than 240 min.). The

viscosity and the surface tension of the pore solution are affected by ion concentration. The first-order estimation did not consider concentration; however, the sorptivity could be roughly evaluated by considering the changes in surface tension and viscosity of pure water by using a factor of 0.5.

The FAC specimens also showed stronger anomalous behavior at higher temperatures. The penetration depth of FAC-RS-105C-60 after twenty-four hours was 15% smaller than that of FAC-RS-105C-20, as shown in **Figure 4.12 (d)**. These results show trends that are consistent with those for OPC mortar.

For the mild drying process at 40% RH, the sorptivity rate decreased, as confirmed in **Figure 4.12 (e)** and **(f)**. It is found that the anomaly appeared much earlier when mortars were pre-dried at 40% RH, as shown in **Figure 4.13(b)**.

The anomalous behavior of water absorption in cement-based materials has been discussed in the literature for more than twenty years [14], [19]. The possible mechanisms for this behavior include hydration, cement hydrate precipitation, inhomogeneous micro-cracking in the specimen from the pre-drying process, concrete swelling, and dynamic microstructural behaviors resulting from the colloidal nature of C-S-H [21]–[23], [26], [28], [185]–[189]. In addition, one may think that the 5-surface sealed condition will create air entrapment inside the specimen and a back-pressure cause the change in rate of penetration. It is possible and authors can not deny this possibility. But if this is the dominant mechanism, the inflection point shown in **Figure 4.12** should be occurred at the similar penetration depth rather than the similar elapsed time.

In a companion paper, Kiran et al.[30], showed that the water exchange from large pores to fine pores in different temperature conditions could be monitored by ^{1}H-NMR relaxometry [30]. These results could be attributed to dynamic microstructural changes in C-S-H during water absorption. If both sorption anomalies in OPC mortar and FAC mortar mainly occur from dynamic structural changes in C-S-H and local water exchange from large pores to fine pores, the difference in behaviors between the two mortars can be explained by the morphology of C-S-H. The FAC mortar contains C-S-H with a lower Ca/Si ratio; as a result, the rate of moisture transport decreases. The lower sorptivity of FAC mortar is evidence that these C-S-H characteristics affect adsorption in the mortars. This macroscopic behavior should also affect the local water exchange from larger pores to fine pores since the foil-like shape of C-S-H increases the material's tortuosity. The impact of C-S-H morphology is a major factor that determines the sorptivity of mortar for specimens with similar water to binder ratios and aggregate contents. At higher temperatures, ^{1}H-NMR relaxometry confirms the rapid water exchange between large pores and fine pores. After the mortar is exposed to water, the C-S-H in the mortar near the water contact surface

begins to expand, resulting in the rapid closure of the larger pores. Thus, as the larger pores rapidly close, the channels that carry large volumes of water into the mortar collapse. Thus, this is the mechanism for the strong and rapid anomalous behavior that occurred at higher temperature conditions. When the pre-drying conditions were incomplete and water remained in the fine pores, the number and the size of pores in the final specimen were smaller than in the mortars exposed to the more severe pre-drying condition at 105 °C. Consequently, the water penetration rate decreased. In addition, the deviation (anomaly) in the specimens dried at 40% RH began much earlier than for specimens pre-dried at 105 °C, as the larger pores closed faster when water was already present in the C-S-H.

The pre-drying procedure could also be the cause of the cracking of the specimens [184], [186], [190], [191]. The shrinkage of the hardened cement paste in the mortar was much larger than that of the fine aggregate, which inhibited the shrinkage and caused the cracking of the hardened cement paste in the mortar specimens. It is also possible that the hardened cement paste expands due to the expansion of the C-S-H agglomeration structure after contact with water; as discussed by Alderete et al. [22], the expansion of the C-S-H agglomeration structure reduces the widths of micro-cracks around the fine aggregates. In the present experiment, the anomaly is still controlled by the nature of C-S-H, since the process of the narrowing the width of micro-cracks is always associated with the expansion of the C-S-H agglomeration structure.

Therefore, it is concluded that the anomalous sorptivity of water in cement-based materials could be qualitatively explained by the nature of C-S-H. This conclusion is consistent with a recent discussion by McDonald et al. [192].

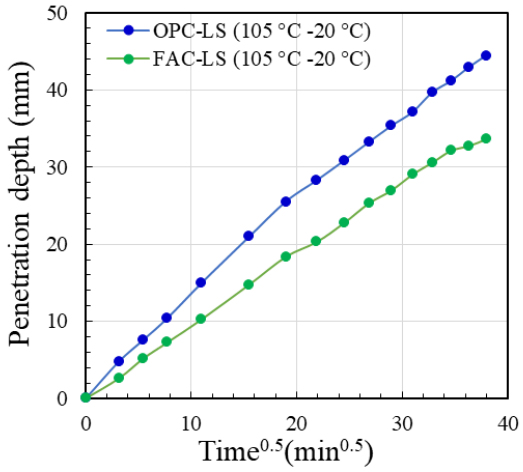

(a) Impact of cement type

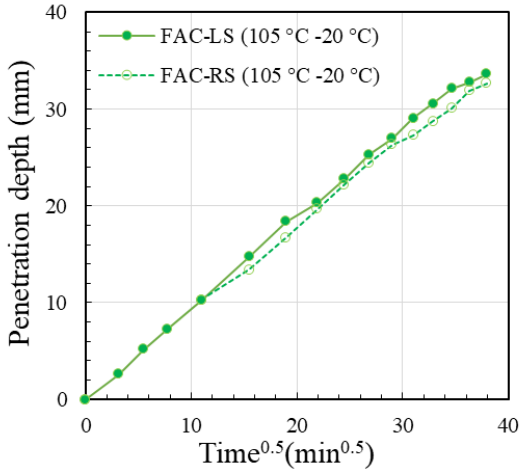

(b) Impact of aggregate type

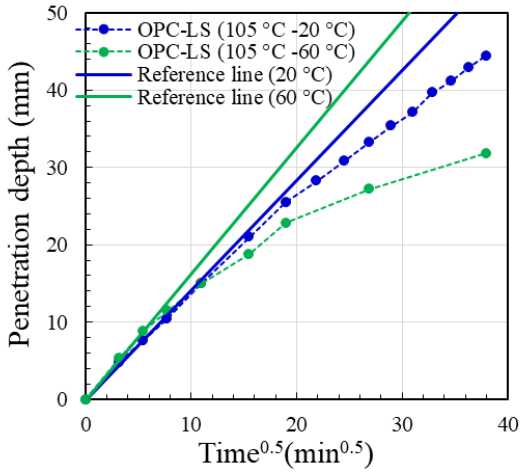

(c) Impact of temperature on OPC mortar

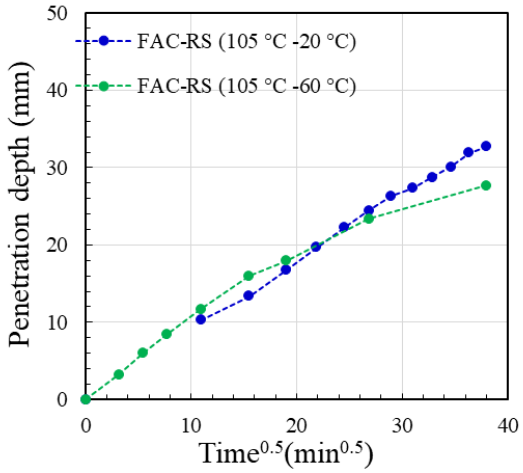

(d) Impact of temperature on FAC mortar

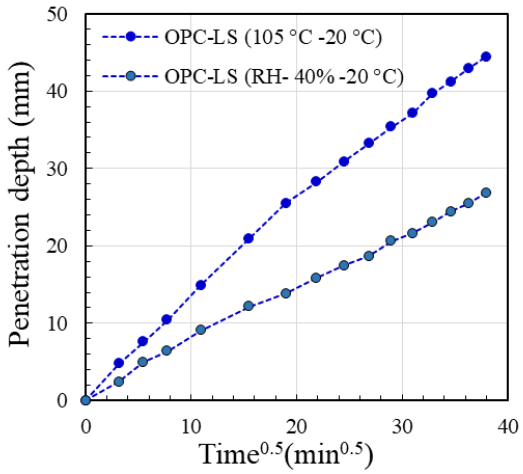

(e) Impact of pre-drying conditions on OPC mortar

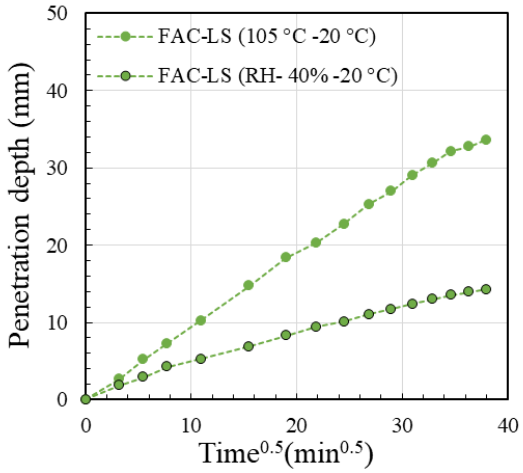

(f) Impact of pre-drying conditions on FAC mortar

Figure 4.12 Penetration depth of water in the mortar over time: (a) impact of cement type (OPC vs. FAC), (b) impact of aggregate type (limestone vs. sandstone containing clay minerals), (c) impact of temperature on OPC mortar (20 °C and 60 °C), (d) impact of temperature on FAC mortar (20 °C and 60 °C), (e) impact of pre-drying conditions on OPC mortar (drying at 105 °C or at 20 °C and 40% RH), and (f) impact of pre-drying conditions on FAC mortar (drying at 105 °C or at 20 °C and 40% RH). The solid lines shown in (c) represent the sorptivity slope at the beginning of the experiments

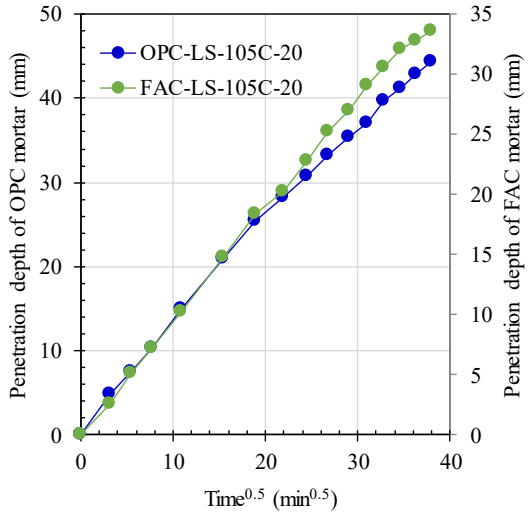

(a) OPC and FAC

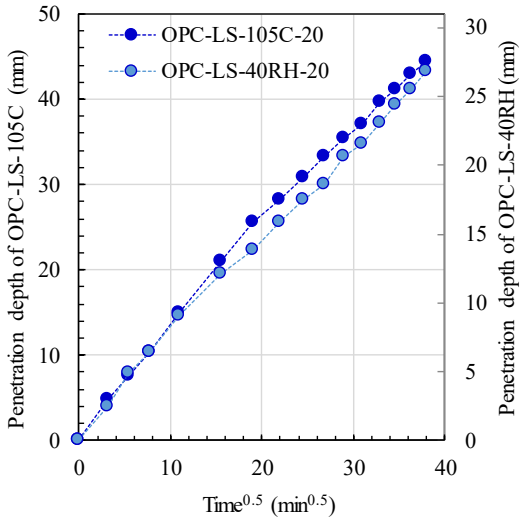

(b) Pre-drying condition at 105°C and at 40% RH and 20°C.

Figure 4.13 Comparisons of anomalous behavior trends for (a) OPC mortar and FAC mortar and (b) pre-drying conditions at 105 °C and at 40% RH at 20 °C for OPC mortar

Table 4.9 Measured sorptivity (mm/min$^{0.5}$).

	OPC-LS-105C-20	FAC-LS-105C-20	FAC-RS-105C-20	OPC-LS-105C-60	FAC-LS-105C-60	FAC-RS-105C-60	OPC-LS-40RH-20	FAC-LS-40RH-20
Initial *	1.34	0.94	0.92	1.67	1.09	1.076	0.87	0.54
After 1-day **	1.17	0.89	0.86	0.84	0.73	0.73	0.71	0.38

*: the initial sorptivity was calculated by the linear fitting of the data within 240 min. after water contact. **: the sorptivity after 1 day is calculated as a tangent between origin and the data at 24 hours after water contact

4.3. Numerical analysis

4.3.1. Background and modeling

As discussed in Section 3, the anomalous water sorption in cement-based materials can be explained by the colloidal nature of C-S-H. In this section, the anomalous behavior associated with microstructural changes and temperature is discussed. To explain these phenomena, a simple numerical moisture transport model is introduced.

4.3.1.1. Local moisture water exchange from large pores to fne pores

In a previous study [30], the local water exchange between larger pores and fine

pores was modeled by **Eq. (4.3):**

$$\frac{\partial W_F}{\partial t} = \alpha W_L, \quad \alpha = \beta\,(W_L/W_F) \tag{4.3}$$

where W_F is the water in fine pores (in the interlayer spaces and gel pores in hardened cement paste) (g/g-solid), W_L is the water in large pores (interhydrate pores and capillary pores) (g/g-solid), α and β are coefficients representing the rate of moisture transport from large pores to fine pores (/s), and t is time. The total water content, W (g/g-solid), can be determined according to

$$W_L + W_F = W. \tag{4.4}$$

4.3.1.2. Moisture transport

Sakata experimentally determined that the water diffusion coefficient in concrete is a function of water content and proposed a simple model [193]. Based on their model, the following equation was applied in this study:

$$\begin{cases} R \geq 0.8 : K_s \\ R > 0.8 : \quad K_o + \dfrac{K_s - K_o}{1 + \left(\dfrac{0.8 - R}{0.8 - R_c}\right)^n} + \dfrac{K_s - K_o}{1 + \left(\dfrac{0.8}{0.8 - R_c}\right)^n} \cdot (R - 0.8) \end{cases} \tag{4.5}$$

where K_o is the moisture transfer coefficient in a dry sample (cm^2/s), K_s is the moisture transfer coefficient in a sample in its saturated condition (cm^2/s), R_c is the relative moisture content at the inflection point, R is the relative water content (water content per the maximum water capacity, in g/g-solid), and n is an experimental constant. An example of the application of **Eq. (4.5)** in this study is shown in **Figure 4.14**.

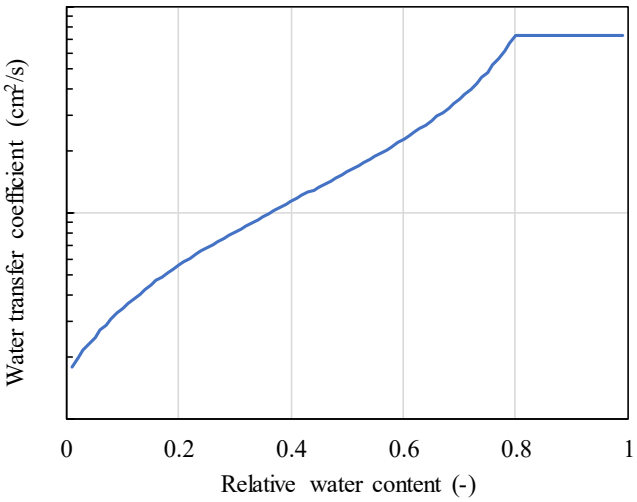

Figure 4.14 Example of the function determined by Equation (5.5). In the calculation process, the maximum value changes with time due to changes in the microstructure

Additionally, changes in the microstructure can also be incorporated with the moisture transfer coefficient. The following equation according to McDonald et al.[192] was adopted:

$$K_s = \frac{1}{\frac{R_F}{K_F} + \frac{(1 - R_F)}{K_L}}, \qquad \textbf{(4.6)}$$

where K_F is the moisture transfer coefficient in fine pores (cm²/s), K_L is the moisture transfer coefficient in large pores (cm²/s), and R_F is the relative water content in fine pores (W_L/W_o, where W_o is the maximum water content).

4.3.2. Results and discussion

The parameters used in the calculations are summarized in **Table 4.10**. The calculation was performed using an implicit finite differential method with an incremental time step of 0.1 hours and a spatial span of 1 mm. The calculation results are compared with the experimental results in **Figure 4.15**. The general trends observed experimentally are well reproduced by the simplified model.

Table 4.10 Parameters for the numerical model, where $\boldsymbol{K_{F,20}}$ and $\boldsymbol{K_{L,20}}$ are water transfer coefficients in fine pores and large pores at 20 °C, respectively. For calculations at 60 °C, a factor of 1.4 can be applied.

Parameters	20 °C	60 °C	Additional comments
R_c	0.70	0.70	Fitted
n	0.28	0.28	Sakata (1983)
β (/day)	0.5	3.5	Kiran et al. (2020)
$K_{F,20}$ (cm²/day)	2.8	1.2	$\frac{K_{F,60}}{K_{F,20}} = 1.40$
$K_{L,20}$ (cm²/day)	100.0	200	$\frac{K_{L,60}}{K_{L,20}} = 1.40$

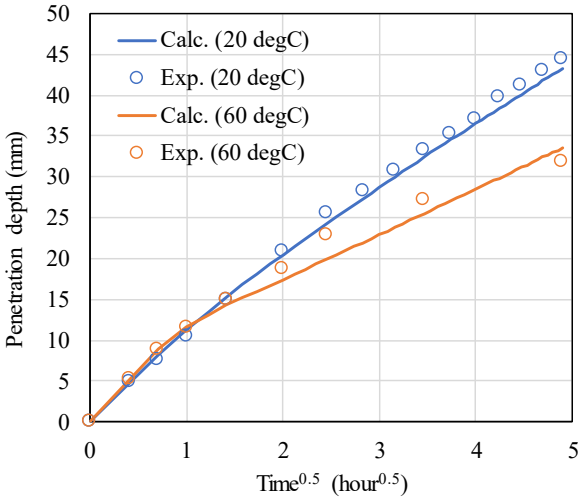

Figure 4.15 Calculated results compared with the experimental results at 20 and 60 °C.

In the present modeling, an inconsistency in the values for $K_{F,20}$ and $K_{L,20}$ can be observed, which represents the moisture transfer coefficients in fine pores and large pores, respectively, at 20 °C and 60 °C. This discrepancy appears to be inappropriate. However, several reports have shown that the C-S-H packing density, interlayer spacing, and the microstructures change with temperature [15], [194]–[196]. According to these studies, the interlayer spacing for specimens at 10 °C is 35% larger than that at 60 °C, and samples at 60 °C were associated with increased pore size (capillary and interhydrate pores). It is quite possible that the apparent water transfer coefficient in fine pores decreases due to narrowed necking pores and increased viscosity, while the apparent water transfer coefficient in large pores is increased due to the greater pore width and

connectivity. Since these trends could only be qualitatively observed, further validation in a future study is recommended. In mortar, the difference between the thermal expansion coefficient of hardened cement paste and aggregate could affect the water transport near the surface of the aggregates. However, as the effects are on the order of 10^{-4}, the authors do not believe that these effects are significant for the measurement results.

Based on these calculations, several phenomena were confirmed. First, the relationship between the penetration depth and the square root of the exposure time followed bilinear trends. The first slope was determined by the pore size distribution in the hardened cement paste under the pre-drying condition. The second slope was determined by the pore size distribution of the hardened cement paste after re-saturation. In the present finite differential calculations, the node that was exposed to the water reservoir controlled the rate of water supply through the mortar due to changes in the microstructure (see in **Figure 4.16**). The trends show that after the dynamic structural changes and increase in pore water volume, the system reached a quasi-steady state. Although the microstructures did not reach a stable state, a linear relationship is observed. In the present calculations, the balance of W_F and W_L with K_F and K_L resulted in a nearly constant slope after ten hours of water exposure at 20 °C and ten hours at 60 °C.

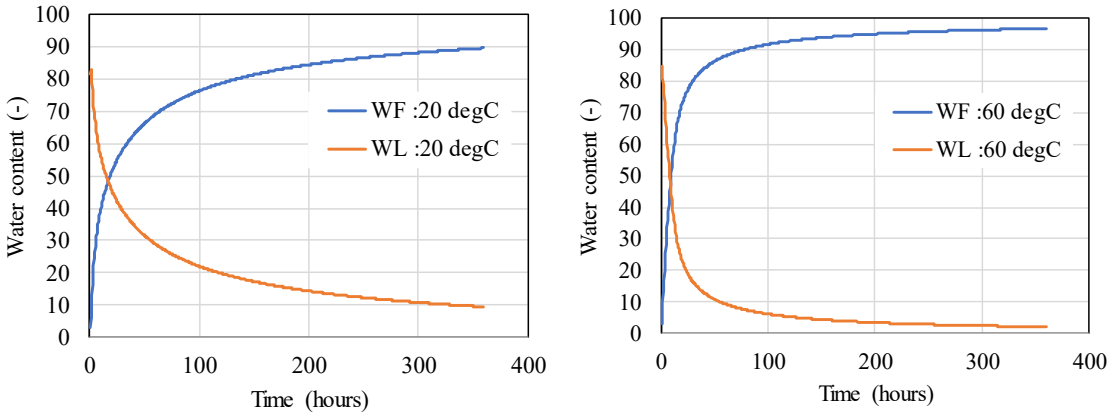

(a) 20 °C (b) 60 °C

Figure 4.16 Dynamic microstructural changes for a surface node at (a) 20 °C and (b) 60 °C.

To predict the penetration depth in the target concrete, the second slope was determined experimentally over a period greater than two days. According to other studies, experiments should last more than one week for concrete [12], [14]. At higher temperatures, the second slope appears much earlier in the experiment.

The offset value for the second slope (y-intercept) was less than 10 mm. Using this offset value and the water contact time, the depth of water penetration in the concrete could be

estimated. This value corresponds to the maximum depth of water penetration in the concrete.

Slope estimations for water penetration behaviors are challenging. Initially, the first slope was estimated using changes in the surface tension and the viscosity of the pore solution; however, after this calculation, it was found that the slope was affected by the balance between microstructural changes and the water transfer coefficients between fine pores and large pores. Under various temperature conditions, the C-S-H structures had different properties. Since the second slope showed trends that were contrary to those expected by pore solution surface tension and viscosity properties, it is challenging to explain the decreased slope without densification of the C-S-H structures. To accurately predict water transport, further quantitative data for microstructural changes coupled with sorptivity measurements are required.

4.4. Conclusions

As a step toward estimating the degree of concrete contamination following the Fukushima Daiichi accident, x-ray radiography was used to measure the sorptivity of mortar containing different cement and aggregate types under two different temperature conditions, i.e. 20 and 60 °C. The results were numerically evaluated using a simplified finite differential method, which considered microstructural changes after water uptake and the resultant changes in the water transfer coefficient. From the results, the following can be determined:

- The sorptivity measurements showed that water transport displayed anomalous behavior; the relationship between the penetration depth or total absorbed volume of water and the square root of exposure time deviated from a linear relationship and became nonlinear. The trend was bimodal, and the second slope appears after a certain hour of exposed time, which is necessary to show the rearrangement of C-S-H structure.
- Mortar containing fly ash (FAC mortar) had a lower sorptivity than that of mortar containing ordinary Portland cement (OPC mortar) under the same volumetric mixture proportions. One possible explanation is that the morphology of calcium silicate hydrate (C-S-H) is affected by the calcium-silicate ratio. The behavior of water in the OPC mortar was more anomalous than in FAC mortar.
- At higher temperatures, the first slope is larger, while the second slope is smaller. The second slope cannot be explained only by changes in the surface tension and viscosity of the pore solution; C-S-H structure rearrangement may be the dominant factor for the slope change at elevated temperature.

5. Summary and Future perspective

In recent years, many problems such as premature deterioration and shrinkage cracking of concrete structures have been raised, and it has become an issue to extend the service life of buildings and to predict the future, and it is required to evaluate the performance such as strength and durability along the time axis. In particular, cracking can be caused by a wide range of factors such as settlement during placing, self-shrinking of cement, neutralisation, corrosion of steel and alkali-silica reactions. Cracks in concrete allow rainwater and salt to penetrate the concrete and accelerate the deterioration of the building. Cracks in concrete lead to a reduction in strength and Young's modulus, which are governed by factors such as aggregate, cement hardener and voids. Among these, chemical changes in the cement hardener and physical changes in the voids are the most important factors. Therefore, it is important to measure the pore structure of concrete, mortar and cement paste in order to understand their physical properties and durability. In addition, concrete structures in real environments are subjected to all kinds of changes. It is necessary to understand the changes in the hardened cement under such realistic conditions, such as drying, which is a cause of cracking of concrete. Therefore, it is necessary to understand the behavior of water and the change of porosity in concrete under various conditions such as drying and high temperature.

5.1. Summary

Chapter 1:- This chapter describes the **section 1.1.1** about the background of this thesis, From a macroscopic point of view, the hydration of Portland cment at room temperature gives rise to a plastic and adherent product which sets both in air and under water in a few hours, but which hardens progressivelys over several weeks, months and even years until if axquires its fundamental properties: strength and durability. Similary, if the process is observed from a microscopic point of view, the hydration of the cement based materials leads to the formation of a set of minority crystalline products (ettringite and portlandite) and a majority amorphous product, which is responsible for the properties. This compound is a calcium silicate hydrate (C-S-H) of variable composition. In **section 1.1.2**, the background of the thesis is described as the importance of understanding the water uptake behavior in concrete for the estimating the amount of waste for decommissioning of Fukushima Daiichi nuclear power plants, and the demand for the establishment of a non destructive techniques for the specimens current status of water uptake tests on cement based materials. Based on the aboe background, the objective of this

study is to establish a measurement techniques by using ^{1}H-NMR relaxometry, X-ray computed radiography is a non-destructive techniques, and to analyze the behaviour of water uptake movement after drying at (105 °C) at different temperatures (20 °C, 40 °C and 60 °C) and at RH-40% at room temperature (20 °C) by using this techniques.

Chapter 2 :- Literature review presents about the structure of C-S-H. In **section 2.1** and **section 2.2**, the existence of a great variety of commercial cements that the C-S-H presents in cement pastes have a great variability in terms of composition, structure and microstructure. All this, together with the fact that the C-S-H has an amorphous nature, means that its structure is not well known. There has been a succession of experimental work was done at developing a structural model of the hydrated phases of cement. The models that attempts to explain the structure of C-S-H by :- (1) Crystalline models, (2) Meso-scale models. Based on scientific and technological development gradually made it possible to study this compound in greated depth through the application of new techniques such as electron microprobe (EMPA), scanning electron microscopy (SEM), Transmission electron microscopy (TEM), X-ray diffraction (XRD), Fourier transform infrared spectrsoscopy (FTIR), Water and Nitrogen sorption and Nuclear magnetic resonance (NMR). Gradually, different structural models were developed in an attempt to explain the structure of calcium silicate hydrate. In **section 2.3** and **section 2.5.1**, explains about the ^{1}H-NMR relaxometry has seen practical usability in cement and concrete research technology from many years and has successfully detected nuclear spin-lattice relaxometry. The longitudinal and the transverse relaxometry rely on the magnetic dipole to dipole interaction fluctuations resulting from the relative motion of pairs from the spins. Based on ^{1}H-NMR relaxometry signals , the relaxation times of T_1 and T_2 for the mobile components were measured based on the pulse sequence, inversion recovery, CPMG pulse sequence and FID. Based on the CPMG signal, the authors were analyzed to obtain T_2 distributions. The four confirmed T_2 peaks from the ILT algorithm were used to analyze the CPMG data. The four peaks and the ratio of each peak to the total intensity were used to evaluate the quantities of interlayer pore water, gel pore water, interhydrate pore water and capillary pore water. In **section 2.4** and **section 2.5.2**, washburns equation, which is a therotical equation for water absorption in a circular tube driven by capillary tension was introduced as a model applicable to cement based materiaals. In the present study, it was confirmed that the behavior was in accordance with the Washburn's equation.

In this paper, we introduced the methods of non-destructive liquid-water transfer measurement using several specimens of different lengths, mass change measurement of specimens with time, and imaging using neutron radiography. It is reported that the liquid penetration distance and the cumulative water uptake of the specimens are generally in

accordance with the Washburn's equation. By using neutron radiography imaging, it was reported that the liquid water distribution inside the specimen could be visualized nondestructively by obtaining the difference image between the specimen before the water absorption started and the transmitted image during each water absorption process.

Chapter 3:- In this thesis demonstrates how ^{1}H-NMR relaxometry is an established powerful technique for non-invasive and non-destructive characterization of pore size distribution and pore water interaction in cement based materials. How ^{1}H-NMR relaxometry may offer a lot of information on cement microstructure as a function of hydration time, temperature, drying (105 °C), and mixture composition. Furthermore, researchers gained a better understanding of pore-water interactions in cementitious materials.

^{1}H-NMR experiments have been proven to be quantitative. The measured CPMG were analyzed with ILT algorithm to obtain T_2 distribution. The water uptake test was performed at three different temperatures (20 ℃, 40 ℃ and 60 ℃). The water present in four peaks and the ratio of each peak to the intensity were used to evaluate the quantities of interlayer water, gel pore water, interhydrate pore water and capillary pore water was measured for the sealed condition, dried condition amd during the 26 days of water absorption process.

The evaporable water for different samples was measured with a balance in different conditions. The mass evolutions given by the balance and that obtained by ^{1}H-NMR signal being generally in the same range confirms that all the wateris captured by ^{1}H-NMR relaxometry. A high evaporable water content was observed for W55 compared to W40, which is consistent with the initial high water content and consequently the high porosity. For the sealed condition the water content was slightly higher as compared to the wetted samples for the different periods of sorption.

During the water absorption process, the interhydrate pores are quickly filled with water at the beginning of the sorption test before emptying into the finest porosities over time. The distribution of water from different pores to the gel pores increases with time and temperature. The water in the cement paste can be divided into two categories, the water in either fine pores or large pores. Where fine pores is the sum of (interlayer water+gel pore water) and where large pores is the sum of (interhydrate pore water + Capillary pore water). Based on the NMR signal, the NMR signals are expected to change with temperature, owing to the temperature dependence of the Boltzmann factor that contributes to the equilibrium nuclear magnetization. Based on the theory [152], [153], the 60 ℃/20 ℃ and 40 ℃/20 ℃ signal ratios were 0.880 and 0.936, respectively, while the obtained CPMG data was normalized by the data at the 20 ℃ condition. It is also assumed that the T_2 values at different temperatures are not affected by the temperature of the sample [153].The rate of

water redistribution between large pores and fine pores can be obtained and showing an increasing tendency with temperature. The activation energy for W40 and W55 are 36KJ/mol and 35KJ/mol corresponding to water exchange between large and fine pores was similar for both studied compositions. The activation energy obtained from the diffusion or permeability processes based on the previous studies was inferior to the measuered result. This difference can be linked to the microstructural rearrangement observed experimentally, which is not considered in classical water transport theories. A double slope was observed in the Arrhenius plots. The finest microstructure showed an important variation in the proportion of the gel and interlayer pores between the lowest temperatures (20 °C and 40 °C) and the higher temperature (60 °C), which can be linked to the variation in the necessary energy to move water between pores and to reorganize the microstructure.

The fast diffusion relaxation model links the T_2 relaxation time. The pore width is clearly proportional to the relaxation time T_2 and can provide initial details on the C-S-H microstructure. In the sealed condition, the size of the interlayer space is approximately 1.73±0.08 nm for W40 and approximately 2.07±0.11 nm for W55. Under 105 °C drying, most of the water is removed and the remaining fraction in the interlayer space shows a stacked C-S-H structure with an interlayer width equal to 1.24±0.20 nm and 1.20±0.20 nm for W40 and W55, respectively. After wetting, the interlayer spaces of W40 and W55 broaden again, returning after 26 days to their initial sizes of 1.72±0.11 nm and 2.02±0.11 nm, respectively, at 20 °C, and to a greater sizes of 1.87±0.05 nm and 2.34±0.33 nm, respectively, at 40 °C and to 2.00±0.19 nm and 2.30±0.00 nm, respectively, at 60 °C. The absorption under high temperatures clearly widens the interlayer pores. The same observations can be made for the gel pores with average initial widths of 4.42±0.72 nm and 5.16±0.30 nm for respectively W40 and W55 in the sealed condition. The gel pores become larger after wetting, especially for higher temperatures. After 26 days of water absorption for W40 and W55, the calculated widths are equal to 5.21±0.47 nm and 5.71±0.17 nm, respectively, at 20 °C; to 5.54±0.19 nm and 6.71±0.10 nm, respectively, at 40 °C; and to 5.49±0.39 nm (7.31±0.00 nm) at 60 °C. For interhydate and capillary pores, more fluctuation is observed with temperature, which can be explained by the signal to noise ratio and lower number of detected pores as compared to the finest pores.

Chapter 4:- X-ray computed radiography is a non-destructive method, and to anlayze the behavior of liquid water movement in mortar specimens. The washburn's equation which is a theoretical equation of water absorption behavior in a circular tube driven by capillary tension, is introduced as a water absorption process applicable to cement based materials. In the present study, it was confiems that the behavior was in

accordance with the washburn's equation. Based on the X-CR imaging, the liquid water distribution could be visualized by substracting the difference in the images between the transmitted image at each water absorption process and the transmitted image at drying as a background image. By comparing the changes in the luminance values of the transmitted image in the direction of water absorption with the luminance value of the transmitted image during drying, the distance of liquid water penetration was derived. It was confirmed that the distance of water penetration and the amount if cumulative water absorption were approximately linearly related to the square root of time and behaved in accordance with washburn's equation, which indicated that the data obtained by non-destructive measurement using X-CR observation was valid and significant experimental method.

X-CR was used to measure the sorpivity of mortar containing different cement and aggregate types under two different temperature conditions (20 °C and 60 °C). The results were numerically evaluated using a simplified finite differential method, which considered microstructural changes after water uptake and the resultant changes in the water transfer coefficient. The sorptivity measurements showed that water transport displayed anomalous behavior; the relationship between the penetration depth or total absorbed volume of water and the square root of exposure time deviated from a linear relationship and became nonlinear. The trend was bimodal, and the second slope appears after a certain hour of exposed time, which is necessary to show the rearrangement of C-S-H structure. Mortar containing fly ash (FAC mortar) had a lower sorptivity than that of mortar containing ordinary Portland cement (OPC mortar) under the same volumetric mixture proportions. One possible explanation is that the morphology of calcium silicate hydrate (C-S-H) is affected by the calcium-silicate ratio. The behavior of water in the OPC mortar was more anomalous than in FAC mortar. At higher temperatures, the first slope is larger, while the second slope is smaller. The second slope cannot be explained only by changes in the surface tension and viscosity of the pore solution; C-S-H structure rearrangement may be the dominant factor for the slope change at elevated temperatures.

5.2. Future Perspective

The proton NMR has seen practical usability in cement and concrete research technology for many years and has successfully detected nuclear spin-lattice relaxometry. The longitudinal (T_1) and the transverse (T_2) relaxometry rely on the magnetic dipole to dipole interaction fluctuations resulting from the relative motion of pairs from the spins. Based on ^{1}H-NMR relaxometry signals , the relaxation times of T_1 and T_2 for the mobile components were measured based on the pulse sequence, inversion recovery, CPMG

signal,FID and solid echo signal. Based on CPMG signal, the data were analyzed based on the inverse laplace transform to obtain the T_2 distributions. The four confirmed T_2 peaks from the ILT algorithm were used to analyze the CPMG data. The four peaks and the ratio of each peak to the total intensity were used to evaluate the quantities of interlayer pore water, gel pore water, interhydrate pore water and capillary pore water. Hardened cement paste samples that are either sealed or cured under (water or saturated lime water) from the very beginning age. ^{1}H-NMR relaxometry can be used to understand the behaviour of dynamic microstructural change of C-S-H. The water uptake test can be performed at different drying conditions under different temperatures. To understand the behaviour of pore water and the rate of water exchange between the fine pore water and large pore water of hardened cement based materials. Fine pore water is considered as the sum of (interlayer water + gel pore water) and large pore water is considered as the sum of (Interhydrate pore water +Capillary pore water). If the rate of water movement is a function fine pore water and large pore water. The activation energy corresponding to the water uptake after adsorption from large pore water to fine pore water under different drying conditions and at different tempertaures can be calculated and it can be explained by the dynamic microstructure.

X-ray computed radiograph is a non-destuctive method for the visualization of water penetration in the sample during water absorption process can be visualized. It can be said that it is possible to use for the estimation of actual concrete structures.

In the intrusion of liquid water, a change in pore structure of C-S-H in cement has a great effect. After the C-S-H structural change, it settles down to the $\sqrt{t}$ rule (the square root of time and the penetration depth are proportional). The velocity coefficient at this time is affected by the surface tension and visocisty of the liquid water. In order to understand the actual depth, prepare a large specimen or more at an arbitrary temperature with cement based materials and acquire a more data, from the estimated value of the temperature and the water contact time.

6. Appendix

A– Appendix: CPMG data based on ^{1}H-NMR relaxometry

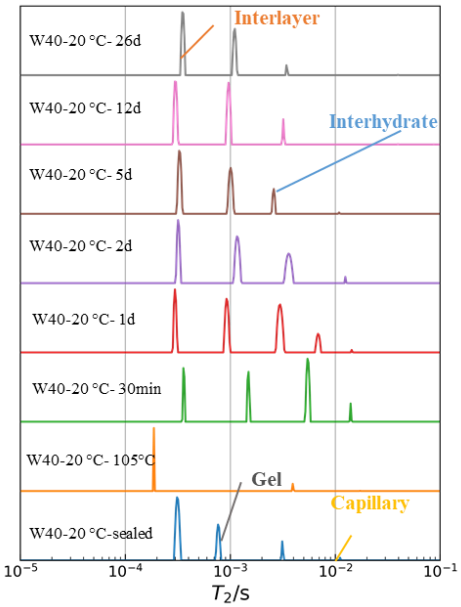

(a) W40 – 20 °C

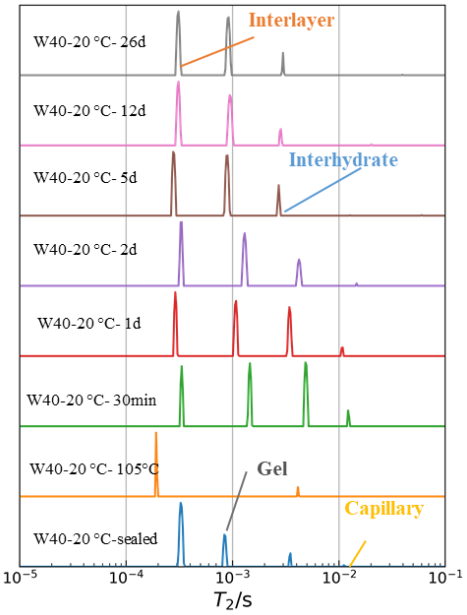

(b) W40 - 20 °C

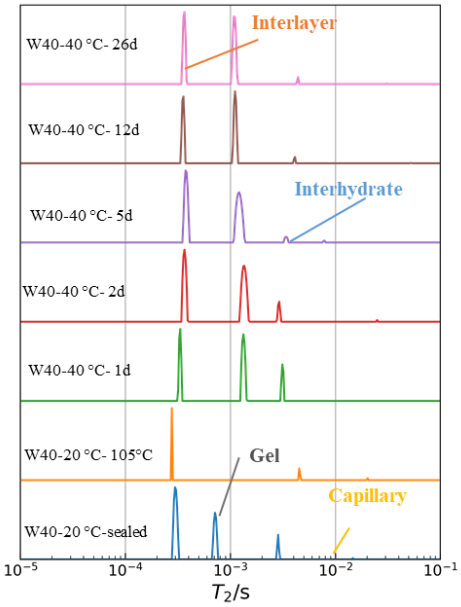

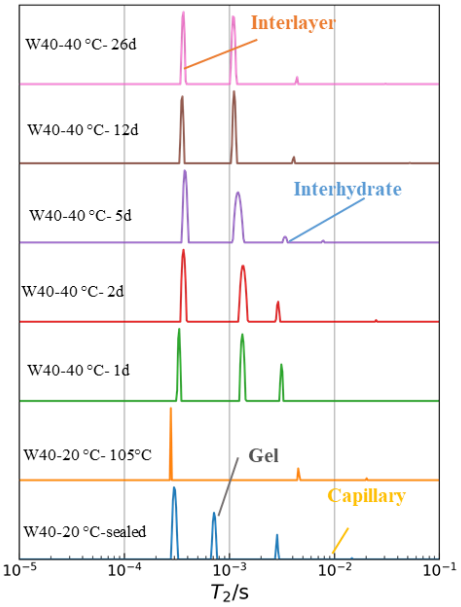

(c) W40 - 40 °C

(d) W40 - 40 °C

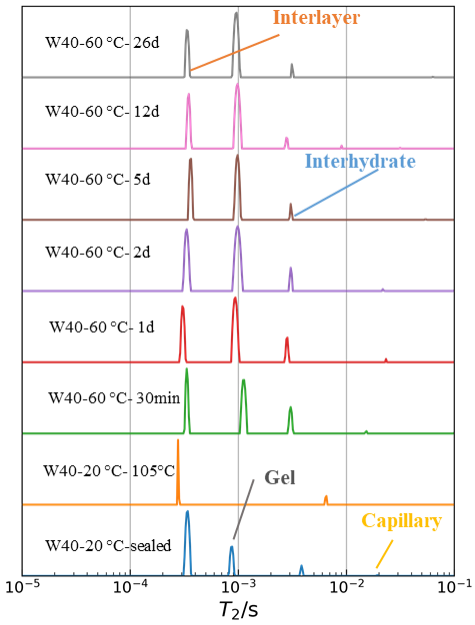

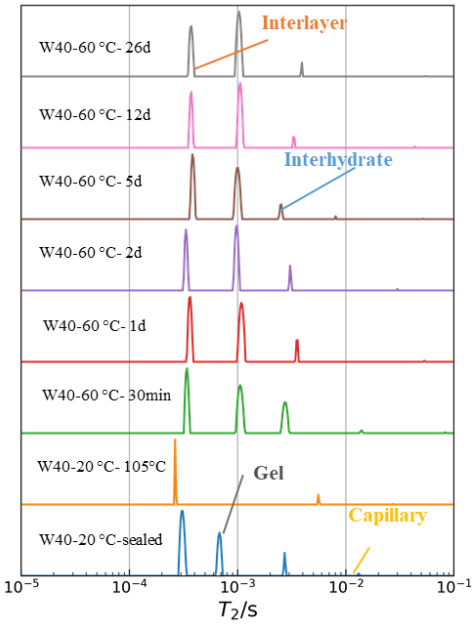

(e) W40 - 60 °C

(f) W40 - 60 °C

Figure A 1– T_2 distribution calculated by an inverse Laplace transformation of the CPMG signal of W40 under temperatures of 20 °C, 40 °C, and 60 °C

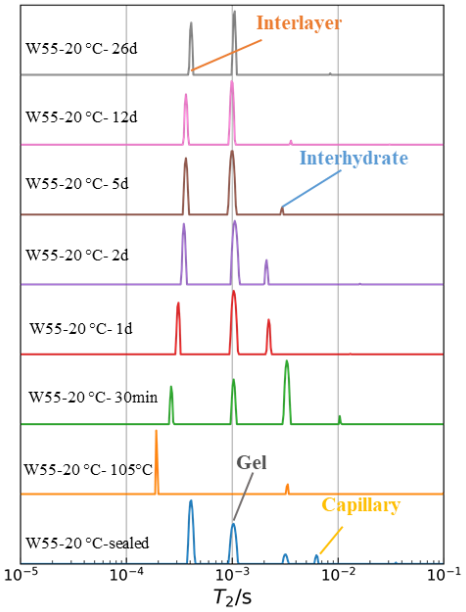

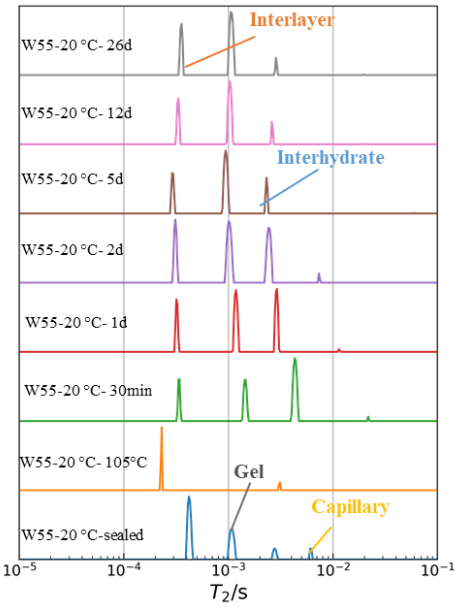

(a) W55 – 20 °C

(b) W55 – 20 °C

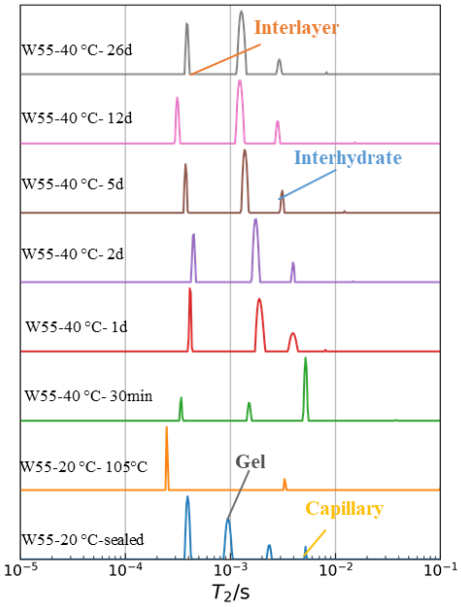

(c) W55 – 40 °C

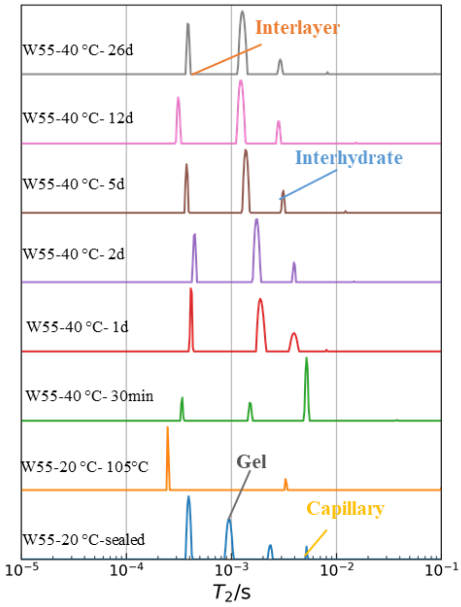

(d) W55 – 40 °C

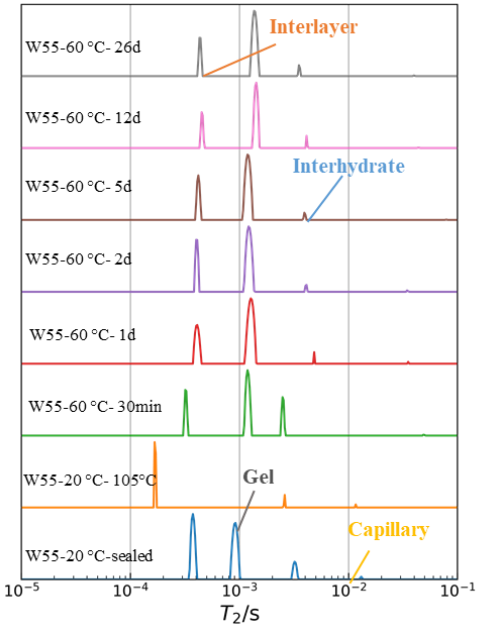

(e) W55 – 60 °C

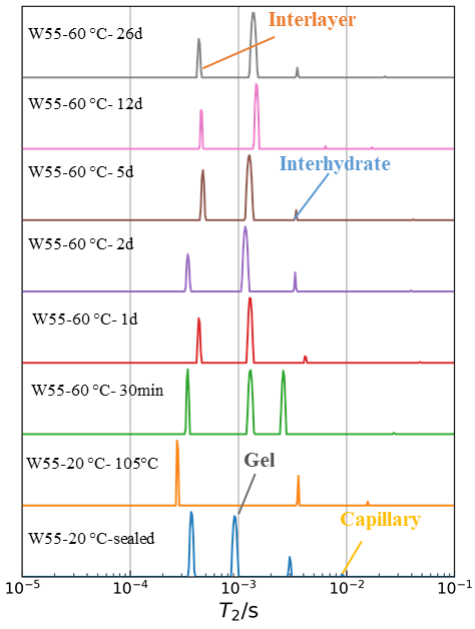

(f) W55 – 60 °C

Figure A 2– T_2 distribution calculated by an inverse Laplace transformation of the CPMG signal of W55 under temperatures of 20 °C, 40 °C, and 60 °C.

B – Appendix: X-ray computed radiography

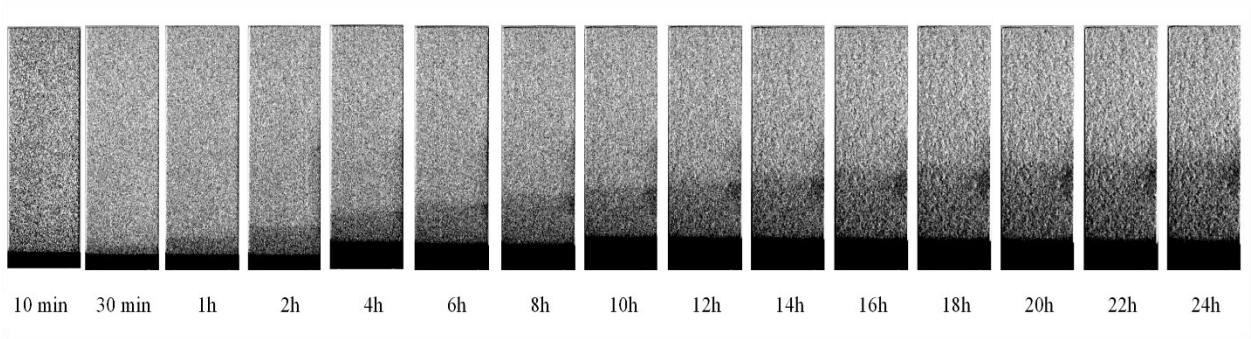

(a) Visualization of water penetration into OPC-LS-RH40%-20 °C mortar specimen

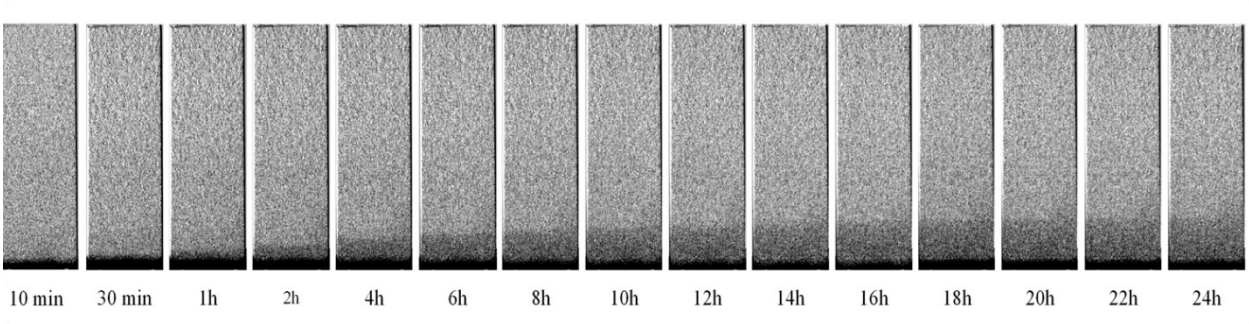

(b) Visualization of water penetration into FAC-LS-RH40%-20 °C mortar specimen

Figure B 1 – Visualization of water penetration in mortar specimen. The width of image is about 2 cm

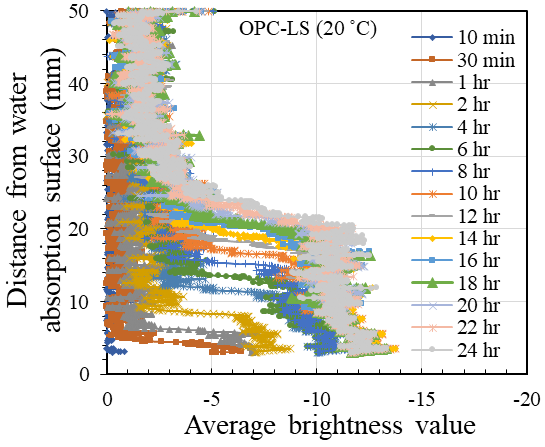

(a) OPC-LS-RH40%-20 °C

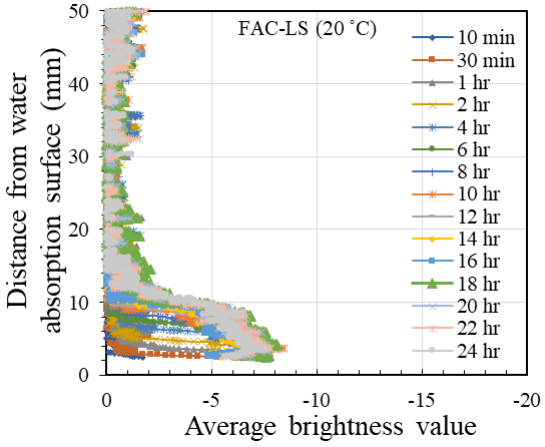

(b) FAC-LS-RH40%-20 °C

Figure B 2 – Results of the x-ray computed radiography (average brightness value) for the water absorption, in which water at 20 °C was absorbed from the bottom surface of the mortar specimens dried at RH-40%

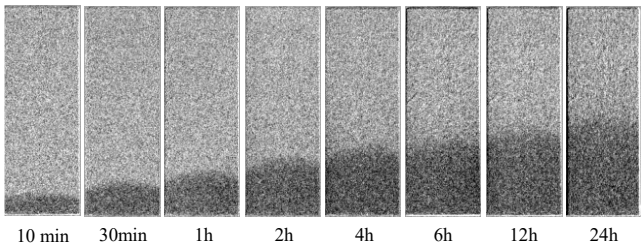

(a) Visualization of water penetration into OPC-LS -105°C-60 °C mortar specimen

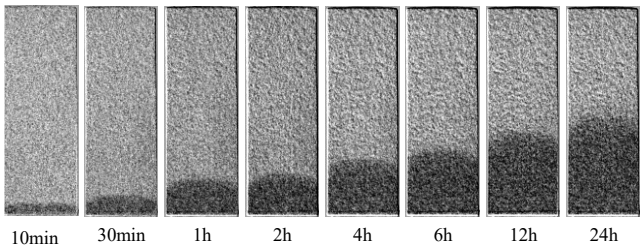

(b) Visualization of water penetration into FAC-LS -105°C-60 °C mortar specimen

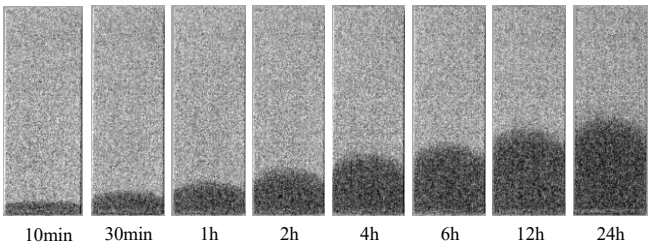

(c) Visualization of water penetration into FAC-RS -105°C-60 °C mortar specimen

Figure B 3 - Visualization of water penetration in mortar specimen.

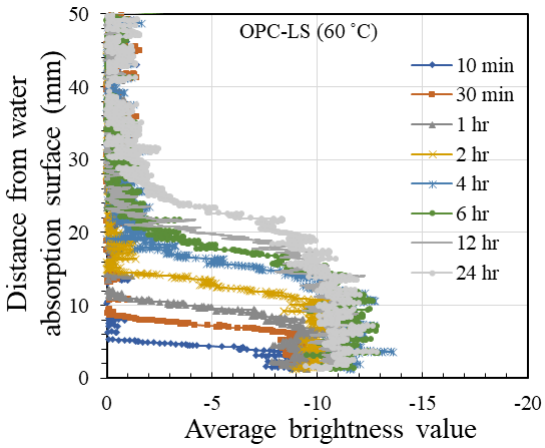

(a) OPC-LS -105°C-60 °C

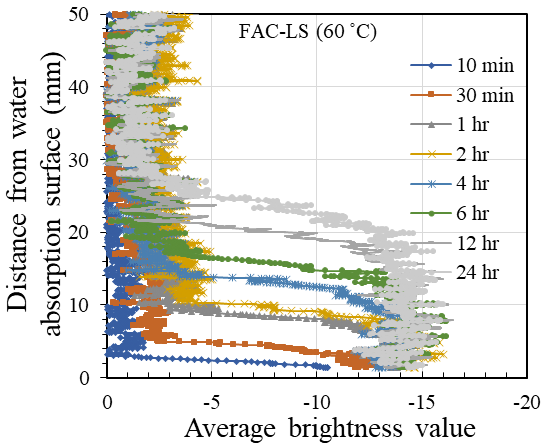

(b) FAC-LS -105°C-60 °C

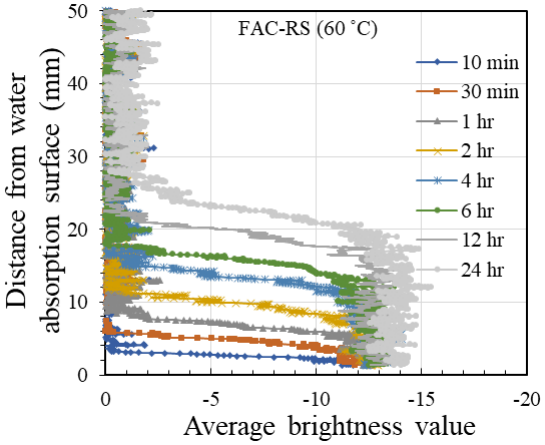

(c) FAC-RS -105°C-60 °C

Figure B 4 – Results of the x-ray computed radiography (average brightness value) for the water absorption, in which water at 60 °C was absorbed from the bottom surface of the mortar specimens dried at 105°C

7. References

[1] E. Gartner, “Industrially interesting approaches to ‘low-CO2’ cements,” *Cement and Concrete Research*, vol. 34, no. 9. pp. 1489–1498, 2004.

[2] H. F. W. Taylor, “Cement chemistry,” *Cem. Chem.*, 1997.

[3] P. Kumar Mehta and P. J. M. Monteiro, *Concrete: Microstructure, Properties, and Materials*. .

[4] J. P. Ollivier, J. C. Maso, and B. Bourdette, “Interfacial transition zone in concrete,” *Advanced Cement Based Materials*, vol. 2, no. 1. pp. 30–38, 1995.

[5] JamesBeaudoin and Ivan Odler, *5 - Hydration, Setting and Hardening of Portland Cement*. 2019.

[6] K. L. Scrivener, “Backscattered electron imaging of cementitious microstructures: Understanding and quantification,” *Cem. Concr. Compos.*, vol. 26, no. 8, pp. 935–945, 2004.

[7] J. Rymeš *et al.*, “Long-term material properties of a thick concrete wall exposed to ordinary environmental conditions in a nuclear reactor building: The contribution of cement hydrates and feldspar interaction,” *J. Adv. Concr. Technol.*, vol. 17, no. 5, pp. 195–215, 2019.

[8] I. Maruyama *et al.*, “Long-term use of modern Portland cement concrete: The impact of Al-tobermorite formation,” *Mater. Des.*, vol. 198, p. 109297, Jan. 2021.

[9] K. Yamada, M. Osako, and T. Yasutaka, “Study on the Strategy for Final Disposal and Reuse of Decontamination Wastes after the Fukushima Daiichi NPP Accident,” *Proc. WM Symp.*, vol. 20426, 2020.

[10] METI, “Mid-and-Long-Term Roadmap towards the Decommissioning of TEPCO’s Fukushima Daiichi Nuclear Power Station,” 2019.

[11] C. Hall *et al.*, “Water anomaly in capillary liquid absorption by cement-based materials,” *J. Mater. Sci. Lett.*, vol. 14, no. 17, pp. 1178–1181, 1995.

[12] S. C. Taylor, W. D. Hoff, M. A. Wilson, and K. M. Green, “Anomalous water transport properties of Portland and blended cement-based materials,” *J. Mater. Sci. Lett.*, vol. 18, no. 23, pp. 1925–1927, 1999.

[13] N. S. Martys and C. F. Ferraris, “Capillary transport in mortars and concrete,” *Cement and Concrete Research*, vol. 27, no. 5. pp. 747–760, 1997.

[14] C. Hall, “Anomalous diffusion in unsaturated flow: Fact or fiction?,” *Cem. Concr. Res.*, vol. 37, no. 3, pp. 378–385, 2007.

[15] I. Maruyama and J. Rymeš, “Temperature dependency of short-term length-change and desorption isotherms of matured hardened cement,” *J. Adv. Concr. Technol.*, vol. 17, no. 5, pp. 188–194, 2019.

[16] X. Li and Y. Xu, “Microstructure-Based Modeling for Water Permeability of Hydrating Cement Paste,” *J. Adv. Concr. Technol.*, vol. 17, no. 7, pp. 405–418, Jul. 2019.

[17] S. Bhattacharja, M. Moukwa, F. D'Orazio, J. Y. Jehng, and W. P. Halperin, "Microstructure determination of cement pastes by NMR and conventional techniques," *Adv. Cem. Based Mater.*, vol. 1, no. 2, pp. 67–76, Dec. 1993.

[18] W. P. Halperin, J. Y. Jehng, and Y. Q. Song, "Application of spin-spin relaxation to measurement of surface area and pore size distributions in a hydrating cement paste," *Magn. Reson. Imaging*, vol. 12, no. 2, pp. 169–173, Jan. 1994.

[19] N. S. Martys and C. F. Ferraris, "Capillary transport in mortars and concrete," *Cem. Concr. Res.*, vol. 27, no. 5, pp. 747–760, 1997.

[20] C. Hall, "Capillary imbibition in cement-based materials with time-dependent permeability," *Cem. Concr. Res.*, vol. 124, p. 105835, Oct. 2019.

[21] Z. Zhang and U. Angst, "A Dual-Permeability Approach to Study Anomalous Moisture Transport Properties of Cement-Based Materials," *Transp. Porous Media*, vol. 135, no. 1, pp. 59–78, 2020.

[22] N. M. Alderete, Y. A. Villagrán Zaccardi, and N. De Belie, "Physical evidence of swelling as the cause of anomalous capillary water uptake by cementitious materials," *Cem. Concr. Res.*, vol. 120, pp. 256–266, Jun. 2019.

[23] P. J. McDonald, O. Istok, M. Janota, A. M. Gajewicz-Jaromin, and D. A. Faux, "Sorption, anomalous water transport and dynamic porosity in cement paste: A spatially localised 1H NMR relaxation study and a proposed mechanism," *Cement and Concrete Research*, vol. 133. 2020.

[24] Z. Wu, H. S. Wong, C. Chen, and N. R. Buenfeld, "Anomalous water absorption in cement-based materials caused by drying shrinkage induced microcracks," *Cement and Concrete Research*, vol. 115. pp. 90–104, 2019.

[25] C. Biagioni, E. Bonaccorsi, M. Lezzerini, M. Merlini, and S. Merlino, "Thermal behaviour of tobermorite from N'Chwaning II mine (Kalahari Manganese Field, Republic of South Africa). I. Thermo-gravimetric and X-ray diffraction studies," *Eur. J. Mineral.*, vol. 24, no. 6, pp. 981–989, Nov. 2012.

[26] A. M. Gajewicz, E. Gartner, K. Kang, P. J. McDonald, and V. Yermakou, "A 1H NMR relaxometry investigation of gel-pore drying shrinkage in cement pastes," *Cem. Concr. Res.*, vol. 86, pp. 12–19, 2016.

[27] A. C. A. Muller, K. L. Scrivener, A. M. Gajewicz, and P. J. McDonald, "Densification of C-S-H measured by 1H NMR relaxometry," *J. Phys. Chem. C*, vol. 117, no. 1, pp. 403–412, 2013.

[28] C. Zhou, F. Ren, Z. Wang, W. Chen, and W. Wang, "Why permeability to water is anomalously lower than that to many other fluids for cement-based material?," *Cem. Concr. Res.*, vol. 100, pp. 373–384, 2017.

[29] I. Maruyama, T. Ohkubo, T. Haji, and R. Kurihara, "Dynamic microstructural evolution of

hardened cement paste during first drying monitored by 1H NMR relaxometry," *Cem. Concr. Res.*, vol. 122, no. August 2018, pp. 107–117, 2019.

[30] R. Kiran *et al.*, "Temperature-Dependent Water Redistribution from Large Pores to Fine Pores after Water Uptake in Hardened Cement Paste," *J. Adv. Concr. Technol.*, vol. 18, no. 10, pp. 588–599, 2020.

[31] L. Raki, J. Beaudoin, R. Alizadeh, J. Makar, and T. Sato, "Cement and concrete nanoscience and nanotechnology," *Materials*, vol. 3, no. 2. pp. 918–942, 2010.

[32] B. Lothenbach and A. Nonat, "Calcium silicate hydrates: Solid and liquid phase composition," *Cement and Concrete Research*, vol. 78. pp. 57–70, 2015.

[33] S. Garrault and A. Nonat, "Hydrated layer formation on tricalcium and dicalcium silicate surfaces: Experimental study and numerical simulations," *Langmuir*, vol. 17, no. 26, pp. 8131–8138, 2001.

[34] C. S. Walker, S. Sutou, C. Oda, M. Mihara, and A. Honda, "Calcium silicate hydrate (C-S-H) gel solubility data and a discrete solid phase model at 25 °C based on two binary non-ideal solid solutions," *Cem. Concr. Res.*, vol. 79, pp. 1–30, 2016.

[35] H. F. . Taylor and D. E. Newbury, "Calcium hydroxide distribution and calcium silicate hydrate composition in tricalcium silicate and β-dicalcium silicate pastes," *Cem. Concr. Res.*, vol. 14, no. 1, pp. 93–98, 1984.

[36] I. G. Richardson and G. W. Groves, "Microstructure and microanalysis of hardened ordinary Portland cement pastes," *Journal of Materials Science*, vol. 28, no. 1. pp. 265–277, 1993.

[37] I. G. Richardson, "The nature of the hydration products in hardened cement pastes," *Cem. Concr. Compos.*, vol. 22, no. 2, pp. 97–113, 2000.

[38] I. G. Richardson, "The nature of C-S-H in hardened cements," *Cem. Concr. Compos.*, vol. 29, no. 2, pp. 1131–1147, 1999.

[39] M. T. Blanco-Varela, S. Martínez-Ramírez, M. Gener, and T. Vázquez, "Modifications induced by adding natural zeolitic pozzolans to cement paste," *Mater. Constr.*, vol. 55, no. 280, pp. 27–42, 2005.

[40] H. F. W. Taylor, "Hydrated calcium silicates. Part I. Compound formation at ordinary temperatures," *J. Chem. Soc.*, pp. 3682–3690, 1950.

[41] D. L. Kantro, S. Brunauer, and C. H. Weise, "The ball-mill hydration of tricalcium silicate at room temperature," *Journal of Colloid Science*, vol. 14, no. 4. pp. 363–376, 1959.

[42] J. Haas and A. Nonat, "From C-S-H to C-A-S-H: Experimental study and thermodynamic modelling," *Cem. Concr. Res.*, vol. 68, pp. 124–138, 2015.

[43] L. S. Dent Glasser, E. E. Lachowski, K. Mohan, and H. F. W. Taylor, "A multi-method study of C3S hydration," *Cem. Concr. Res.*, vol. 8, no. 6, pp. 733–739, 1978.

[44] I. G. Richardson, A. R. Brough, G. W. Groves, and C. M. Dobson, "The characterization of

hardened alkali-activated blast-furnace slag pastes and the nature of the calcium silicate hydrate (C-S-H) phase," *Cem. Concr. Res.*, vol. 24, no. 5, pp. 813–829, 1994.

[45] C. K. Yip and J. S. J. Van Deventer, "Microanalysis of calcium silicate hydrate gel formed within a geopolymeric binder," *Journal of Materials Science*, vol. 38, no. 18. pp. 3851–3860, 2003.

[46] W. S. Chiang, E. Fratini, P. Baglioni, D. Liu, and S. H. Chen, "Microstructure determination of calcium-silicate-hydrate globules by small-angle neutron scattering," *J. Phys. Chem. C*, vol. 116, no. 8, pp. 5055–5061, 2012.

[47] F. Battocchio, P. J. M. Monteiro, and H. R. Wenk, "Rietveld refinement of the structures of 1.0 C-S-H and 1.5 C-S-H," *Cement and Concrete Research*, vol. 42, no. 11. pp. 1534–1548, 2012.

[48] E. T. Rodriguez, I. G. Richardson, L. Black, E. Boehm-Courjault, A. Nonat, and J. Skibsted, "Composition, silicate anion structure and morphology of calcium silicate hydrates (C-S-H) synthesised by silica-lime reaction and by controlled hydration of tricalcium silicate (C3S)," in *Advances in Applied Ceramics*, 2015, vol. 114, no. 7, pp. 362–371.

[49] E. Gartner, I. Maruyama, and J. Chen, "A new model for the C-S-H phase formed during the hydration of Portland cements," *Cement and Concrete Research*, vol. 97. pp. 95–106, 2017.

[50] E. Bonaccorsi, S. Merlino, and A. R. Kampf, "The crystal structure of tobermorite 14 Å (plombierite), a C-S-H phase," *J. Am. Ceram. Soc.*, vol. 88, no. 3, pp. 505–512, 2005.

[51] H. Bonaccorsi, E., Merlino, S. y Taylor, "The crystal structure of jennite, Ca9Si6O18(OH)6·8H2O," *Cem. Concr. Res*, vol. 34, pp. 1481–1488, 2004.

[52] I. G. Richardson, "Tobermorite/jennite- and tobermorite/calcium hydroxide-based models for the structure of C-S-H: Applicability to hardened pastes of tricalcium silicate, β-dicalcium silicate, Portland cement, and blends of Portland cement with blast-furnace slag, metakaol," *Cem. Concr. Res.*, vol. 34, no. 9, pp. 1733–1777, 2004.

[53] I. G. Richardson, A. R. Brough, R. Brydson, G. W. Groves, and C. M. Dobson, "Location of Aluminum in Substituted Calcium Silicate Hydrate (C-S-H) Gels as Determined by 29Si and 27Al NMR and EELS," *J. Am. Ceram. Soc.*, vol. 76, no. 9, pp. 2285–2288, 1993.

[54] G. K. Sun, J. F. Young, and R. J. Kirkpatrick, "The role of Al in C-S-H: NMR, XRD, and compositional results for precipitated samples," *Cem. Concr. Res.*, vol. 36, no. 1, pp. 18–29, 2006.

[55] X. Pardal, I. Pochard, and A. Nonat, "Experimental study of Si-Al substitution in calcium-silicate-hydrate (C-S-H) prepared under equilibrium conditions," *Cement and Concrete Research*, vol. 39, no. 8. pp. 637–643, 2009.

[56] E. L'Hôpital, B. Lothenbach, G. Le Saout, D. Kulik, and K. Scrivener, "Incorporation of aluminium in calcium-silicate-hydrates," *Cement and Concrete Research*, vol. 75. pp. 91–103, 2015.

[57] E. L'Hôpital, B. Lothenbach, D. A. Kulik, and K. Scrivener, "Influence of calcium to silica ratio

on aluminium uptake in calcium silicate hydrate," *Cement and Concrete Research*, vol. 85. pp. 111–121, 2016.

[58] J. D. Bernal, J. W. Jeffery, and H. F. W. Taylor, "Crystallographic research on the hydration of Portland cement. A first report on investigations in progress," *Mag. Concr. Res.*, vol. 4, no. 11, pp. 49–54, Oct. 1952.

[59] C. Megaw, H. y Kelsey, "Crystal structure of tobermorite. Nature," pp. 390–391, 1956.

[60] H. Kurczyk, H. y Schwiete, "Concerning the hydration products of C3S and β-C2S," in *En IV International Congress of the Chemistry of Cement*, 1962, pp. 135–166.

[61] D. L. Kantro, S. Brunauer, and C. H. Weise, "Development of surface in the hydration of calcium silicates. II. Extension of investigations to earlier and later stages of hydration," *Journal of Physical Chemistry*, vol. 66, no. 10. pp. 1804–1809, 1962.

[62] J. Bernal, "The structure of cement hydration compounds," *En III Int. Congr. Chem. Cem.*, pp. 216–236, 1954.

[63] D. Stade, H. y Müller, "Stade, H. y Müller, D. (1987). On the coordination of Al in ill-crystallized C-S-H phases formed by hydration of tricalcium silicate and by precipitation reactions at ambient temperature," *Cem. Concr. Res*, pp. 147–151, 1987.

[64] F. P. GLASSER, E. E. LACHOWSKI, and D. E. MACPHEE, "Compositional Model for Calcium Silicate Hydrate (C-S-H) Gels, Their Solubilities, and Free Energies of Formation," *J. Am. Ceram. Soc.*, vol. 70, no. 7, pp. 481–485, 1987.

[65] M. W. Grutzeck, "A new model for the formation of calcium silicate hydrate (C-S-H)," *Mater. Res. Innov.*, vol. 3, no. 3, pp. 160–170, 1999.

[66] S. Rakiewicz, E., Benesi, A., Grutzeck, M. y Kwan, "Determination of the state of water in hydrated cement phases using deuterium NMR spectroscopy." pp. 6415–6416, 1998.

[67] H. F. W. Taylor, "Relationships Between Calcium Silicates and Clay Minerals," *Clay Miner.*, vol. 3, no. 16, pp. 98–111, 1956.

[68] H. F. W. TAYLOR, "Proposed Structure for Calcium Silicate Hydrate Gel," *J. Am. Ceram. Soc.*, vol. 69, no. 6, pp. 464–467, 1986.

[69] K. Mohan and H. F. W. Taylor, "A trimethylsilylation study of tricalcium silicate pastes," *Cem. Concr. Res.*, vol. 12, no. 1, pp. 25–31, 1982.

[70] I. G. Richardson and G. W. Groves, "Models for the composition and structure of calcium silicate hydrate (CSH) gel in hardened tricalcium silicate pastes," *Cem. Concr. Res.*, vol. 22, no. 6, pp. 1001–1010, 1992.

[71] I. G. Richardson and G. W. Groves, "The incorporation of minor and trace elements into calcium silicate hydrate (CSH) gel in hardened cement pastes," *Cem. Concr. Res.*, vol. 23, no. 1, pp. 131–138, 1993.

[72] S. Komarneni *et al.*, "27Al and29Si magic angle spinning nuclear magnetic resonance

spectroscopy of Al-substituted tobermorites," *J. Mater. Sci.*, vol. 20, no. 11, pp. 4209–4214, 1985.

[73] X. Cong and R. J. Kirkpatrick, "29Si and 17O NMR investigation of the structure of some crystalline calcium silica hydrates," *Adv. Cem. Based Mater.*, vol. 3, no. 3–4, pp. 133–143, 1996.

[74] X. Cong and R. James Kirkpatrick, "29Si MAS NMR study of the structure of calcium silicate hydrate," *Adv. Cem. Based Mater.*, vol. 3, no. 3–4, pp. 144–156, 1996.

[75] X. Cong and R. J. Kirkpatrick, "17O MAS NMR investigation of the structure of calcium silicate hydrate gel," *J. Am. Ceram. Soc.*, vol. 79, no. 6, pp. 1585–1592, 1996.

[76] J. J. Chen, J. J. Thomas, H. F. W. Taylor, and H. M. Jennings, "Solubility and structure of calcium silicate hydrate," *Cem. Concr. Res.*, vol. 34, no. 9, pp. 1499–1519, 2004.

[77] S. Grangeon, F. Claret, Y. Linard, and C. Chiaberge, "X-ray diffraction: A powerful tool to probe and understand the structure of nanocrystalline calcium silicate hydrates," *Acta Crystallographica Section B: Structural Science, Crystal Engineering and Materials*, vol. 69, no. 5. pp. 465–473, 2013.

[78] S. Grangeon, F. Claret, C. Roosz, T. Sato, S. Gaboreau, and Y. Linard, "Structure of nanocrystalline calcium silicate hydrates: Insights from X-ray diffraction, synchrotron X-ray absorption and nuclear magnetic resonance," *J. Appl. Crystallogr.*, vol. 49, pp. 771–783, 2016.

[79] Powers and Brownyard, "Studies of the Physical Properties of Hardened Portland Cement Paste," *ACI J. Proc.*, vol. 43, no. 9, pp. 2–8, 1946.

[80] T. C. Powers, "Structure and Physical Properties of Hardened Portland Cement Paste," *J. Am. Ceram. Soc.*, vol. 41, no. 1, pp. 1–6, 1958.

[81] S. Brunauer, J. Skalny, and E. E. Bodor, "Adsorption on nonporous solids," *J. Colloid Interface Sci.*, vol. 30, no. 4, pp. 546–552, 1969.

[82] R. F. Feldman and P. J. Sereda, "A model for hydrated Portland cement paste as deduced from sorption-length change and mechanical properties," *Matériaux Constr.*, vol. 1, no. 6, pp. 509–520, 1968.

[83] R. F. Feldman and others, "Sorption and length-change scanning isotherms of methanol and water on hydrated Portland cement," *Proceedings of the 5th International Symposium on the Chemistry of Cement*, vol. 3. pp. 53–66, 2010.

[84] R. F. Feldman, "Helium flow and density measurement of the hydrated tricalcium silicate - water system," *Cem. Concr. Res.*, vol. 2, no. 1, pp. 123–136, 1972.

[85] R. F. Feldman, "Assessment of Experimental Evidence for Models of Hydrated Portland Cement," *Highway Research Record 370,*. pp. 8–24, 1972.

[86] R. F. Feldman, "Application of the helium inflow technique for measuring surface area and hydraulic radius of hydrated portland cement," *Cem. Concr. Res.*, vol. 10, no. 5, pp. 657–664, 1980.

[87] H. J. H. Brouwers, "The work of Powers and Brownyard revisited: Part 1," *Cem. Concr. Res.*, vol. 34, no. 9, pp. 1697–1716, 2004.

[88] M. DAIMON, S. A. ABO-EL-ENEIN, G. ROSARA, S. GOTO, and R. KONDO, "Pore Structure of Calcium Silicate Hydrate in Hydrated Tricalcium Silicate," *J. Am. Ceram. Soc.*, vol. 60, no. 3–4, pp. 110–114, 1977.

[89] F. H. Wittmann, "On the action of capillary pressure in fresh concrete," *Cem. Concr. Res.*, vol. 6, no. 1, pp. 49–56, 1976.

[90] A. J. Alleni, R. C. Oberthur, D. Pearson, P. Schofield, and C. R. Wilding, "Development of the fine porosity and gel structure of hydrating cement systems," *Philosophical Magazine B: Physics of Condensed Matter; Statistical Mechanics, Electronic, Optical and Magnetic Properties*, vol. 56, no. 3. pp. 263–288, 1987.

[91] H. M. Jennings, "A model for the microstructure of calcium silicate hydrate in cement paste," *Cem. Concr. Res.*, vol. 30, no. 6, pp. 101–116, 2000.

[92] P. D. Tennis and H. M. Jennings, "Model for two types of calcium silicate hydrate in the microstructure of Portland cement pastes," *Cem. Concr. Res.*, vol. 30, no. 6, pp. 855–863, 2000.

[93] H. M. Jennings, "Colloid model of C–S–H and implications to the problem of creep and shrinkage," *Materials and Structures*, vol. 37, no. 1. pp. 59–70, 2004.

[94] J. J. Thomas and H. M. Jennings, "A colloidal interpretation of chemical aging of the C-S-H gel and its effects on the properties of cement paste," *Cem. Concr. Res.*, vol. 36, no. 1, pp. 30–38, 2006.

[95] A. J. Allen and J. J. Thomas, "Analysis of C-S-H gel and cement paste by small-angle neutron scattering," *Cem. Concr. Res.*, vol. 37, no. 3, pp. 319–324, 2007.

[96] H. M. Jennings, J. J. Thomas, J. S. Gevrenov, G. Constantinides, and F. J. Ulm, "A multi-technique investigation of the nanoporosity of cement paste," *Cem. Concr. Res.*, vol. 37, no. 3, pp. 329–336, 2007.

[97] A. J. Allen, J. J. Thomas, and H. M. Jennings, "Composition and density of nanoscale calcium-silicate-hydrate in cement," *Nat. Mater.*, vol. 6, no. 4, pp. 311–316, 2007.

[98] H. M. Jennings, "Refinements to colloid model of C-S-H in cement: CM-II," *Cem. Concr. Res.*, vol. 38, no. 3, pp. 275–289, 2008.

[99] P. J. McDonald, V. Rodin, and A. Valori, "Characterisation of intra- and inter-C-S-H gel pore water in white cement based on an analysis of NMR signal amplitudes as a function of water content," *Cem. Concr. Res.*, vol. 40, no. 12, pp. 1656–1663, 2010.

[100] V. Gajewicz, A. M., Gartner, E. Kang, K., McDonald, P.J., Yermakou, "A 1H NMR relaxometry investigation of gel-pore drying shrinkage in cement pastes.," vol. 86, pp. 1–28, 1999.

[101] A. C. A. Muller, K. L. Scrivener, A. M. Gajewicz, and P. J. McDonald, "Use of bench-top NMR to measure the density, composition and desorption isotherm of C-S-H in cement paste,"

Microporous Mesoporous Mater., vol. 178, pp. 99–103, 2013.

[102] E. Kawachi, K., Murakami, M., & Hirahara, "Studies on the hydration and hardening of cement (experimental studies on nuclear magnetic resonance of water molecules in cement)," *Bull. Fac. Eng. Hiroshima Univ.*, vol. 4, pp. 95–101, 1995.

[103] R. Blinc, M. Buragar, G. Lahajnar, M. Rozmarin, and V. Rutar, "NMR Relaxation Study of Adsorbed Water in Cement and C3S Pastes," *J. Am. Ceram. Soc.*, vol. 61, no. 1–2, pp. 35–37, 1978.

[104] L. J. Schreiner, J. C. Mactavish, L. Miljkovic, and M. M. Pintar, "NMR Line Shape-Spin-Lattice Relaxation Correlation Study of Portland Cement Hydration," *J. Am. Ceram. Soc.*, vol. 68, no. 1, pp. 10–16, 1985.

[105] D. D. Lasic, J. M. Corbett, J. Jiant, J. C. Tavish, and M. M. Pintar, "NMR spin grouping in hydrating cement at 200 MHz," *Cem. Concr. Res.*, vol. 18, no. 4, pp. 649–653, 1988.

[106] L. Miljkovic, D. Lasic, J. C. MacTavish, M. M. Pintar, R. Blinc, and G. Lahajnar, "NMR studies of hydrating cement: A spin-spin relaxation study of the early hydration stage," *Cem. Concr. Res.*, vol. 18, no. 6, pp. 951–956, 1988.

[107] W. P. Halperin, J. Y. Jehng, and Y. Q. Song, "Application of spin-spin relaxation to measurement of surface area and pore size distributions in a hydrating cement paste," *Magn. Reson. Imaging*, vol. 12, no. 2, pp. 169–173, 1994.

[108] J. Greener, H. Peemoeller, C. Choi, and R. Holly, "Monitoring of hydration of white cement paste with proton NMR spin-spin relaxation," *J. Am. Ceram. Soc.*, vol. 83, no. 3, pp. 623–627, 2000.

[109] R. Holly, E. J. Reardon, C. M. Hansson, and H. Peemoeller, "Proton spin-spin relaxation study of the effect of temperature on white cement hydration," *J. Am. Ceram. Soc.*, vol. 90, no. 2, pp. 570–577, 2007.

[110] A. C. A. MULLER, "Characterization of porosity & C-S-H in cement pastes by 1H NMR," *Cem. Concr. Res.*, vol. 52, no. 3, p. 246, 2015.

[111] A. C. A. Muller, K. L. Scrivener, A. M. Gajewicz, and P. J. Mcdonald, "Densification of C − S − H Measured by 1 H NMR Relaxometry," *J. Phys. Chem.*, pp. 403–412, 2013.

[112] A. C. A. Muller, K. L. Scrivener, J. Skibsted, A. M. Gajewicz, and P. J. McDonald, "Influence of silica fume on the microstructure of cement pastes: New insights from 1H NMR relaxometry," *Cement and Concrete Research*, vol. 74. pp. 116–125, 2015.

[113] A. C. A. Muller, K. L. Scrivener, A. M. Gajewicz, and P. J. McDonald, "Use of bench-top NMR to measure the density, composition and desorption isotherm of C-S-H in cement paste," *Microporous Mesoporous Mater.*, vol. 178, pp. 99–103, 2013.

[114] I. Maruyama, T. Ohkubo, T. Haji, and R. Kurihara, "Reply to Zhou et al.'s 'A discussion of the paper "Dynamic microstructural evaluation of hardened cement paste during first drying monitored by 1H NMR relaxometry,"'" *Cement and Concrete Research*, vol. 137. 2020.

[115] N. Fischer, R. Haerdtl, and P. J. McDonald, “Observation of the redistribution of nanoscale water filled porosity in cement based materials during wetting,” *Cem. Concr. Res.*, vol. 68, pp. 148–155, 2015.

[116] R. Schulte Holthausen and M. Raupach, “Monitoring the internal swelling in cementitious mortars with single-sided 1H nuclear magnetic resonance,” *Cem. Concr. Res.*, vol. 111, no. March, pp. 138–146, 2018.

[117] L. Monteilhet, J. P. Korb, J. Mitchell, and P. J. McDonald, “Observation of exchange of micropore water in cement pastes by two-dimensional T2 - T2 nuclear magnetic resonance relaxometry,” *Phys. Rev. E - Stat. Nonlinear, Soft Matter Phys.*, vol. 74, no. 6, pp. 1–9, 2006.

[118] P. J. McDonald, J. P. Korb, J. Mitchell, and L. Monteilhet, “Surface relaxation and chemical exchange in hydrating cement pastes: A two-dimensional NMR relaxation study,” *Phys. Rev. E - Stat. Nonlinear, Soft Matter Phys.*, vol. 72, no. 1, pp. 1–9, 2005.

[119] C. Hall and C. Hall, “Water sorptivity of mortars and concretes: A review,” *Mag. Concr. Res.*, vol. 41, no. 147, pp. 51–61, 1989.

[120] L. J. Parrott, “Water absorption in cover concrete,” *Mater. Struct.*, vol. 25, no. 5, pp. 284–292, 1992.

[121] L. J. Parrott, “Moisture conditioning and transport properties of concrete test specimens,” *Mater. Struct.*, vol. 27, no. 8, pp. 460–468, 1994.

[122] C. Hall, “Water anomaly in capillary liquid absorption by cement-based materials,” vol. 14, pp. 1178–1181, 1995.

[123] P. a Claisse, H. I. Elsayad, and I. G. Shaaban, “ABSORPTION AND SORPTIVITY OF COVER CONCRETE By Peter A. Claisse; Banaa I. Eisayad,z and Ibrahim G. Shaaban 3,” *J. Mater. Civ. Eng.*, vol. 9, no. 3, pp. 105–110, 1997.

[124] D. Andrade, C., Bettencourt-Ribeiro, A., Buenfeld, N. R., Carcasses, M., Carino, N. J., Ehrenberg, F., Ewertson, C., Garbocczi, E., Geiker, M., Gjorv, O. E., Goncalves, A. F., Gräf, H., Grube, H., Hilsdorf, H. K., Hooton, R. D., Kropp, J., Modry, S., Molin, “Concrete durability - an approach towards performance testing,” *Mater. Struct. Constr.*, vol. 32, no. 217, pp. 163–173, 1999.

[125] and R. W. Z. H.S. Wong*, M. Zobel*, N.R. Buenfeld*, “Influence of the interfacial transition zone and microcracking on the diffusivity, permeability and sorptivity of cement-based materials after drying,” *Mag. Concr. Res.*, vol. 61, no. 8, pp. 571–589, 2015.

[126] Z. Wu, H. S. Wong, C. Chen, and N. R. Buenfeld, “Anomalous water absorption in cement-based materials caused by drying shrinkage induced microcracks,” *Cem. Concr. Res.*, vol. 115, pp. 90–104, 2019.

[127] Y. A. Villagrán Zaccardi, N. M. Alderete, and N. De Belie, “Improved model for capillary absorption in cementitious materials: Progress over the fourth root of time,” *Cement and Concrete Research*, vol. 100. pp. 153–165, 2017.

[128] R. Kimmich, "NMR: Tomography, Diffusometry, Relaxometry," *Springer Berlin Heidelb.*, 1997.

[129] A. C. A. Muller, "Characterization of porosity & C-S-H in cement pastes by 1H NMR," vol. 6339, p. 208, 2014.

[130] A. Valori, P. J. McDonald, and K. L. Scrivener, "The morphology of C-S-H: Lessons from 1H nuclear magnetic resonance relaxometry," *Cement and Concrete Research*, vol. 49. pp. 65–81, 2013.

[131] A. Gajewicz, "Characterisation of cement microstructure and pore – water interaction by 1H Nuclear Magnetic Resonance Relaxometry," *Dep. Phys. Sci.*, 2014.

[132] F. Bloch, "Nuclear induction," *Phys. Rev.*, vol. 70, no. 7–8, pp. 460–474, 1946.

[133] P. J. McDonald, A. M. Gajewicz, and R. Morrell, "The characterisation of cement based materials using T2 1H nuclear magnetic resonance relaxation analysis.," *Meas. Good Pract. Guid.*, vol. 144, no. 144, 2017.

[134] H. Y. Carr and E. M. Purcell, "Effects of diffusion on free precession in nuclear magnetic resonance experiments," *Phys. Rev.*, vol. 94, no. 3, pp. 630–638, 1954.

[135] S. Meiboom and D. Gill, "Modified spin-echo method for measuring nuclear relaxation times," *Review of Scientific Instruments*, vol. 29, no. 8. pp. 688–691, 1958.

[136] I. Maruyama *et al.*, "Long-term use of modern Portland cement concrete: The impact of Al-tobermorite formation," *Mater. Des.*, vol. 198, 2021.

[137] J. G. Powles and J. H. Strange, "Zero time resolution nuclear magnetic resonance transient in solids," *Proc. Phys. Soc.*, vol. 82, no. 1, pp. 6–15, 1963.

[138] D. A. Faux, P. J. McDonald, N. C. Howlett, J. S. Bhatt, and S. V. Churakov, "Nuclear magnetic resonance relaxometry of water in two and quasi-two dimensions," *Phys. Rev. E - Stat. Nonlinear, Soft Matter Phys.*, vol. 87, no. 6, pp. 1–18, 2013.

[139] E. Washburn, "The dynamics of capillary flow," *Phys. Rev.*, vol. 17, no. 18, pp. 273–283, 1921.

[140] G. N. Hounsfield, "Computerized transverse axial scanning (tomography): I. Description of system," *Br. J. Radiol.*, vol. 46, no. 552, pp. 1016–1022, 1973.

[141] A. F. Nielsen, "Gamma-ray-attenuation used for measuring the moisture content and homogeneity of porous concrete," *Build. Sci.*, vol. 7, no. 4, pp. 257–263, 1972.

[142] R. A. Brooks and G. Di Chiro, "Beam hardening in X-ray reconstructive tomography," *Phys. Med. Biol.*, vol. 21, no. 3, pp. 390–398, 1976.

[143] K. Kupwade-Patil *et al.*, "Retarder effect on hydrating oil well cements investigated using in situ neutron/X-ray pair distribution function analysis," *Cement and Concrete Research*, vol. 126. 2019.

[144] O. Stamati, E. Roubin, E. Andò, and Y. Malecot, "Phase segmentation of concrete x-ray tomographic images at meso-scale: Validation with neutron tomography," *Cement and Concrete Composites*, vol. 88. pp. 8–16, 2018.

[145] A. du Plessis and W. P. Boshoff, “A review of X-ray computed tomography of concrete and asphalt construction materials,” *Constr. Build. Mater.*, vol. 199, pp. 637–651, 2019.

[146] F. C. De Beer, “Neutron- and X-ray radiography/tomography: Non-destructive analytical tools for the characterization of nuclear materials,” *J. South. African Inst. Min. Metall.*, vol. 115, no. 10, pp. 913–924, 2015.

[147] S. Roels and J. Carmeliet, “Analysis of moisture flow in porous materials using microfocus X-ray radiography,” *Int. J. Heat Mass Transf.*, vol. 49, no. 25–26, pp. 4762–4772, 2006.

[148] M. Lukovic, G. Ye, E. Schlangen, and K. Van Breugel, “Moisture movement in cement-based repair systems monitored by X-ray absorption,” *Heron*, vol. 62, no. 1, pp. 21–46, 2017.

[149] S. Meiboom and D. Gill, “Modified spin-echo method for measuring nuclear relaxation times,” *Rev. Sci. Instrum.*, vol. 29, no. 8, pp. 688–691, 1958.

[150] J. P. Butler, J. A. Reeds, and S. V Dawson, “Estimating Solutions of First Kind Integral Equations with Nonnegative Constraints and Optimal Smoothing,” *SIAM J. Numer. Anal.*, vol. 18, no. 3, pp. 381–397, 1981.

[151] A. C. A. Muller, K. L. Scrivener, A. M. Gajewicz, and P. J. Mcdonald, “Densification of C–S–H measured by 1H NMR relaxometry,” *J. Phys. Chem. C*, no. 117, pp. 403–412, 2013.

[152] K. V. R. Chary and G. Govil, *NMR in Biological Systems From Molecules to Humans*, vol. 6. Springer Science & Business Media, 2008.

[153] M. Wyrzykowski, P. J. McDonald, K. L. Scrivener, and P. Lura, “Water Redistribution within the Microstructure of Cementitious Materials due to Temperature Changes Studied with 1H NMR,” *J. Phys. Chem. C*, vol. 121, no. 50, pp. 27950–27962, 2017.

[154] Z. P. Bazant, G. Cusatis, and L. Cedolin, “Modeling Masonry Shear-Compression: Role of Dilatancy Highlighted,” *J. Eng. Mech.*, vol. 130, no. October, pp. 1195–1210, 2004.

[155] T. C. Powers, “The specific surface area of hydrated cement obtained from permeability data,” *Matériaux Constr.*, vol. 12, no. 3, pp. 159–168, 1979.

[156] B. P. Hughes, I. R. G. Lowe, and J. Walker, “The diffusion of water in concrete at temperatures between 50 and 95°C,” *Br. J. Appl. Phys.*, vol. 17, no. December, pp. 1545–1552, 1966.

[157] N. L. Hancox, “The role of moisture diffusion in the drying of cement paste under the influence of temperature gradients,” *J. Phys. D. Appl. Phys.*, vol. 1, no. 12, pp. 1769–1777, 1968.

[158] S. Nakashima, “Diffusivity of ions in pore water as a quantitative basis for rock deformation rate estimates,” *Tectonophysics*, vol. 245, pp. 185–203, 1995.

[159] N. Otsuki, M. S. Madlangbayan, T. Nishida, T. Saito, and M. A. Baccay, “Temperature dependency of chloride induced corrosion in concrete,” *J. Adv. Concr. Technol.*, vol. 7, no. 1, pp. 41–50, 2009.

[160] B. Zehtab and A. Tarighat, “Molecular dynamics simulation to assess the effect of temperature on diffusion coefficients of different ions and water molecules in C-S-H,” *Mech. Time-*

Dependent Mater., vol. 22, no. 4, pp. 483–497, 2018.

[161] P. Klug and F. Wittmann, "Activation energy of creep of hardened cement paste," *Matériaux Constr.*, vol. 2, no. 1, pp. 11–16, 1969.

[162] R. L. Day and B. R. Gamble, "The effect of changes in structure on the activation energy for the creep of concrete," *Cem. Concr. Res.*, vol. 13, no. 4, pp. 529–540, 1983.

[163] Z. P. Bazant, *Mathematical Modeling of Creep and Shrinkage of Concrete*. 1988.

[164] A. Pertué, P. Mounanga, and A. Khelidj, "Application of the maturity concept for the prediction of restrained autogenous shrinkage of cement pastes," in *Proceeding of the 3rd International Symposium GeoProc*, 2013, pp. 231–238.

[165] A. C. A. Muller, K. L. Scrivener, A. M. Gajewicz, and P. J. Mcdonald, "Densification of C − S − H Measured by 1 H NMR Relaxometry," 2013.

[166] M. Jooss and H. W. Reinhardt, "Permeability and diffusivity of concrete as function of temperature," *Cem. Concr. Res.*, vol. 32, no. 9, pp. 1497–1504, 2002.

[167] M. Choinska, A. Khelidj, G. Chatzigeorgiou, and G. Pijaudier-Cabot, "Effects and interactions of temperature and stress-level related damage on permeability of concrete," *Cem. Concr. Res.*, vol. 37, no. 1, pp. 79–88, 2007.

[168] I. Maruyama, J. Rymeš, M. Vandamme, and B. Coasne, "Cavitation of water in hardened cement paste under short-term desorption measurements," *Mater. Struct. Constr.*, vol. 51, no. 6, 2018.

[169] G. M. Glover and E. Raask, "Water diffusion and microstructure of hydrated cement pastes," *Matériaux Constr.*, vol. 5, no. 5, pp. 315–322, 1972.

[170] E. Drouet, S. Poyet, and J. M. Torrenti, "Temperature influence on water transport in hardened cement pastes," *Cem. Concr. Res.*, vol. 76, pp. 37–50, 2015.

[171] H. Kaburagi, "Fukushima genshiryoku kensetsu no gaiyou ni tsuite (brief summary of construction of fukushima nuclear power plant buildings)," *Hydro Electr. power*, vol. 98, pp. 75–88, in Japanese, 1969.

[172] L. Greenspan and others, "Humidity fixed points of binary saturated aqueous solutions," *J. Res. Natl. Bur. Stand. (1934).*, vol. 81, no. 1, pp. 89–96, 1977.

[173] L. a Feldkamp, "Practical cone-beam algorithm. Journal of the Optical Society of America A," *America (NY).*, vol. 1, no. 6, pp. 612–619, 1984.

[174] C. A. Schneider, W. S. Rasband, and K. W. Eliceiri, "NIH Image to ImageJ: 25 years of image analysis," *Nature Methods*, vol. 9, no. 7. pp. 671–675, 2012.

[175] M. K. Gopalan, "Sorptivity of fly ash concretes," *Cem. Concr. Res.*, vol. 26, no. 8, pp. 1189–1197, Aug. 1996.

[176] T. Jena and K. C. Panda, "Strength and Sorptivity of Concrete Using Fly Ash and Silpozz in Marine Environment," in *Lecture Notes in Civil Engineering*, vol. 75, Springer, 2021, pp. 625–639.

[177] H. Y. Leung, J. Kim, A. Nadeem, J. Jaganathan, and M. P. Anwar, "Sorptivity of self-compacting concrete containing fly ash and silica fume," *Constr. Build. Mater.*, vol. 113, pp. 369–375, Jun. 2016.

[178] D. Hatungimana, C. Taşköprü, M. İçhedef, M. M. Saç, and Ş. Yazıcı, "Compressive strength, water absorption, water sorptivity and surface radon exhalation rate of silica fume and fly ash based mortar," *J. Build. Eng.*, vol. 23, pp. 369–376, May 2019.

[179] C. Tasdemir, "Combined effects of mineral admixtures and curing conditions on the sorptivity coefficient of concrete," *Cem. Concr. Res.*, vol. 33, no. 10, pp. 1637–1642, Oct. 2003.

[180] I. G. Richardson, "Nature of C-S-H in hardened cements," *Cem. Concr. Res.*, vol. 29, no. 8, pp. 1131–1147, 1999.

[181] I. G. G. Richardson, J. Skibsted, L. Black, and R. J. J. Kirkpatrick, "Characterisation of cement hydrate phases by TEM, NMR and Raman spectroscopy," *Adv. Cem. Res.*, vol. 22, no. 4, pp. 233–248, Oct. 2010.

[182] I. G. Richardson, "Tobermorite/jennite- and tobermorite/calcium hydroxide-based models for the structure of C-S-H: applicability to hardened pastes of tricalcium silicate, -dicalcium silicate, Portland cement and blends of Portland cement with blast-furnace slag, metakaolin." pp. 1733–1777, 2004.

[183] Xie Ping, J. J. Beaudoin, and R. Brousseau, "Effect of aggregate size on transition zone properties at the portland cement paste interface," *Cem. Concr. Res.*, vol. 21, no. 6, pp. 999–1005, 1991.

[184] H. S. Wong, M. Zobel, N. R. Buenfeld, and R. W. Zimmerman, "Influence of the interfacial transition zone and microcracking on the diffusivity, permeability and sorptivity of cement-based materials after drying," *Mag. Concr. Res.*, vol. 61, no. 8, pp. 571–589, 2009.

[185] Z. Wu, H. S. Wong, C. Chen, and N. R. Buenfeld, "Anomalous water absorption in cement-based materials caused by drying shrinkage induced microcracks," *Cem. Concr. Res.*, vol. 115, no. August 2018, pp. 90–104, 2019.

[186] Z. Wu, H. S. Wong, and N. R. Buenfeld, "Influence of drying-induced microcracking and related size effects on mass transport properties of concrete," *Cem. Concr. Res.*, vol. 68, pp. 35–48, 2015.

[187] M. Saeidpour and L. Wadsö, "The influence of sorption hysteresis on diffusion coefficients represented with different moisture potentials," *Cem. Concr. Res.*, vol. 90, pp. 1–5, 2016.

[188] M. Saeidpour and L. Wadsö, "Evidence for anomalous water vapor sorption kinetics in cement based materials," *Cem. Concr. Res.*, vol. 70, pp. 60–66, 2015.

[189] M. Saeidpour and L. Wadsö, "Moisture diffusion coefficients of mortars in absorption and desorption," *Cem. Concr. Res.*, vol. 83, pp. 179–187, 2016.

[190] I. Maruyama, H. Sasano, Y. Nishioka, and G. Igarashi, "Strength and Young's modulus change

in concrete due to long-term drying and heating up to 90 °c," *Cem. Concr. Res.*, vol. 66, pp. 48–63, 2014.

[191] Z. Wu, H. S. Wong, and N. R. Buenfeld, "Transport properties of concrete after drying-wetting regimes to elucidate the effects of moisture content, hysteresis and microcracking," *Cem. Concr. Res.*, vol. 98, no. March, pp. 136–154, 2017.

[192] P. J. McDonald, O. Istok, M. Janota, A. M. Gajewicz-Jaromin, and D. A. Faux, "Sorption, anomalous water transport and dynamic porosity in cement paste: A spatially localised 1H NMR relaxation study and a proposed mechanism," *Cem. Concr. Res.*, vol. 133, no. March, p. 106045, 2020.

[193] K. Sakata, "A study on moisture diffusion in drying and drying shrinkage of concrete," *Cement and Concrete Research*, vol. 13, no. 2. pp. 216–224, 1983.

[194] A. M. Gajewicz-Jaromin, P. J. McDonald, A. C. A. Muller, and K. L. Scrivener, "Influence of curing temperature on cement paste microstructure measured by 1H NMR relaxometry," *Cem. Concr. Res.*, vol. 122, no. April, pp. 147–156, 2019.

[195] E. Gallucci, X. Zhang, and K. L. Scrivener, "Effect of temperature on the microstructure of calcium silicate hydrate (C-S-H)," *Cem. Concr. Res.*, vol. 53, pp. 185–195, 2013.

[196] S. Bahafid, S. Ghabezloo, M. Duc, P. Faure, and J. Sulem, "Effect of the hydration temperature on the microstructure of Class G cement: C-S-H composition and density," *Cem. Concr. Res.*, vol. 95, pp. 270–281, 2017.